

Exchange coupled $\text{Mn}_2\text{Au}/\text{Ni}_{81}\text{Fe}_{19}$ heterostructures for antiferromagnetic spintronics

An experimental study

Satya Prakash Bommanaboyena

born on 12.08.1990
in Hyderabad, India

Dissertation for attaining the academic degree of
“Doktor rerum naturalium” (Dr. rer. nat.)
of the departments
08 - Physics, Mathematics and Computer Science,
09 – Chemistry, Pharmaceutics and Geoscience,
10 – Biology and
University Medicine
of the Johannes Gutenberg Universität Mainz

Max Planck Graduate Center 
mit der Johannes Gutenberg-Universität



Max Planck Graduate Center
Johannes Gutenberg Universität Mainz

16th May 2022

Supervisors

xxx

xxx

Mentor & daily advisor

xxx

Mentor

xxx

Date of the oral examination: 14.09.2022

(The names have been removed in the electronic version of this thesis due to data protection regulations.)

Declaration

I hereby declare that I wrote the dissertation submitted without any unauthorized external assistance and used only sources acknowledged in the work. All textual passages which are appropriated verbatim or paraphrased from published and unpublished texts as well as all information obtained from oral sources are duly indicated and listed in accordance with bibliographical rules. In carrying out this research, I complied with the rules of standard scientific practice as formulated in the statutes of Johannes Gutenberg Universität Mainz to insure standard scientific practice.

Mainz,

[Date of submission]

[Signature]

Satya Prakash Bommanaboyena
Matrikelnummer: 2744369
Institut für Physik, Johannes Gutenberg Universität
Staudingerweg 7
55128 Mainz, Germany
sprakash@uni-mainz.de
satyaprakash.01123@gmail.com

Acknowledgements

Removed in the electronic version of this thesis due to data protection regulations.

Publications included in this thesis

- ❑ *High quality epitaxial Mn₂Au (001) thin films grown by molecular beam epitaxy.*
S. P. Bommanaboyena, T. Bergfeldt, R. Heller, M. Kläui and M. Jourdan.
Journal of Applied Physics **127**, 243901 (2020).

- ❑ *Readout of an antiferromagnetic spintronics system by strong exchange coupling of Mn₂Au and Permalloy.*
S. P. Bommanaboyena, D. Backes, L. S. I. Veiga, S. S. Dhesi, Y. R. Niu, B. Sarpi, T. Denneulin, A. Kovács, T. Mashoff, O. Gomonay, J. Sinova, K. Everschor-Sitte, D. Schönke, R. M. Reeve, M. Kläui, H.-J. Elmers and M. Jourdan.
Nature Communications **12**, 6539 (2021).

Conferences

- ❑ *Strongly exchange coupled Mn₂Au/Ni₈₁Fe₁₉ bilayers for antiferromagnetic spintronics.*
S. P. Bommanaboyena, D. Backes, L. Ishibe Veiga, S. S. Dhesi, Y. R. Niu, B. Sarpi, T. Denneulin, A. Kovacs, T. Mashoff, D. Schönke, R. M. Reeve, M. Kläui, H.-J. Elmers & M. Jourdan.
Poster presentation - Joint School on Spin Physics 2021, Apolda.

- ❑ *Large exchange coupling of Mn₂Au/Ni₈₁Fe₁₉ for antiferromagnetic spintronics.*

S. P. Bommanaboyena, D. Backes, L. Ishibe Veiga, S. S. Dhesi, Y. R. Niu, B. Sarpi, T. Denneulin, A. Kovacs, T. Mashoff, D. Schönke, R. M. Reeve, M. Kläui, H.-J. Elmers & M. Jourdan.

Poster presentation - Annual Meeting of DPG and DPG-Tagung of the Condensed Matter Section 2021.

- *High quality Mn₂Au (001) thin films for antiferromagnetic spintronics.*

S. P. Bommanaboyena, T. Denneulin, A. Kovacs, R. Heller, M. Kläui & M. Jourdan.

Poster presentation - Annual Meeting of DPG and DPG-Tagung of the Condensed Matter Section 2021.

- *Imprinting the domain structure of a metallic antiferromagnet on thin ferromagnetic layers.*

S. P. Bommanaboyena, D. Schönke, M. Filianina, S. Yu. Bodnar, D. Backes, F. Maccherozzi, R. Reeve, M. Kläui & M. Jourdan.

Oral presentation - Intermag 2021.

- *Imprinting the antiferromagnetic domain pattern of Mn₂Au on thin ferromagnetic layers.*

S. P. Bommanaboyena, D. Schönke, M. Filianina, S. Yu. Bodnar, D. Backes, F. Maccherozzi, R. Reeve, M. Kläui & M. Jourdan.

Poster & flash presentation - The Joint European Magnetic Symposia (JEMS) 2020.

Contents

Abstract	13
Zusammenfassung	15
List of abbreviations	17
1 Introduction	21
1.1 Overview	25
2 Theoretical background	27
2.1 Antiferromagnetism	27
2.2 Antiferromagnetic Mn ₂ Au	28
3 Experimental techniques	33
3.1 Thin film deposition	33
3.1.1 RF magnetron sputtering	34
3.1.2 Molecular beam epitaxy (MBE)	34
3.1.3 AFM/FM bilayer architecture	35
3.2 Reflective high energy electron diffraction (RHEED)	36
3.3 Superconducting quantum interference device (SQUID) magnetometry	39
3.4 Scanning electron microscope with polarization analysis (SEMPA)	42
3.5 Kerr microscopy	44
3.6 Dichroism in magnetic materials	46
3.6.1 X-ray magnetic circular dichroism (XMCD)	46
3.6.2 X-ray magnetic linear dichroism (XMLD)	48
3.7 Photoemission electron microscopy (PEEM)	49
4 Results and discussion	51
4.1 Characterization of epitaxial Mn ₂ Au (001) thin films	51

4.2	Magnetic microscopy of Mn ₂ Au/FM bilayers	60
4.2.1	SEMPA based imaging of FM overlayers	60
4.2.2	XMLD-PEEM	65
4.3	Quantification of the exchange coupling strength in Mn ₂ Au/Py	68
4.4	Origin of the large coercive field of exchange coupled Py	71
4.5	Visualization of field-driven AFM/FM switching behaviour . .	76
5	Conclusions & future work	81
	Appendix*	85
	Bibliography[†]	89

**The reader is directed to additional information available in the appendix by a footnote wherever appropriate.*

[†]All references to the literary sources presented in this section are marked by numerals in [] within the main body of this thesis.

Abstract

The last few years have witnessed an emerging interest in building spin-electronics devices for memory and logic applications from antiferromagnets due to their highly favourable properties of external field stability, ultrafast magnetization dynamics etc. However, unless antiferromagnets are manipulated electrically, they cannot be effectively implemented in practical microelectronic devices that rival existing technologies, let alone supersede them. One of the proposed ideas is to use antiferromagnets with a special crystallographic symmetry (as found in Mn_2Au & CuMnAs) in memory bit cells. Theoretically, their unique structure enables their bi-stable magnetic order to be reversibly manipulated by short electrical pulses. This so called 'Néel spin-orbit torque' based switching of such antiferromagnets might require current densities comparable to values typically needed for the traditional spin-torque switching of ferromagnets. Though promising strides towards experimental proof were made in recent years, yet another challenge impeding the practicality of antiferromagnets remains to be tackled. Currently, the state of the antiferromagnet (upon reorientation of its magnetic order) is read via anisotropic magnetoresistance which is usually a tiny change of less than 1% in the resistance of the structure. However, the integration of a memory element into a functional CMOS circuit with a high signal to noise ratio (for good scalability) demands a significantly larger electrical readout. This work explores the growth of high quality epitaxial Mn_2Au (001) thin films and the exceptionally robust interfacial exchange coupling found in the $\text{Mn}_2\text{Au}/\text{Ni}_{81}\text{Fe}_{19}$ system. Such strongly coupled antiferromagnet/ferromagnet bilayers open up the possibility of generating large magnetoresistance effects via the ferromagnet for electrical readout while retaining the core advantages offered by the antiferromagnet. Furthermore, imprinting of the antiferromagnetic domain pattern on the ferromagnet facilitates its visualization via well established imaging techniques for ferromagnets. Additionally, it enables an in-house study of current induced switching of antiferromagnets while eliminating

the need for synchrotron based microscopy. Thus, this research will help make antiferromagnets more accessible by addressing some of the key issues identified in the quest for next generation spintronics devices based on these remarkable materials.

Zusammenfassung

In den letzten Jahren ist das Interesse an der Entwicklung von Spin-Elektronik-Bauelementen für Speicher- und Logikanwendungen auf der Grundlage von Antiferromagneten rapide angestiegen. Dies ist vor allem auf die äußerst vorteilhaften Eigenschaften von Antiferromagneten zurückzuführen, wie z. B. Stabilität in externen Feldern und ultraschnelle Magnetisierungsdynamik. Solange Antiferromagnete jedoch nicht elektrisch manipuliert werden, können sie nicht effektiv für mikroelektronische Anwendungen eingesetzt werden und dabei mit bestehenden Technologien konkurrieren bzw. diese ersetzen. Eine der vorgeschlagenen Ideen ist Antiferromagneten mit einer speziellen kristallographischen Symmetrie (wie sie in Mn_2Au und CuMnAs zu finden ist) in Speicherzellen zu verwenden. Theoretisch ermöglicht es ihre einzigartige Struktur, ihre bistabile magnetische Ordnung durch kurze elektrische Impulse reversibel zu manipulieren. Dieses sogenannte 'Néel-Spin-Bahn-Drehmoment' basierte Schalten von Antiferromagneten erfordert Stromdichten, welche mit denen für das traditionelle Spin-Drehmoment-Schalten von Ferromagneten vergleichbar sind. Obwohl in den letzten Jahren vielversprechende Fortschritte in Richtung eines experimentellen Nachweises gemacht wurden, gilt es noch eine weitere Herausforderung zu bewältigen, die die praktische Anwendbarkeit von Antiferromagneten erschwert. Gegenwärtig wird der Zustand des Antiferromagneten (bzgl. der Ausrichtung der magnetischen Momente) über den anisotropen Magnetowiderstand ausgelesen, der in der Regel eine kleine Änderung von weniger als 1% des Widerstands der Struktur darstellt. Die Integration eines Speicherelements in eine funktionale CMOS-Schaltung mit hohem Signal-Rausch-Verhältnis (für eine gute Skalierbarkeit) erfordert jedoch ein wesentlich größeres elektrisches Auslesesignal. Diese Arbeit erforscht das Wachstum hochqualitativer epitaktischer Mn_2Au (001)-Dünnschichten und die außergewöhnlich starke Austauschkopplung an der Grenzfläche im $\text{Mn}_2\text{Au}/\text{Ni}_{81}\text{Fe}_{19}$ System. Solche stark gekoppelten Antiferromagnet/Ferromagnet-Doppelschichten eröffnen

die Möglichkeit, über den Ferromagneten große Magnetowiderstandseffekte für elektrisches Auslesen zu erzeugen und gleichzeitig die wesentlichen Vorteile des Antiferromagneten beizubehalten. Darüber hinaus erleichtert das Einprägen des antiferromagnetischen Domänenmusters in den Ferromagneten dessen Visualisierung mit Hilfe etablierter Bildgebungsverfahren für Ferromagnete. Dies ermöglicht die Untersuchung des strominduzierten Schaltens von Antiferromagneten im Labor und stellt eine effiziente Alternative zur Synchrotron basierten Mikroskopie dar. Somit trägt diese Arbeit dazu bei, Antiferromagnete für die nächste Generation von Spintronik Anwendungen zugänglicher zu machen.

List of abbreviations

2DEG 2-dimensional electron gas.

AFM Antiferromagnet.

AMR Anisotropic magnetoresistance.

ARPES Angle-resolved photoemission spectroscopy.

CCD Charge-coupled device.

CMOS Complementary metal–oxide–semiconductor.

DC Direct current.

DOS Density of states.

EDX Energy dispersive X-ray spectroscopy.

FM Ferromagnet.

FY Fluorescence yield.

GMR Giant magnetoresistance.

HDD Hard disk drive.

ICP-OES Inductively coupled plasma optical emission spectroscopy.

ISGE Inverse spin galvanic effect.

LED Light emitting diode.

LEED Low energy electron diffraction.

MBE Molecular beam epitaxy.

MOKE Magneto-optic Kerr effect.

MTJ Magnetic tunnel junction.

NSOT Néel spin-orbit torque.

PEEM Photoemission electron microscopy.

PVD Physical vapour deposition.

Py Permalloy ($\text{Ni}_{81}\text{Fe}_{19}$).

RBS Rutherford backscattering spectrometry.

RF Radio frequency.

RHEED Reflective high energy electron diffraction.

SEMPA Scanning electron microscope with polarization analysis.

SHE Spin Hall effect.

SPLEED Spin-polarized low energy electron diffraction.

SQUID Superconducting quantum interference device.

STM Scanning tunneling microscopy.

STT-MRAM Spin transfer torque magnetic random access memory.

TEM Transmission electron microscopy.

TEY Total electron yield.

TMR Tunneling magnetoresistance.

UHV Ultra high vacuum.

XMCD X-ray magnetic circular dichroism.

XMLD X-ray magnetic linear dichroism.

XRD X-ray diffraction.

XRF X-ray fluorescence.

XRR X-ray reflectometry.

"Equipped with his five senses, man explores the universe around him and calls the adventure Science."

- Edwin P. Hubble
"The exploration of space"
Harper's Magazine - May 1929

1 Introduction

SPINTRONICS is the concept of engineering microelectronic devices that utilize the spin property of electrons together with their charge. Although it is a relatively young science, rapid advances in thin film magnetism coupled with the looming end of Moore's law[‡] have spurred researchers to look towards spin-based alternatives. These developments have shaped the field into a fine blend of condensed matter physics and electrical engineering.

Early spin-electronics devices primarily focused on a variety of magnetoresistance effects derived from ferromagnetic (FM) layers and the manipulation of ferromagnetic moments by spin polarized currents. Notable examples include the giant- and tunnelling magnetoresistance (GMR and TMR) based magnetic read heads of commercial hard disk drives (HDDs) [1] and the spin transfer torque magnetic random access memory (STT-MRAM) [1, 2]. The late 2000s ushered in a new era of relativistic phenomena based on the interplay between spin and orbital motion of electrons ('spin-orbitronics') such as the spin Hall effect (SHE), Rashba-Edelstein effect etc. [3] which gradually paved the way to a realm of 'antiferromagnetic spintronics'. The recent prediction and experimental realization of Néel order switching in antiferromagnets (AFMs) with a specific crystallographic symmetry (as in CuMnAs and Mn₂Au) using current induced 'staggered' spin-orbit fields [4–7] is a true testimony to the hitherto untapped potential held by AFMs.

[‡]In 1975 Gordon Moore (co-founder of Intel) predicted that the number of transistors on computer processors (which translates into their processing power) would double every two years. This laid the basis for a technology roadmap which the industry has faithfully adhered to ever since.

Reversible switching between two stable states using extremely short current pulses might enable these AFMs to be used for information storage as shown recently in a fully integrated memory device [8]. Moreover, attractive features such as insensitivity to large external magnetic fields, lack of stray fields and ultrafast magnetization dynamics (see section 2.1) provide strong motivation for the investigation of AFMs on par with FMs for next generation electronics.

Antiferromagnetic spintronics was kick-started in 2014 by the experimental observation of anisotropic magnetoresistance (AMR) in FeRh thin films by Marti et al. [9]. FeRh is an AFM which transitions to a FM phase at ≈ 100 K above room temperature. In the FM state it can be polarized along an easy axis with a sufficiently large magnetic field which defines the direction of the Néel vector when it is field-cooled back to the AFM phase. Hence, the AFM order can be reversibly set to any one of two distinct in-plane spin configurations allowed by the magnetocrystalline anisotropy of FeRh. The switching between these two AFM spin states is read via its intrinsic AMR of $\approx 0.3\%$, and therefore, FeRh functions as a memristor. Though it revealed a facet of antiferromagnets with technological potential, the use of heat and external magnetic fields severely limit the feasibility of this concept. Similar drawbacks were previously encountered in early generations of MRAM where complementary Oersted fields were generated by mutually orthogonal 'bit' and 'word' lines to toggle the recording layer of a memory cell [1]. The field was seen to cause unintentional writing of neighbouring bit cells in densely packed arrays, hindering the scalability of such devices. Therefore, electrical writing of information was deemed greatly desirable for practical applications. Though the manipulation of magnetic moments via electrical currents has been extensively investigated in FMs for more than two decades, it has very recently found its way into the previously unexplored territory of AFMs. One way is through interfacial spin-orbit torques exerted by pure spin currents injected from a heavy metal (HM) into an adjacent antiferromagnet as predicted in AFM/HM bilayers [10]. This technique is similar to the more conventional switching of magnetization via s-d exchange[§] in FM/HM systems [11, 12]. Another possibility is a bulk spin-orbit torque derived from the inverse spin galvanic effect (ISGE) and is exclusive to certain antiferromagnetic compounds which satisfy a set of crystallographic requirements explained below [4]. This aptly named Néel spin-orbit torque (NSOT) is capable of switching the Néel vector between two

[§]s-electrons from spin currents generated by the SHE in HMs like Pt, Ta etc. can transfer their momentum to local d-magnetic moments in an adjoining FM by exchange interaction. This can be modeled as an effective torque acting on the magnetization of the FM.

orthogonal easy axes and experimental reports of the same in CuMnAs [5] and Mn₂Au [6, 7] have opened up a whole new avenue of current induced spin manipulation. Centrosymmetric antiferromagnets in which the two magnetic sublattices form inversion partners while lacking a local spatial inversion symmetry themselves (figure 1.1.a) are needed to observe this phenomenon. Owing to this special structure an effective field alternating in sign with respect to the AFM sublattices (staggered field) is exerted on the moments lying on a magnetic easy axis by a current-driven along the same (figure 1.1.b) [4]. Consequently, the Néel vector is rotated by 90° towards the other easy axis (see section 2.2) and can be reversed via a second current pulse along this new axis. This bi-stability allows the encoding of binary information in the magnetic structure of the AFM, and therefore Mn₂Au and CuMnAs have drawn significant attention in recent years for next generation memory applications. Such memory bit cells could be operated by electrical pulses of

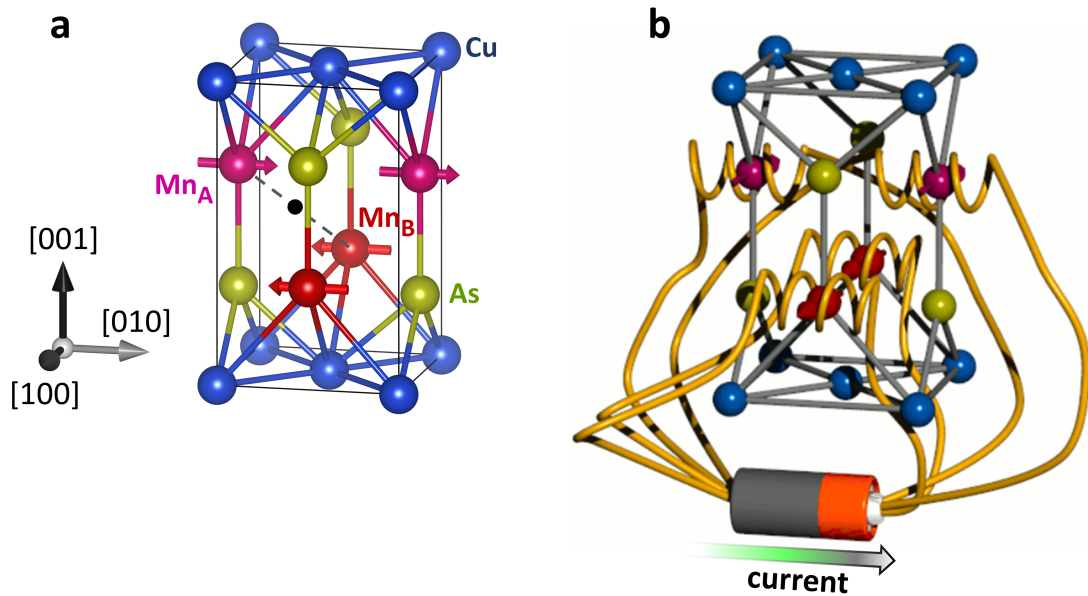


Figure 1.1. (a). Unit cell of CuMnAs. It is tetragonal with the spatial inversion centre represented by the black dot. Anti-parallel spin sublattices (M_A & M_B) form inversion partners with respect to this inversion point as indicated by the dashed lines. Additionally, the local environment of each Mn sublattice contains a broken structure inversion symmetry. The AFM easy axes are along [100] and [010]. (b). Oersted field analogy of NSOT. A current-driven through the coils exerts opposite Oersted fields (of equal magnitude) on alternate spins due to the opposite winding sense, similar to the staggered action of current-induced spin-orbit fields. Figure (b) modified from [13].

$\sim 10^6 - 10^7 \text{ A/cm}^2$ [5–8], comparable to current densities required to switch the storage layer in modern STT-MRAM devices [14]. Moreover, Mn₂Au is also considered to be a favourable option due to its large spin-flop transition

field, high Néel temperature [15] and lack of toxic elements.

Despite the identification of innovative means for electrical spin manipulation in AFMs, a major hurdle in their successful implementation in integrated circuits for memory devices persists in the form of their challenging readout. The intrinsic AMR of the antiferromagnet itself (typically a fraction of 1%) is insufficient, and therefore designing a readout circuit with a large signal to noise ratio would require the incorporation of more transistors for signal amplification. This not only complicates the circuit but also poses a threat to the scalability of microelectronic devices. This doctoral study makes it possible to envision a novel solution to the readout problem based on $\text{Mn}_2\text{Au}/\text{Ni}_{81}\text{Fe}_{19}$ (Permalloy or Py) bilayers. The Py magnetization perfectly mimics the underlying AFM domain pattern due to a strong mutual exchange coupling between the two layers combined with the specific atomic termination of Mn_2Au . The exchange coupling also mediates $\text{FM} \leftrightarrow \text{AFM}$ momentum transfer which compels the FM to replicate the new AFM domain structure even after the latter has been manipulated by fields or current-driven torque (detailed explanation in chapter 4). The bilayers can be additionally combined with another ferromagnet to build a magnetic tunnel junction (MTJ) with AFM/FM/tunnel barrier/fixed FM architecture which facilitates a TMR based readout. TMR is a large effect which can reach up to several hundred percent [16–18] and is also the standard readout mechanism in commercial STT-MRAM devices and magnetic read heads.

The first approach in the verification of current-driven switching of AFMs involved electrical transport measurements on lithographically patterned films [5–7]. Typically, writing pulse trains with amplitudes of $\sim 10^6 - 10^7 \text{A}/\text{cm}^2$ and spanning tens of milliseconds are injected into the structure, followed by a measurement of its transverse or longitudinal resistance using a small DC probe current. Zig-zag changes in this readout signal corresponding to forward and reverse switching pulses are commonly interpreted as magnetoresistance arising from re-orientation of the AFM moments with respect to the probe current. However, recent experiments by Chiang et al. [19] and Matalla-Wagner et al. [20] have suggested that such resistance changes can also stem from thermal voltages and local variations in the resistivity of the patterned structure at high current densities. The identification of such deceptive signals of a non-magnetic origin calls for further corroboration of transport experiments by suitable magnetic microscopy. Until now, photoemission electron microscopy (PEEM) combined with X-ray magnetic linear dichroism (XMLD) has been the most

commonly applied method in this investigation [21, 22]. Though effective, it often involves cumbersome measurements at a synchrotron light source with a low success rate. This work presents an easier alternative to synchrotron microscopy based on the perfect imitation of Mn_2Au domains by an exchange coupled Py overlayer. Thus, in-house visualization of AFM domains is made possible using relatively simple techniques for FMs such as scanning electron microscopy with polarization analysis (SEMPA) and Kerr microscopy. Therefore, AFM/FM heterostructures will take us a step further towards realization of practical microelectronic devices based on AFMs. Additionally, they will aid in the extensive in-house examination of current driven switching of AFMs to harness their immense potential.

1.1 Overview

This PhD thesis investigates the synthesis and characterization of epitaxial Mn_2Au (001) thin films and the physics of interfacial exchange coupling in $\text{Mn}_2\text{Au}/\text{Ni}_{81}\text{Fe}_{19}$.

Chapter 2 establishes the fundamental theory behind the phenomenon of antiferromagnetism and the special features exhibited by antiferromagnetic Mn_2Au .

Chapter 3 deals with the experimental methods employed by this study for thin film deposition, material characterization and imaging of both FM and AFM domain structure.

Chapter 4 discusses the results of epitaxial Mn_2Au (001) thin film growth optimization and subsequent magnetic characterization of $\text{Mn}_2\text{Au}/\text{Ni}_{81}\text{Fe}_{19}$ bilayers.

Chapter 5 outlines the conclusions drawn from various experiments and talks about possible future work.

The Appendix provides the reader with additional information on selected topics for a better understanding.

The Bibliography lists the literary sources which were referred to during this study.

2 Theoretical background

2.1 Antiferromagnetism

Antiferromagnets are magnetic materials that can be regarded as being comprised of two or more interpenetrating ferromagnetic sublattices which mutually cancel to generate an overall zero magnetic moment. Though initially thought to be impractical[¶] [23], several potential advantages offered by them over FMs for spin-electronics applications have been identified in recent years. These are summarized in table 2.1.

Table 2.1: Ferromagnets vs. antiferromagnets.

	Ferromagnets	Antiferromagnets
Stray fields	Large	None
External field stability	Poor	Very high
Magnetization dynamics	GHz	THz

Despite the presence of a global magnetic order, AFMs possess no net magnetization, and therefore do not generate stray fields unlike FMs. Thus, AFM bit cells might lead to higher density information storage compared to their FM counterparts which run the risk of influencing each other when placed in close proximity, leading to 'false writes'. Moreover, FM based memory devices are vulnerable to inadvertent erasure by external magnetic

[¶]"They (antiferromagnets) are extremely interesting from the theoretical standpoint but do not appear to have any practical applications." - Louis Néel (Nobel lecture - December 11, 1970).

fields. In contrast, AFMs neatly sidestep this issue owing to their low magnetic susceptibility and large spin-flop transition fields. The speed of magnetic microelectronics is limited by the resonance frequency f_{FMR} of the switching layer. In FMs this value largely depends on the anisotropy field ($\sim 10 - 10^2$ mT) and does not exceed GHz frequencies. It is given by the Kittel formula [24]:

$$f_{FMR} = \frac{\gamma}{2\pi} \sqrt{B_{an}(B_{an} + \mu_0 M_s)} \quad (2.1)$$

where γ , B_{an} , M_s , μ_0 represent gyromagnetic ratio, anisotropy field, saturation magnetization and permeability of free space respectively. AFMs on the other hand are capable of much faster magnetization dynamics as the resonance frequency f_{AFMR} is dominated by the exchange field B_{ex} experienced by their constituent magnetic sublattices (figure 2.4.a). It is expressed as [24]:

$$f_{AFMR} = \frac{\gamma}{2\pi} \sqrt{B_{an}(B_{an} + 2B_{ex})} \quad (2.2)$$

Though both anisotropy and exchange fields are comparable in FMs and AFMs, the dependance of f_{AFMR} on B_{ex} (typically $\sim 10^3 B_{an}$ [25]) leads to frequency values in the THz regime. Thus, AFMs are expected to play a crucial role in the search for new technologies aimed at fulfilling the perennial demand for denser, faster and robust devices.

2.2 Antiferromagnetic Mn_2Au

Mn_2Au is a metallic, collinear and layered AFM (figure 2.1) which exhibits a particular set of symmetry conditions that permits current-driven Néel spin-orbit torques within the bulk of the crystal. Presently, it is one of the only two materials known to be capable of hosting this phenomenon (the other being $CuMnAs$). Mn_2Au is a centrosymmetric compound where any Au site can be considered to be the global inversion center while the two magnetic sublattices (Mn_A and Mn_B) form inversion partners. Despite being conserved overall, the inversion symmetry is seen to vanish with respect to the Mn sublattices. The microscopic mechanism at the heart of NSOT is explained in detail below.

Non-equilibrium spin polarization generated at interfaces owing to a loss of structure inversion symmetry has piqued the interest of researchers since the discovery of current-driven magnetization reversal in FM/HM systems [26]. Better known as the inverse spin galvanic effect (a.k.a the

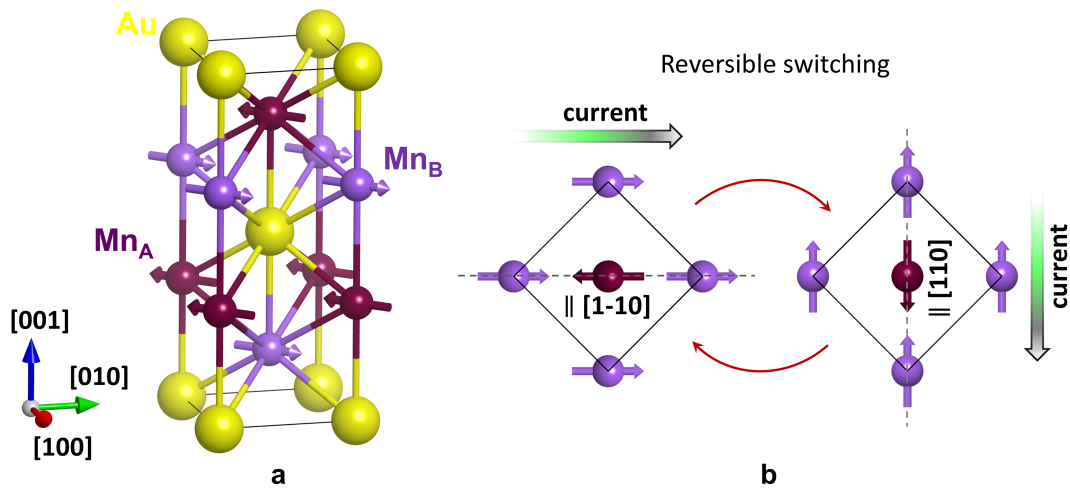


Figure 2.1. (a). Unit cell of Mn_2Au . The central Au atom serves as a spatial inversion point for the unit cell. Mn_A and Mn_B are observed to be inversion partners with respect to it. Every Mn_A or Mn_B site is located midway between a pair of Au and Mn (dissimilar) atoms along $[001]$. Therefore, the Mn sites do not serve as global inversion centres (non-centrosymmetric magnetic sublattices). (b). Current-induced switching of AFM order in Mn_2Au . The two orthogonal easy axes are represented by dotted lines. The AFM moments can be reversibly switched between these two spin states via NSOT.

Edelstein- or Rashba-Edelstein effect) [27, 28], this phenomenon is considered to be one of the several possible mechanisms contributing to interfacial spin-orbit torques (as explained in figure 2.2) [29]. Subsequently, the ISGE was also found to be active inside FMs with a Zinc-blende structure like GaMnAs which intrinsically lack global spatial inversion symmetry within their bulk [30]. Similarly, an ISGE-spin density was shown to exert an exchange mediated bulk torque on the background ferromagnetic order of the half-Heusler NiMnSb, causing it to switch reversibly [31].

The theory was eventually extended to AFMs such as Mn_2Au and CuMnAs which display the requisite structural symmetry described earlier. Although in this case, the net spin polarization induced by a current over the whole crystal is zero due to its centrosymmetric nature, opposite non-zero spin densities can be found locally on the inversion asymmetric magnetic sublattices (figure 2.3). The spin polarization of the conduction electrons on each sublattice couples to it over a short range [32], resulting in a torque on the AFM moments. This interaction can be effectively modeled as an in-plane transverse staggered field as depicted in figure 2.4.b. A combined action of the consequent NSOT and exchange torque reversibly rotates the AFM order between the two magnetic easy axes [33]. Thus, switching via NSOT involves

a single active layer, i.e., the AFM itself unlike other means of electrical spin manipulation which require additional layers for generation of pure spin- or spin-polarized currents. This might aid in designing relatively simpler AFM spintronics device architectures for memory and logic applications.

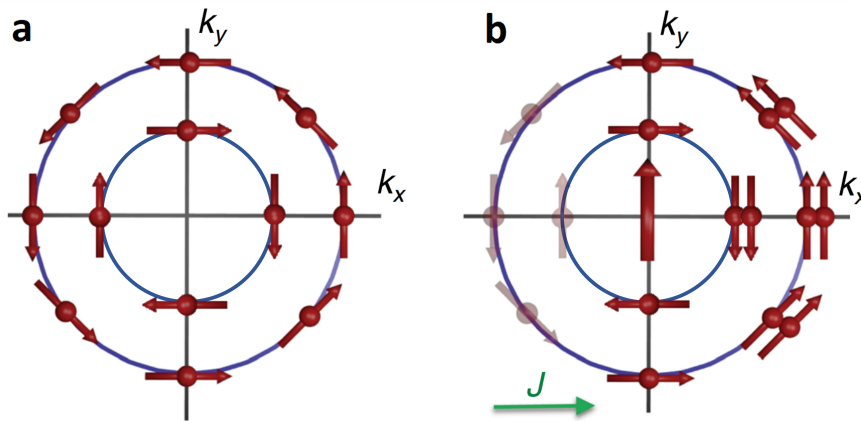


Figure 2.2. (a). 2-dimensional equilibrium Fermi contour of a conductor at an interface or surface. k_x and k_y represent momentum components. Relativistic conduction electrons moving through the out-of-plane electric field induced by an absence of inversion symmetry experience an additional magnetic field in their reference frame which tends to orient them perpendicular to their momentum (Rashba spin-orbit coupling)^{||}. (b). Inverse spin galvanic effect. An in-plane electric field is applied externally along the x-direction to drive a current J as indicated by the green arrow. The charge carriers are redistributed in momentum space (to the right) as they are subjected to acceleration in the applied field together with momentum scattering and k -dependant asymmetric spin-flip scattering events** [34] (depletion of electrons on the left side of the k_y axis is represented by transparency). This leads to an overall increase in the population of electrons with a spin up component (The inner and outer bands produce opposite effects but the latter dominates due to its larger radius). Thus, a net in-plane spin \uparrow polarization is generated $\perp J$ which can excite magnetization dynamics in a neighbouring FM via exchange interaction. Figure modified from [3].

^{||} Please see Appendix 1: 'Rashba spin texture' for a full derivation.

^{**} Please see Appendix 2: 'Non-equilibrium distribution of charge carriers'.

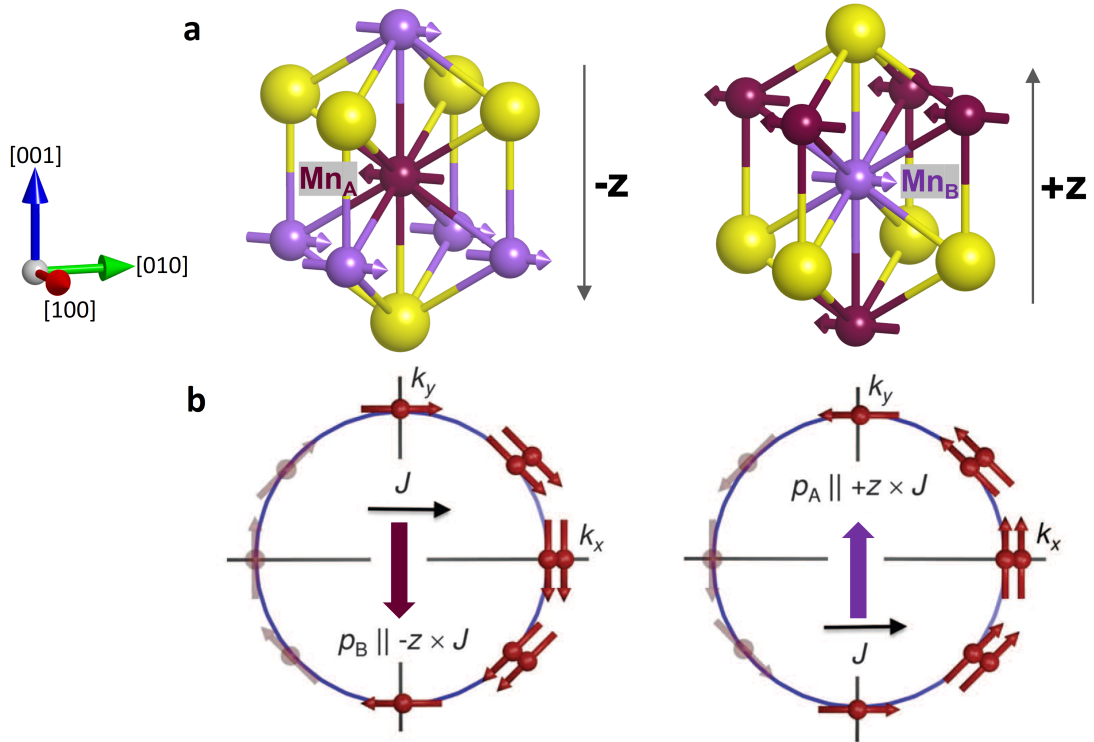


Figure 2.3. (a). Local environments of Mn_A (left) and Mn_B (right) in the crystal structure of Mn₂Au. Any given Mn_A atom has four Au (heavy) atoms above it while it has four Mn (light) atoms below. This asymmetric distribution generates a gradient in electric potential across the sublattice-A. Similarly, a potential gradient of the same magnitude is also built up across sublattice-B but with an opposite sign. This is a direct consequence of the two magnetic sublattices being inversion partners with respect to the global inversion centre^{††}. Therefore, they experience opposite electric fields $\pm z$ generated by the local inversion asymmetry. (b). Non-equilibrium distribution of charge carriers on different sublattices within the bulk of Mn₂Au (only the outer band is shown). An applied in-plane electric field drives a current J through the AFM as illustrated. Opposite spin polarizations $p_A \uparrow$ and $p_B \downarrow$ of equal magnitude are induced on Mn_A and Mn_B respectively as a result of $\pm z$. Figure (b) modified from [5].

^{††} Similarly, the Mn_A sites in CuMnAs have four Cu atoms above and an As atom below (viewed along [001]) while the reverse is true for their inversion partner Mn_B sites (see figure 1.a). This asymmetry produces local electric fields along the hard axis which alternate in sign with respect to the magnetic sublattices.

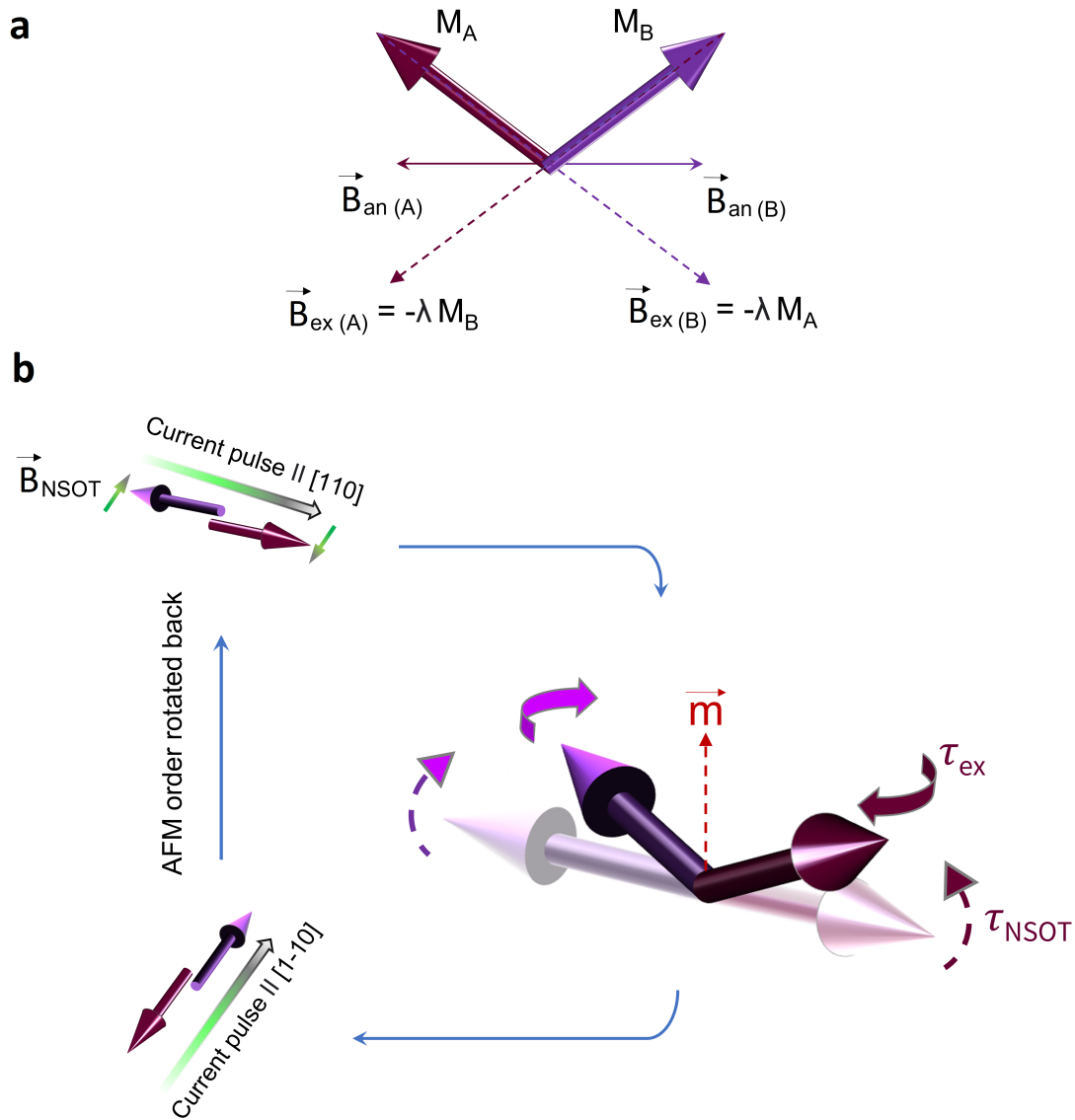


Figure 2.4. (a). Intrinsic fields acting on AFM moments M_A and M_B when canted with respect to the easy axis. Each sublattice feels an exchange force or molecular field \vec{B}_{ex} from the opposite sublattice (λ is a positive constant) [24]. The anisotropy fields \vec{B}_{an} act along the easy axis. (b). Effect of NSOT on the AFM order. A charge current-driven along the easy axis [110] exerts staggered spin-orbit fields \vec{B}_{NSOT} on the magnetic sublattices. The resultant torque $\tau_{NSOT} = -M \times \vec{B}_{NSOT}$ [35] tends to tilt the AFM moments out of plane (indicated by dashed arrows) to generate a net magnetic moment \vec{m} . Subsequently, the magnetic sublattices experience an exchange torque τ_{ex} given by $-M \times \vec{B}_{ex}$ which rotates them about \vec{m} as indicated by the bold arrows. τ_{NSOT} vanishes upon a 90° rotation of the moments with respect to the injected current. Consequently, the moments relax back to an equilibrium in-plane configuration, thereby nullifying τ_{ex} to prevent further precession. The Néel vector can be switched back with a second current pulse applied along [1-10].

3 Experimental techniques

3.1 Thin film deposition

Previously, all available Mn_2Au thin films were grown either by molecular beam epitaxy (MBE) in the (101)-orientation [36] or by sputtering in the (001)- [7, 37, 38], (110)-[38], (103)-, (101)-, and (204)-orientations [39]. However, (001)-axis grown films are favourable to observe NSOT switching as, in this case, the quasi-easy plane is parallel to the substrate plane. (001)-oriented Mn_2Au thin films were first grown by Jourdan et al. [37] via RF magnetron sputtering from a stoichiometric target onto epitaxial Ta (001) buffer layers deposited on r-plane Al_2O_3 substrates. The films were found to be quasi-epitaxial with a relatively rough morphology. Meinert et al. also reported epitaxial Mn_2Au (001) thin films grown by DC magnetron co-sputtering of Au and Mn onto epitaxial ZrN (001) buffer layers deposited on MgO (001) substrates [7]. Unfortunately, they found a trade-off between the morphology of the thin film and its crystallinity. Good crystal quality is required for large NSOT, AMR and to study the band structure of materials using photoemission while smooth surface features are important to observe NSOT-induced AFM domain wall motion. During the course of this study, these problems were overcome by improving upon the previous growth recipe of Jourdan et al. [37]. Mn_2Au thin films were deposited using the standard physical vapour deposition (PVD) techniques of MBE and magnetron sputtering and a post-deposition annealing step was incorporated into the fabrication procedure in both cases. The films were subjected to various characterization procedures to understand their crystallographic phase, topography and composition.

10×10×0.53 mm sized, single side polished r-plane Al₂O₃ substrates from CrysTec GmbH were used for all the samples prepared for this PhD project. Prior to deposition the substrates were annealed in ultra high vacuum (UHV) at 550 °C for at least 30 minutes to get rid of adsorbed water and organic contamination. Mn₂Au has a tetragonal structure with $a = 3.32 \text{ \AA}$ and $c = 8.53 \text{ \AA}$. Body centred cubic Ta has a lattice constant of 3.30 \AA , and therefore serves as an ideal buffer layer for Mn₂Au (001) due to the small lattice mismatch of 0.6% (explained further in chapter 4). Further details pertaining to sample preparation are presented in the following subsections.

3.1.1 RF magnetron sputtering

The base pressure of the sputtering chamber used is 1.5×10^{-8} mbar. First, a 13 nm thick epitaxial Ta (001) buffer layer was deposited on Al₂O₃ (1 $\bar{1}$ 02) at 450 °C via RF magnetron sputtering, following which the sample was cooled to 300 °C. Mn₂Au was then sputtered from a stoichiometric target at 0.1 mbar Ar pressure with a deposition rate of 0.75 \AA/s to obtain a thin film of desired thickness. Subsequently, the sample was annealed at 450 °C for 60 minutes. Both temperature and duration of this post-deposition annealing step were found to be crucial for the formation of a smooth and well-ordered Mn₂Au crystal.

3.1.2 Molecular beam epitaxy (MBE)

The growth of a thin film by MBE involves the co-evaporation of its constituent elements from separate sources. First, a 13 nm thick epitaxial Ta (001) buffer layer was deposited on Al₂O₃ (1 $\bar{1}$ 02) at 450 °C via RF magnetron sputtering. The sample was then transferred to the MBE chamber under UHV conditions. Subsequently, a Mn₂Au film of desired thickness was grown over the Ta buffer by co-evaporation of high purity Mn and Au from two different evaporation sources in high vacuum. The base pressure of our MBE chamber is 7×10^{-10} mbar while the working pressure is 1×10^{-7} mbar. Mn was sublimated from a high temperature effusion cell with a stable evaporation rate which was predetermined by XRR analysis of a pure Mn film. An electron beam evaporator was used to evaporate Au and its rate was continuously monitored during deposition using an oscillating quartz crystal monitor. Mn and Au were simultaneously deposited onto r-plane Al₂O₃/13 nm Ta (001) at a rate of 0.23 \AA/s and 0.15 \AA/s respectively (corresponding to a ratio of

1.5:1) which results in stoichiometric Mn_2Au as explained further in the next chapter. The substrate temperature was maintained at 270°C during deposition. The MBE films were also subjected to the same post-deposition annealing step as the sputtered samples as explained in subsection 3.1.1.

3.1.3 AFM/FM bilayer architecture

The AFM/FM bilayers used for this study were fabricated by depositing a thin film of Fe or Py via RF magnetron sputtering over Mn_2Au (001) at room temperature. Previous work by Sapozhnik et al. [40] found the AFM easy axes of Mn_2Au to be oriented along the diagonals of the unit cell as shown in figure 3.1.

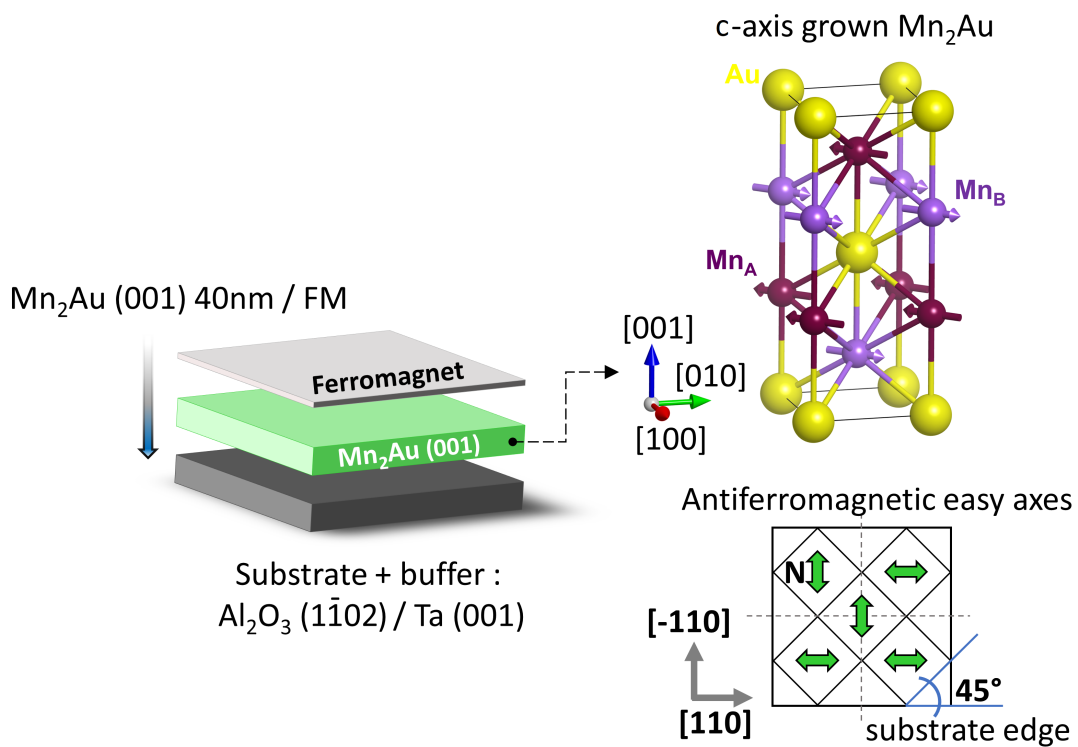


Figure 3.1. The basal plane of the c -axis grown Mn_2Au unit cell is rotated by 45° with respect to the edge of the substrate (confirmed using an XRD ϕ -scan). The AFM moments (marked 'N') are represented by double headed green arrows lying along $[110]$ and $[\bar{1}\bar{1}0]$ crystallographic directions which makes them parallel to the edges of the substrate.

3.2 Reflective high energy electron diffraction (RHEED)

The standard technique of X-ray diffraction (XRD) was used throughout the course of this study for bulk crystallographic analysis of Al_2O_3 ($1\bar{1}02$)/Ta (001)/ Mn_2Au (001) heterostructures. However, one often needs an additional surface sensitive technique to investigate the crystalline order of the uppermost atomic layers sans bulk (especially when interfaces are of interest). RHEED utilizes the scattering of electron waves by atoms constituting the surface of a crystal to form a diffraction pattern (similar to light in case of XRD) which reveals its structural features. Information is gathered only from the topmost atomic planes as the primary electrons are incident onto the sample at a grazing angle of $\sim 0.5^\circ - 6^\circ$ [41] which ensures that they do not interact with its bulk (hence the term 'reflective').

A 2-dimensional lattice in real space can also be viewed as being 3-dimensional with the same in-plane lattice constants but an infinitely large out-of-plane lattice parameter (the next plane is considered to be infinitely far away). This results in a shrinking of the corresponding reciprocal lattice vector to an infinitesimal value. Therefore, in case of a 2D crystal (for example, the surface of an epitaxial thin film), the reciprocal lattice points in the out-of-plane direction are no longer discrete but merge to form continuous 'rods' that are infinitely long as depicted in figure 3.2. Typically, the primary electrons employed in RHEED have an energy ~ 20 KeV (wavelength ≈ 0.08 Å). The electron wave vector \vec{K} is expressed as:

$$\vec{K} = \frac{2\pi}{\lambda} \quad (3.1)$$

where λ is the de Broglie wavelength and is given by $\lambda = h/m_e v$ (h , m_e and v are the Planck's constant, electron mass and electron velocity respectively). The incident electron waves are scattered elastically by surface atoms, resulting in spherical secondary electron waves. Thus, both initial and final electron wave vectors (\vec{K}_i and \vec{K}_f respectively) have the same magnitude. Similar to the case of X-ray diffraction from bulk crystals, constructive interference of these secondary electron waves is observed in those directions of \vec{K}_f for which the scattering vector $\vec{\Delta K} = \vec{K}_f - \vec{K}_i$ is equal to a reciprocal lattice vector (Laue condition) [42]. These directions can be found using a sphere drawn in reciprocal space with a radius of $|\vec{K}_i|$ ($= |\vec{K}_f|$) as illustrated

in figure 3.3.a. Vectors joining the centre of this so-called 'Ewald sphere' to reciprocal lattice points lying on its surface fulfill the Laue condition.

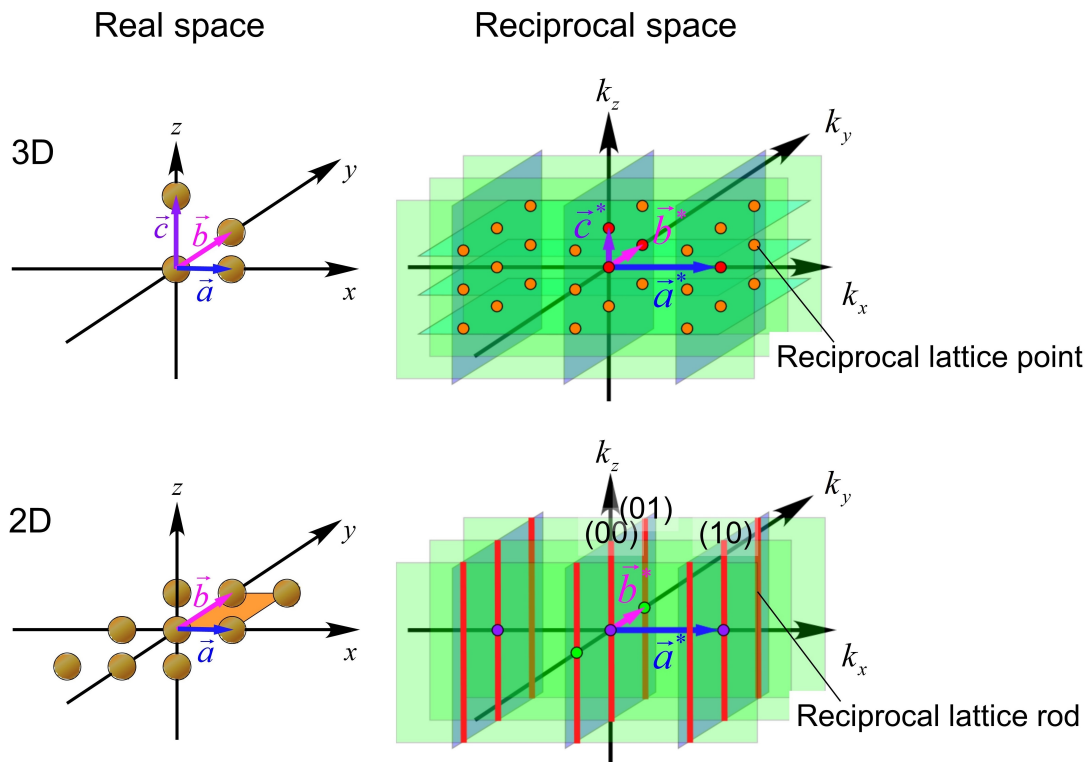


Figure 3.2. Reciprocal lattices of 3D and 2D crystals. \vec{a} , \vec{b} and \vec{c} represent the lattice vectors in real space while \vec{a}^* , \vec{b}^* and \vec{c}^* represent the corresponding reciprocal lattice vectors. The reciprocal lattice of a 2D crystal is comprised of infinitely long rods arranged on planes with the interplanar spacing defined by \vec{a}^* and \vec{b}^* . Figure modified from [43].

As the Ewald sphere intersects planes of reciprocal lattice rods along circles, the diffraction spots are found to be arranged on semi-circles in case of an atomically flat epitaxial thin film (figure 3.3.b). The presence of multiple crystallographic domains at a surface broadens its reciprocal lattice rods, causing them to intersect the Ewald sphere in ellipses which appear as streaks when projected on to the RHEED pattern (as $|\vec{K}_i|$ is much larger compared to the radius of a rod, a small region on the Ewald sphere can be considered to be a plane). The reciprocal lattice of a sample with a rough island-like morphology (for instance, a thin film following a Volmer-Weber growth mode) is composed of discrete points as the surface is 3-dimensional, and therefore the semi-circular RHEED pattern is lost.

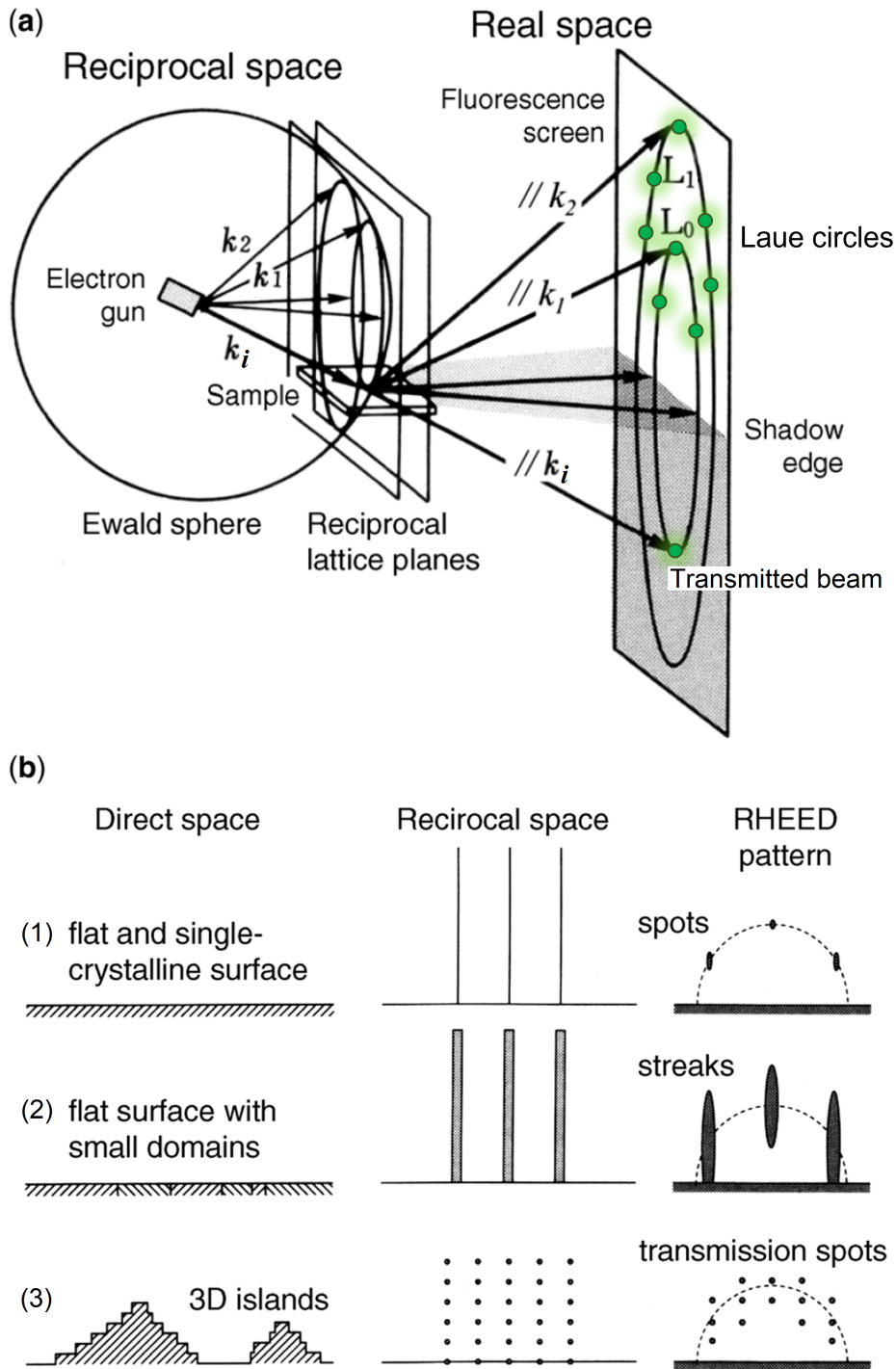


Figure 3.3. a. 3D view of a typical RHEED setup. Primary electrons with a wave vector of \vec{k}_i are generated by an electron gun. \vec{k}_1 and \vec{k}_2 are examples of \vec{k}_f which meet the Laue condition. The diffraction spots observed on the fluorescent screen are arranged on concentric 'Laue circles' (The 0th (L_0) and 1st zones (L_1) are shown here). b. RHEED patterns corresponding to commonly found thin film morphologies. Only the 0th Laue zone is shown in each case. Figure modified from [41].

RHEED spots are sometimes accompanied by additional features known as 'Kikuchi lines' which aid in understanding the crystalline order of the given sample. A fraction of the incident electrons is scattered in-elastically by atoms in the bulk of the crystal, sending out secondary waves in all directions. These secondary electron waves are diffracted by bulk lattice planes at angles where the Bragg condition is satisfied, leading to distinct sharp lines along certain directions in the RHEED patterns of single crystals. In contrast, polycrystalline samples generate lines in all directions due to a randomized distribution of the constituent crystallites, thereby creating a homogeneous background.

3.3 Superconducting quantum interference device (SQUID) magnetometry

During the course of this study, a SQUID magnetometer was used to quantify the exchange coupling strength at the Mn₂Au/Py interface. It is a highly precise instrument which exploits superconducting phenomena, namely the Josephson effect and flux quantization to measure extremely tiny magnetic moments and is ideal for thin film samples.

A DC SQUID consists of two superconducting Josephson junctions (a normal conductor or insulating barrier sandwiched between two superconductors) connected in parallel to form a loop as shown in figure 3.4.a. The loop conducts a supercurrent despite the presence of non-superconducting links because the constituent Cooper pairs can tunnel through them (Josephson effect) analogous to charge carriers in normal conductor-insulator based tunnel junctions. Any superconducting loop permits only integral multiples of one flux quantum ϕ_0 through itself (flux quantization).

$$\phi_0 = \frac{h}{2e} \quad (3.2)$$

Where h and e stand for the Planck's constant and charge of an electron respectively. It is this quantum mechanical phenomenon which is at the heart of a SQUID magnetometer's high sensitivity. Any external field acting upon the SQUID induces a screening current I_S whose magnitude and direction ensure that the net magnetic flux through the loop is always an integral multiple of ϕ_0 . For instance, for values of ϕ less than $\frac{\phi_0}{2}$, I_S flows such that it opposes ϕ and nullifies the overall flux through the loop. If the magnitude of ϕ

is raised to be larger than $\frac{\phi_0}{2}$, I_S does not increase further to continue opposing the applied flux. Instead, it changes direction to support ϕ by generating an overall flux of $1\phi_0$ (lesser current is energetically more favourable) in accordance with flux quantization. Thus, the reversible circulation of I_S results in its cyclic variation with the applied flux with a period of ϕ_0 as illustrated in figure 3.4.b. The presence of I_S also lowers the current that can be applied to the junctions without the appearance of a voltage or 'critical current' (figure 3.4.c), thereby altering the current-voltage (I-V) characteristics of the SQUID as shown in figure 3.5.a.

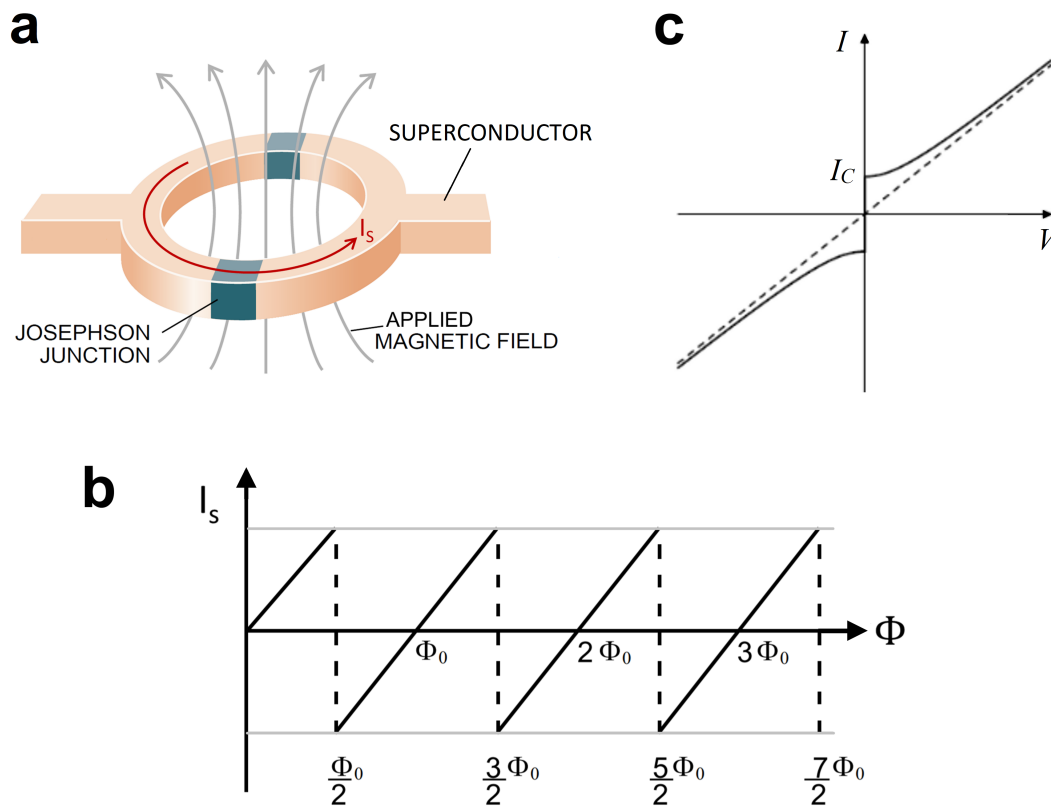


Figure 3.4. a. A DC SQUID loop comprising of two Josephson junctions. b. The direction and magnitude of I_S depend on the flux ϕ generated by the applied field. c. Current (I) vs. voltage (V) characteristics of a Josephson junction or 'weak link' in the absence of external flux. I_C is the critical current beyond which the junction becomes resistive. It should be noted that the critical current of a SQUID is twice that of a single Josephson junction which itself is smaller than the critical current of the constituent superconductor. The dashed line represents the Ohmic behaviour of the junction upon a complete loss of superconductivity at higher currents. Figures modified from [44–46].

When implemented in a magnetometer, a fixed bias current slightly exceeding its critical current is applied to the SQUID such that a voltage

can always be measured across it. When a bias current is passed through the SQUID, it flows parallel to the screening current in one arm while it is anti-parallel to the same in another arm. If the addition of screening- and bias currents in the former arm causes the junction to become resistive, all the bias current tends to flow through the latter, making it resistive. This implies that the maximum bias current which can now be applied without causing a voltage to develop is lowered by $2I_S$ compared to the value when no screening current is present, i.e., I_C . Thus, the critical current hits a minimum I'_C when the screening current is maximum, i.e., at half integer multiples of ϕ_0 . The dependence of I-V characteristics on I_S causes the monitored SQUID voltage to vary continuously with applied flux in the presence of a constant bias current as shown in figure 3.5.b. The voltage oscillates between two well defined values (V_{\min} and V_{\max}) with a period of ϕ_0 , similar to the case of I_S seen earlier in figure 3.4.b. Hence, a change in ϕ can be ascertained by simply measuring the corresponding change in voltage. As the SQUID takes in magnetic flux as input to generate a measurable voltage output, it is often described as a 'flux to voltage transducer' [44].

Usually, in a practical magnetometer the sample does not interact directly with the SQUID, but instead it is moved through pick-up coils which transfer the flux to the SQUID via a transformer [44]. A simplified design is depicted in figure 3.5.c. The pick-up coils are positioned inside a superconducting magnet which can apply a field to the sample if needed (for example, to study ferromagnetic hysteresis). The SQUID is placed away from this arrangement in a magnetically shielded region to avoid being influenced by the applied field.

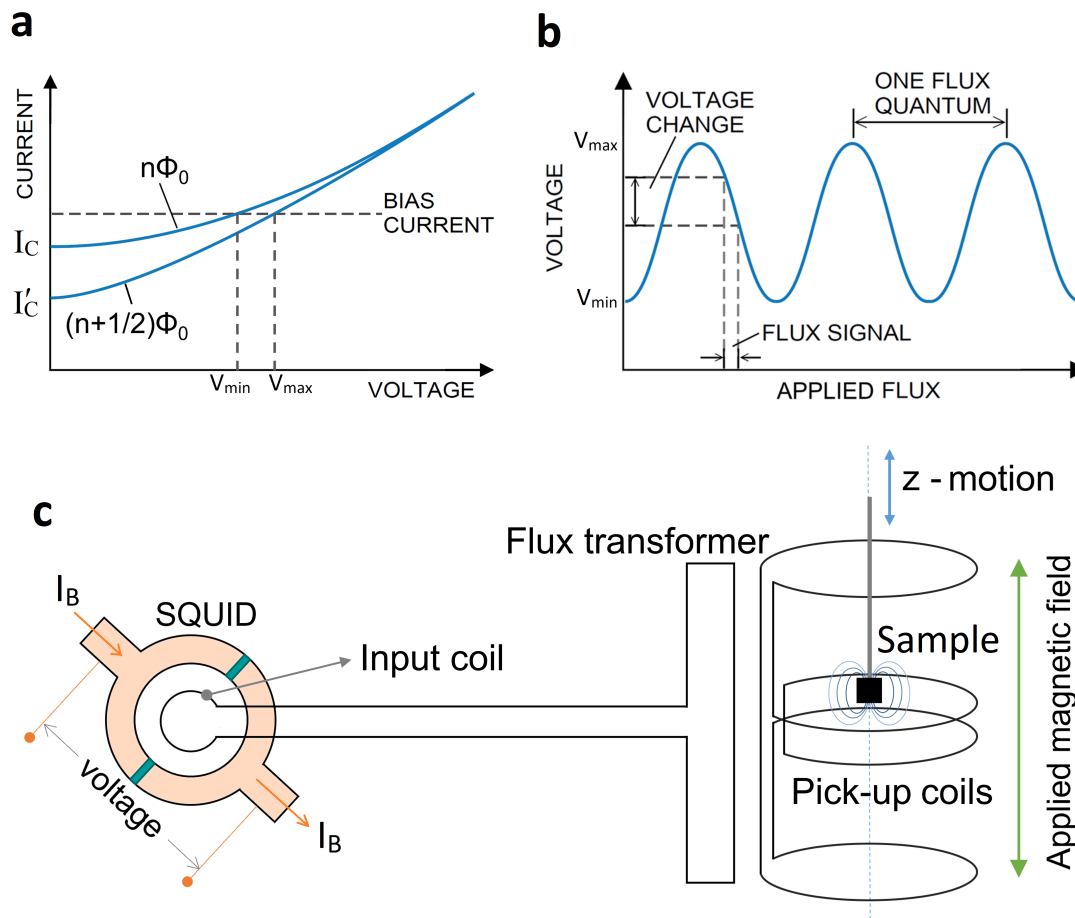


Figure 3.5. a. Current vs. voltage characteristics of a SQUID in the presence of applied flux. The screening current induced whenever the flux is not an integer (n) multiple of ϕ_0 lowers the critical current. b. Periodic variation of the measured voltage with applied flux. c. In a magnetometer the sample is moved through pick-up coils such that its magnetic field generates a current which is transferred to an input coil via a flux transformer. An external field can be applied to the sample using a superconducting magnet (not shown here) perpendicular to the plane of the pick-up coils. The field generated by the input coil acts upon the SQUID which delivers a voltage signal to deduce the magnetic moment of the given sample. Figures a and b modified from [44].

3.4 Scanning electron microscope with polarization analysis (SEMPA)

Scanning electron microscopy (SEM) is a well established surface sensitive technique used to construct topographical images with high spatial resolution. The microscope scans an unpolarized beam of primary electrons across a given sample and counts the secondary electrons emitted from each spot. The

variation in this measured intensity across the sample provides information on its surface features as secondary electron emission is morphology dependant. The SEMPA (a.k.a spin-SEM) is additionally equipped with a spin detector to analyze the intrinsic angular momentum of these outgoing secondary electrons. The local electronic density of states (DOS) of any region on the sample with a net magnetic moment (for example, a ferromagnetic domain) is inherently asymmetric with respect to the two spin channels (exchange splitting) as depicted in figure 3.6.a. Therefore, the population of secondary electrons ejected from such an area is spin-polarized. The electrons are released from a broad binding energy range and undergo spin dependant scattering inside the detector at the W (001) spin-polarized low energy electron diffraction (SPLEED) single crystal [47, 48] (figure 3.6.b). Channeltrons (electron multipliers) positioned at LEED spots count the number of deflected electrons to measure the spin-polarization (and hence magnetization direction) of the region being scanned. The spin polarization P is given by:

$$P = \frac{N_{\uparrow} - N_{\downarrow}}{N_{\uparrow} + N_{\downarrow}} \quad (3.3)$$

where N_{\uparrow} and N_{\downarrow} stand for the number of up and down spin electrons respectively. This enables SEMPA to map out the domain structure of ferro- and ferrimagnetic samples with a lateral spatial resolution of ≈ 30 nm. Using two mutually orthogonal channeltron pairs, any in-plane magnetization can be observed by resolving it into horizontal and vertical components. The entire process is carried out in UHV (typically, in $\sim 1 \times 10^{-10}$ mbar pressure). The W single crystal needs to be heated periodically to a high temperature of ≈ 2300 K for a few seconds (a process referred to as 'flash cleaning') to get rid of oxidation and other adsorbed impurities which degrade its spin distinguishing capability.

This technique does not allow for the direct imaging of antiferromagnets as they lack a net spin-polarization. However, as a Py overlayer is found to exactly copy the domain pattern of Mn_2Au , it serves as a guide for the in-house visualization of AFM domains using SEMPA. Moreover, XMLD-PEEM, which is the most commonly deployed technique for imaging AFMs, fails to resolve 180° domains due to them being aligned to the incident X-ray electric field vector at the same angle (explained further in section 3.4.2). SEMPA on the other hand can easily distinguish these domains owing to their opposite spin polarization, thereby rendering it an ideal tool to probe our bilayer system in the as-grown state. However, as the SEMPA does not provide large magnetic fields in-situ, Kerr microscopy was used to image the

Py layer at various points along its ferromagnetic hysteresis loop as described in the next section.

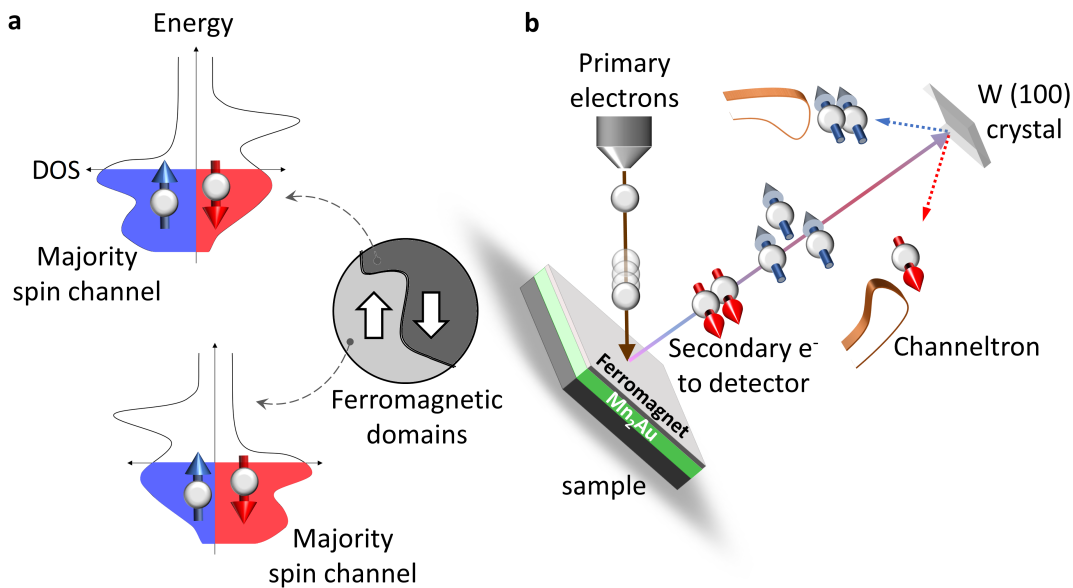


Figure 3.6. a. Density of electronic states in two FM domains separated by a 180° domain wall. b. SEMPA operation principle. The sample stage is tilted such that the primary electron column makes an angle of 60° with respect to the sample plane while the detector axis is collinear with the sample normal. The primary electron beam is rastered across the region shown in (a). Up and down spin secondary electrons are scattered asymmetrically by the W (001) crystal towards opposite channeltrons where they are counted to obtain the spin polarization of the scanned area. Thus, the two domains are resolved due to their opposite spin polarization. Similarly, left and right spins are also deflected asymmetrically and counted by another set of channeltrons orthogonal to the pair shown here. Both horizontal and vertical magnetization components are acquired simultaneously. Morphological information is also obtained from the sum of electrons received by all four channeltrons.

3.5 Kerr microscopy

This technique relies on the magneto-optic Kerr effect (MOKE) which describes the change in polarization of light when it interacts with a ferromagnetic material. The observed change is dependant on the sample's band structure as well as the relative orientation of its magnetization and polarization of incident light. The phenomenon can be explained using a simplified model described below. The two measurement configurations which are relevant to this study are depicted in figure 3.7. The case where the magnetization is parallel to both sample plane and plane of incidence is referred to as 'longitudinal' geometry. Here the sample is illuminated

with p-polarized light (i.e., the electric field \vec{E}_p oscillates within the plane of incidence or the x-y plane) at an angle of θ_i with respect to the surface normal. \vec{E}_p causes electrons in the sample to oscillate in the x-y plane. As this motion takes place within the local magnetic field of the ferromagnet (which is along x), the ensuing Lorentz force leads to additional oscillation along the z-axis [49]. Consequently, the radiation emitted by these accelerating charges carries two electric field components: \vec{E}_p caused by electron oscillation driven by the incoming light and \vec{E}_s , an out-of-phase orthogonal component resulting from the Lorentz force induced oscillation. Thus, the reflected light is elliptically polarized with the major axis of its polarization ellipse being oriented at an angle of Θ_K (Kerr rotation) with respect to the plane of incidence. Opposite domains produce Kerr rotations of opposite signs, thereby generating magnetic contrast. In case of transverse geometry, the magnetization lies within the sample plane but is perpendicular to the plane of incidence. The incident p-polarized light retains its polarization state upon reflection at the ferromagnetic surface but with an altered amplitude. The outgoing intensity is different for $+\vec{M}$ and $-\vec{M}$ which helps distinguish 180° domains.

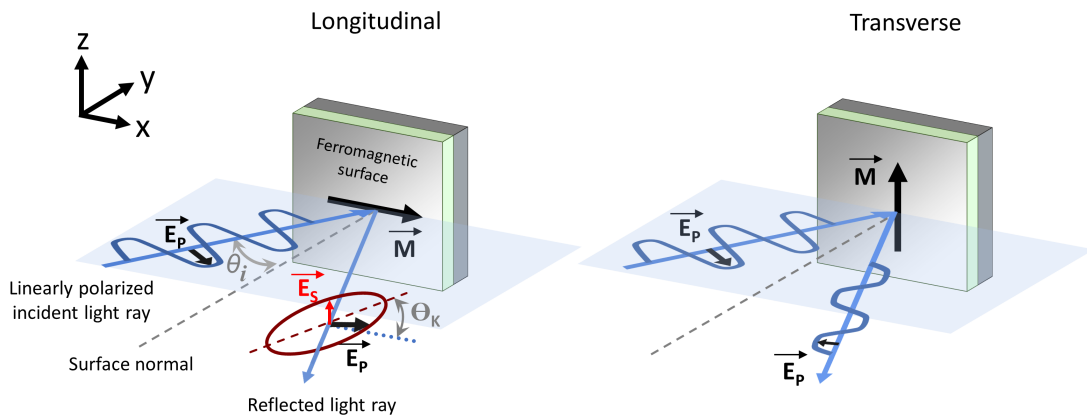


Figure 3.7. Longitudinal and transverse MOKE geometries. The plane of incidence (shown here in blue) is defined by the incident and reflected beams.

In the Kerr microscope employed for this study, off-centred light emitting diodes (LEDs) arranged in a cross pattern serve as the source of primary light, enabling users to choose between the measurement geometries explained above. The incident light has a wavelength of 500 nm which limits the lateral spatial resolution of the microscope to ≈ 300 nm. A polarizer is placed along the primary beam path to convert unpolarized light from the LEDs into p-polarized light. The light reflected from the

sample is passed through an analyzer (i.e., a second polarizer) to infer the magnetization of the illuminated region. Thus, the outgoing intensity depends upon the polarization state of the reflected light and aids in resolving ferromagnetic domains. The spatially resolved images can be recorded via a CCD camera. Additionally, this apparatus allows for in-situ application of in-plane magnetic fields of up to 350 mT using a rotatable electromagnet.

3.6 Dichroism in magnetic materials

Magnetic dichroism refers to the dependence of light absorption by a magnetic material on the relative orientation of its magnetic moments and the polarization (or electric field) of incident light. It is often combined with the imaging technique of PEEM to map out the domain structures of FMs, ferrimagnets and AFMs with high spatial resolution. The various dichroism effects which were used in this study to characterize the magnetic materials involved are explained in the following subsections.

3.6.1 X-ray magnetic circular dichroism (XMCD)

XMCD relies on the difference in the absorption of right- and left circularly polarized (μ^+ and μ^-) light by ferro- and ferrimagnetic materials to probe their domain structure. Within the framework of the one-electron model the mechanism behind XMCD observed at the $L_{2,3}$ -edges of magnetic elements (Fe, Co, Ni etc.) can be decomposed into two steps [51]. In the first step, circularly polarized soft X-rays corresponding to the binding energies of non-degenerate 2p core levels tend to predominantly excite \uparrow or \downarrow spins (depending on X-ray helicity)[‡] to 3d electronic states near the Fermi edge (figure 3.8). Thus, the 2p core levels can be considered to be a source of spin-polarized electrons. The second step involves the spin asymmetry of the 3d band which favours the entry of one type of spin more than the other, thereby functioning as a partial spin-filter. As photon absorption by a 2p electron is dependant on its successful transition to the 3d band, μ^+ and μ^- X-rays elicit dissimilar absorption behaviours from any uniformly magnetized region on the sample (for instance, a FM domain). At any given photon energy

[‡]This phenomenon is known as the Fano effect and is a consequence of spin-orbit coupling [52].

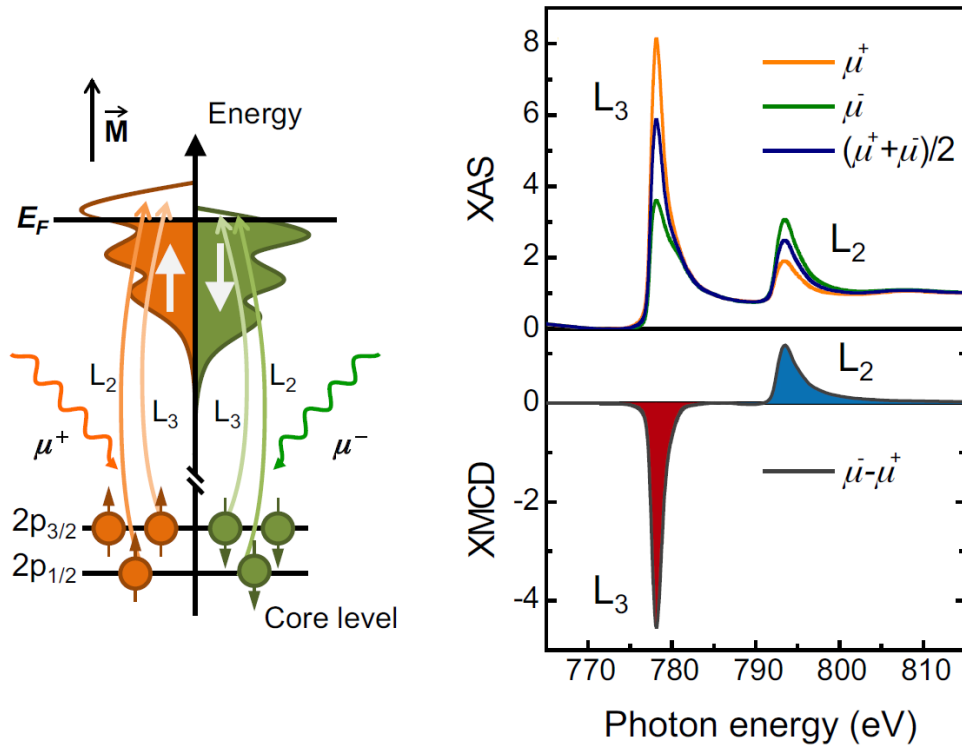


Figure 3.8. Principle of XMCD. A monodomain FM is considered here with magnetization \vec{M} as shown. The helicity vector of the incident photons is assumed to be collinear with \vec{M} (maximum XMCD). For the L_3 transition, μ^+ X-rays have a greater chance (0.625) of exciting \uparrow spin electrons compared to \downarrow spin (0.375) while the reverse is true for μ^- X-rays. The sample is first illuminated with μ^+ X-rays and the corresponding absorption spectrum (XAS) is shown on the right. At photon energy corresponding to the L_3 absorption edge both \uparrow and \downarrow spins can be easily excited to the 3d band as the two spin channels offer a sufficient number of states near the Fermi edge E_F . Subsequently, an XAS spectrum is also obtained using μ^- X-rays which tend to excite more \downarrow spins as explained above. However, a lack of enough 3d \downarrow states near E_F impedes this transition, thereby lowering the overall X-ray absorption. In case of the L_2 -edge, μ^+ X-rays have a probability of 0.25 and 0.75 for exciting \uparrow and \downarrow spins respectively (once again, the opposite is true for μ^- X-rays). Thus, XMCD is also observed at the L_2 -edge but with an opposite sign [50]. Figure modified from [50].

the dichroism is calculated as :

$$\text{XMCD} = \frac{I_{\mu^-} - I_{\mu^+}}{I_{\mu^-} + I_{\mu^+}} \quad (3.4)$$

Where I_{μ^+} and I_{μ^-} represent the X-ray absorption intensities with μ^+ and μ^- polarizations respectively. In this way opposite magnetic domains can be distinguished by their XMCD values (contrast). However, the XMCD magnitude shows a cosine dependance on the angle (θ) between the X-ray incidence vector (collinear with photon spin) and the magnetic moments. Therefore, it is found to be maximum at parallel and anti-parallel alignments ($\theta = 0^\circ$ and 180° respectively). At perpendicular incidence (i.e., $\theta = 90^\circ$) both μ^+ and μ^- X-rays are absorbed equally, leading to zero XMCD.

3.6.2 X-ray magnetic linear dichroism (XMLD)

XMLD utilizes the difference in the absorption of X-rays which are polarized parallel and perpendicular to the magnetic easy axis of a given material. It has become an indispensable tool in the study of magnetism, especially since the advent of antiferromagnetic spintronics.

The distribution of charge in the atoms of non-magnetic crystals shares the symmetry of the crystal lattice. Owing to spin-orbit coupling, the superposition of a magnetic order on the crystal structure breaks this symmetry by deforming the charge distribution along the axis of magnetic moments [53]. This deformation is probed by the incident X-rays as it makes their absorption dependant on polarization, thereby revealing the orientation of magnetic axes. At a given photon energy the XMLD is calculated as :

$$\text{XMLD} = \frac{I_{E\parallel} - I_{E\perp}}{I_{E\parallel} + I_{E\perp}} \quad (3.5)$$

Where $I_{E\parallel}$ and $I_{E\perp}$ represent the X-ray absorption intensities with the electric field \parallel and \perp to a chosen magnetic axis respectively. The magnitude of XMLD scales with cosine² of the angle made by the X-ray electric field vector with the magnetic moments [54]. Therefore, maximum XMLD contrast is obtained in case of mutually orthogonal (90°) domains of ferro-, ferri- and antiferromagnets unlike XMCD where the maximum contrast is found between opposite (180°) domains in materials which carry a net magnetic moment.

3.7 Photoemission electron microscopy (PEEM)

To verify the imprinting of antiferromagnetic Mn_2Au domains on the Py overlayer one needs to visualize both magnetic layers at the same spot via synchrotron based microscopy. A study of this nature was previously reported by Nolting et al. [55] in case of LaFeO_3/Co and by Scholl et al. [56] in NiO/Co . A thin layer of Co deposited at room temperature over antiferromagnetic LaFeO_3 was found to mimic the underlying domain pattern due to 'microscopic exchange bias' at the interface. This was observed using PEEM combined with XMCD and XMLD for the ferromagnetic and antiferromagnetic layers respectively. Similar to an SEM, PEEM relies on the variation in secondary electron emission across a given sample to resolve its topographical features. However, this technique uses X-rays from a synchrotron light source to probe a material (hence the name photoemission) unlike an SEM which uses electrons. A basic PEEM setup is illustrated in figure 3.9.

A similar investigation was carried out as a part of this work on $\text{Mn}_2\text{Au}/\text{Py}$ bilayers at the MAXPEEM beamline - MAX IV laboratory in Lund, Sweden. The beamline has an X-ray incidence angle of 90° with respect to the sample surface and has a lateral spatial resolution of ≈ 30 nm. In this scenario, XMCD is nullified as explained earlier in section 3.6.1. Therefore, XMLD-PEEM was used to visualize the ferromagnetic domains of Py as well as the antiferromagnetic domains of the underlying Mn_2Au .

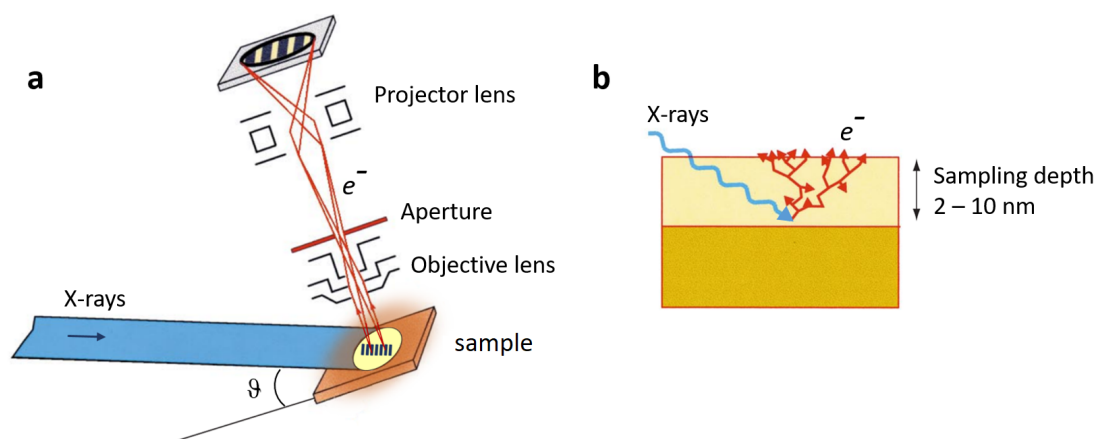


Figure 3.9. a. Experimental setup of PEEM. Both linearly- and circularly polarized X-rays from a synchrotron light source can be used as primary radiation depending on the type of measurement desired. θ is the X-ray incidence angle with respect to the sample plane. The electron optics shown here is responsible for directing the photoelectrons released from the sample on to a phosphor screen which is read by a CCD camera. The contrast observed in the image contains both morphological and magnetic information. b. The information- or sampling depth of this technique is defined by the maximum distance beneath the surface of the sample from which photoelectrons can escape. It is material dependant (typically, $\sim 2 - 10$ nm). Figure modified from [53].

4 Results and discussion

4.1 Characterization of epitaxial Mn_2Au (001) thin films

The results of various analysis procedures that were employed to arrive at optimal growth conditions for Mn_2Au (001) (section 3.1) are elaborated upon here. The characterization begins with in-situ RHEED (performed after cooling the deposited thin films to room temperature) to draw information pertaining to surface crystallinity and topography. Both MBE and sputtered samples reveal sharp diffraction spots arranged on semi-circles together with the presence of Kikuchi lines (figure 4.1). These observations indicate a highly crystalline and smooth surface with a low concentration of crystallographic defects and also imply an improvement over the Mn_2Au (001) films previously reported by this group [37]. The surface features were explored further using X-ray reflectometry (XRR) and scanning tunnelling microscopy (STM) measurements, the results of which are presented later in this section.

The XRD specular $\Theta/2\Theta$ scans shown in figure 4.2 reveal the presence of (001)-oriented Mn_2Au in both samples. A small fraction of the sputtered film is in a Mn-Au cubic phase also growing in the (001) orientation. This undesired phase which was earlier assumed to be Mn_2Au (101) [37] is now minimized as a result of the optimization of deposition temperature and the addition of post-deposition annealing (described in section 3.1). Both MBE and sputtered samples share the same quality of bulk crystalline order which can be inferred from the rocking curve width of the (002) peak (ω -scan). A mosaicity of 0.5° is observed.

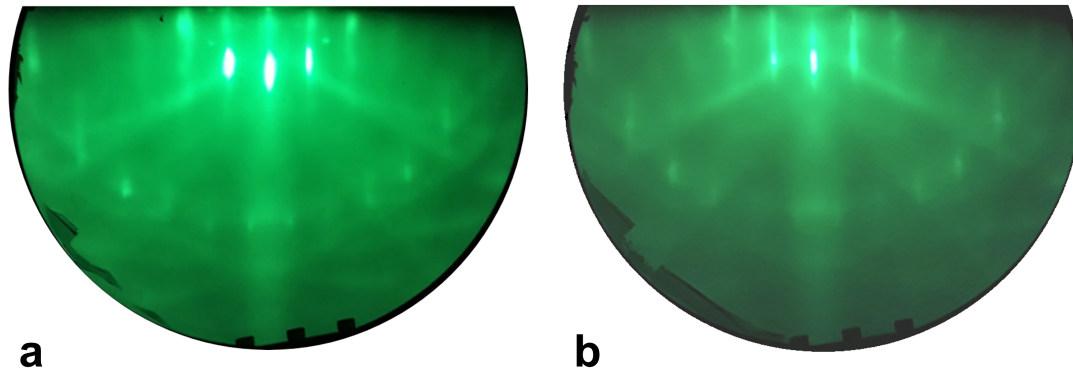


Figure 4.1. RHEED patterns of Al_2O_3 ($1\bar{1}02$)/13 nm Ta (001)/45 nm Mn_2Au (001). a. MBE sample. b. Sputtered sample. The diffraction spots are organized on semicircles, indicating a relatively smooth morphology (rather than a 3-dimensional island-like topography) as explained earlier in figure 3.3.b. The Kikuchi lines observed in both cases point towards a well defined crystallographic order at the surface.

Figure 4.3 shows the in-plane order of a MBE grown Ta (001)/ Mn_2Au (001) sample which was determined with off-specular XRD ϕ -scans of Mn_2Au (101) and Ta (220) planes. In each case, the scan reveals four peaks occurring at regular intervals of 90° within the full range of ϕ ($0^\circ - 360^\circ$), thereby confirming the fourfold rotational symmetry of both Mn_2Au (001) and Ta (001). The coinciding peaks of both species indicate a parallel orientation of Mn_2Au [100] and Ta [100] which is expected based on the lattice match between the two crystals. The same investigation was also carried out on sputtered samples and it found very similar data, leading to the conclusion that the degree of in-plane crystallographic ordering is very high in both sample types.

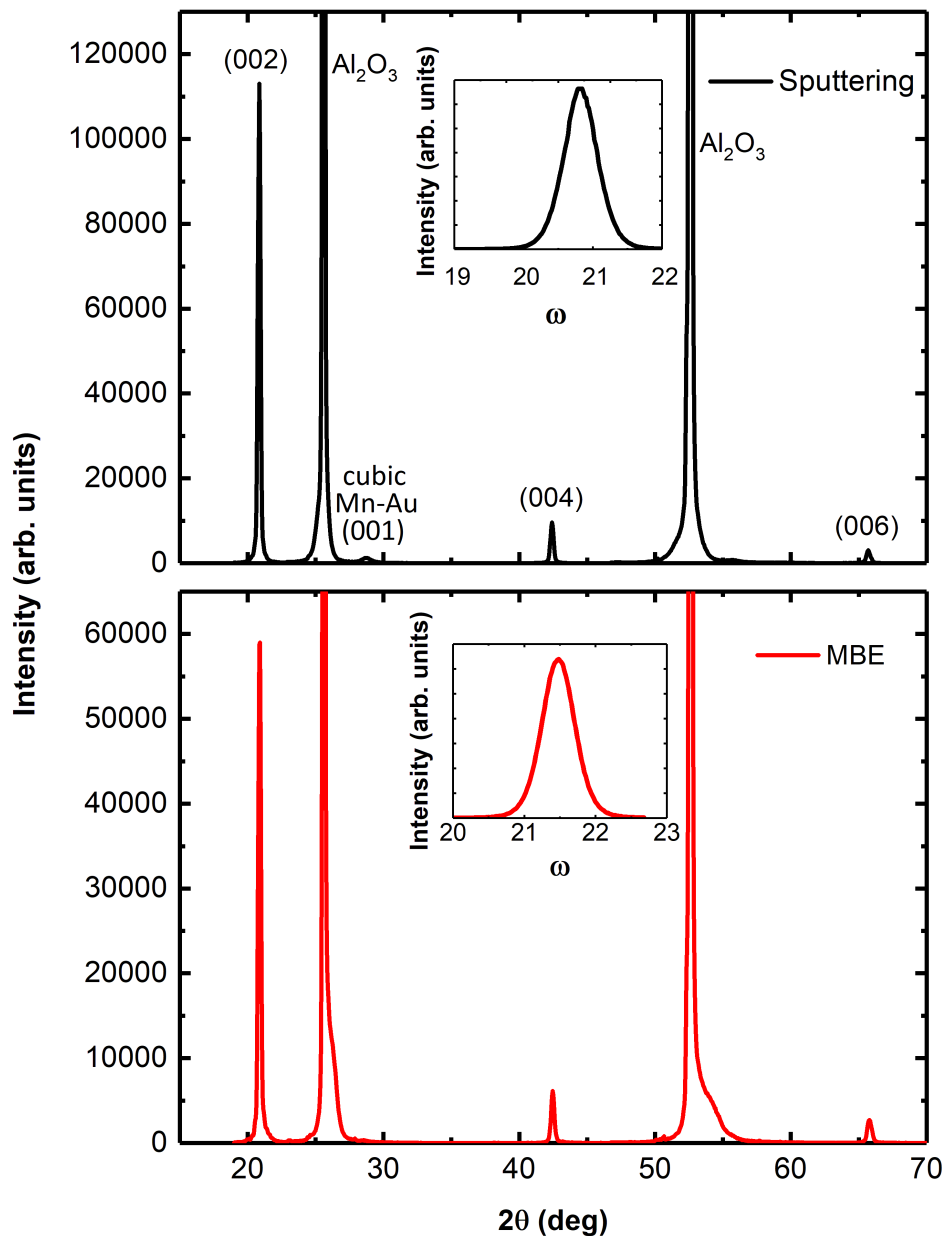


Figure 4.2. $\Theta/2\Theta$ XRD specular scans of Al_2O_3 ($1\bar{1}02$)/13 nm Ta (001)/45 nm Mn_2Au (001) demonstrating the (001)-orientation of sputtered (upper panel) and MBE-grown (lower panel) samples. The rocking curves of the (002) peak of Mn_2Au are shown in insets. The Ta (002) peak from the buffer occurs at $\approx 55.6^\circ$ but has a very low intensity due to the small thickness of this layer, and is therefore not visible on this scale.

The co-deposition of Mn and Au from separate sources with independent rate control in MBE allows for the tuning of sample composition as desired. However, it also poses a challenge to the reproducible growth of Mn_2Au thin films with an accurate composition. Furthermore, the

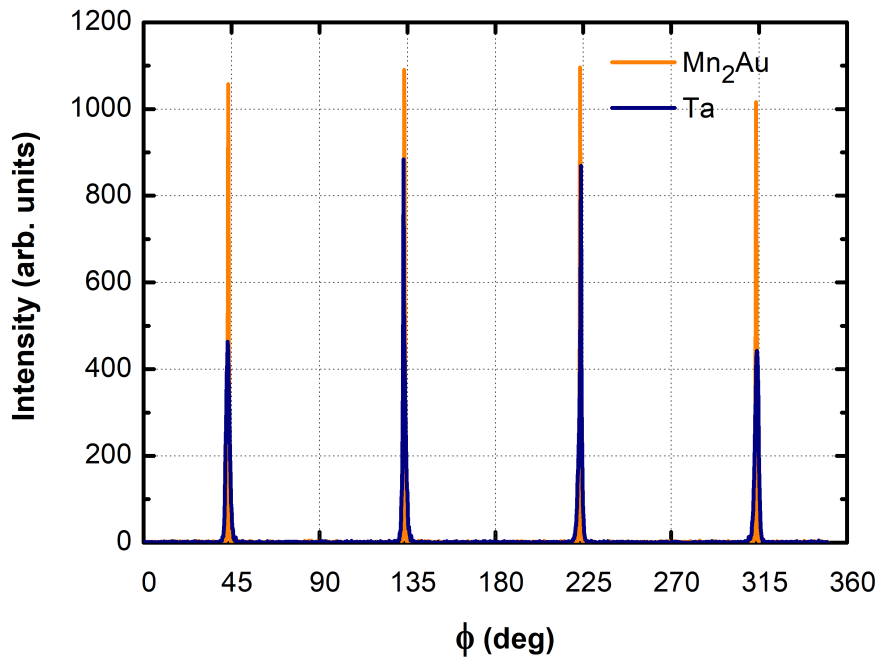


Figure 4.3. XRD ϕ -scans of off-specular Mn_2Au (101) and Ta (220) peaks of a Al_2O_3 ($1\bar{1}02$)/13 nm Ta (001)/45 nm Mn_2Au (001) MBE sample. One edge of the substrate is parallel to the scattering plane at $\phi = 0^\circ$. The first peaks occur at $\phi = 45^\circ$, implying a parallel alignment of Ta [110] and Mn_2Au [110] with respect to the substrate edge (45° rotation of the Mn_2Au basal plane as explained in figure 3.1).

quantification algorithms used by many standard stoichiometry analysis techniques such as X-ray fluorescence (XRF) and energy dispersive X-ray spectroscopy (EDX) assume a semi-infinite sample, rendering them suitable only for bulk specimens. Therefore, the accurate analysis of thin film stoichiometry often demands special methods. After a careful adjustment of the deposition rates, MBE-grown Mn_2Au thin films were obtained with an ideal composition of 66.6 ± 1.2 at.% Mn and 33.4 ± 1.7 at.% Au as determined by inductively coupled plasma optical emission spectroscopy (ICP-OES). The sputtered samples were found to have a composition of 66.1 ± 1.2 at.% Mn and 33.9 ± 1.7 at.% Au. This was further verified using Rutherford backscattering spectrometry (RBS), which estimated the stoichiometry values to be within the error margin mentioned above. Interestingly, both the analysis techniques revealed that for annealing temperatures higher than 450°C Mn begins to desorb from the film, changing both its stoichiometry and crystallographic phase. For instance, a sample annealed at 500°C was found to be polycrystalline (containing a large fraction of the Mn-Au cubic impurity) with an overall composition of 56.6% Mn and 43.3% Au. Additionally, RBS revealed that this sample contained an 8 nm thick Mn–Au–Ta alloy layer

between the buffer and Mn_2Au layers due to thermally activated diffusion of Ta atoms into the overlying film.

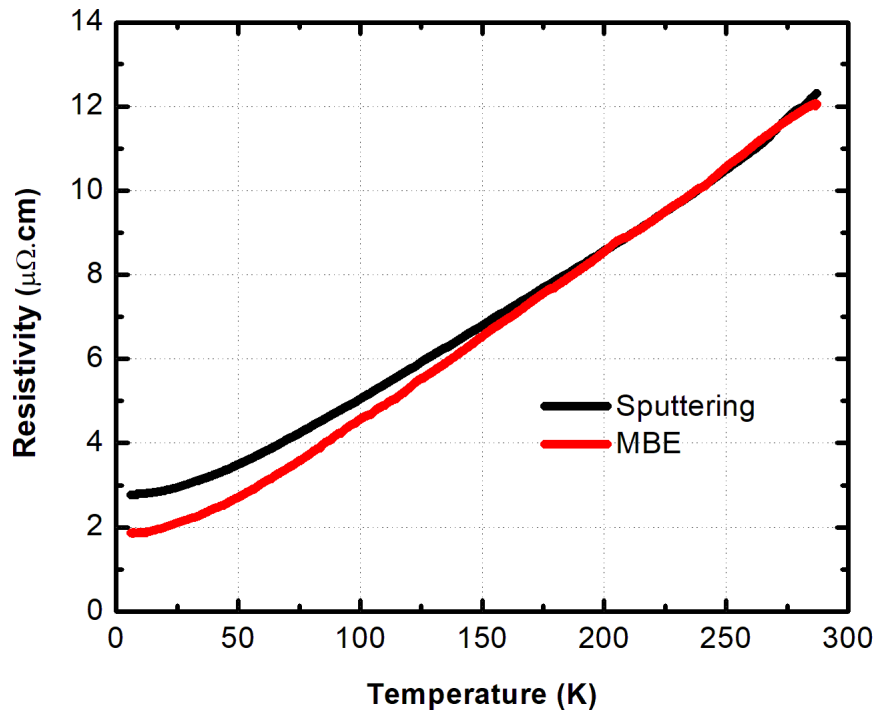


Figure 4.4. Resistivity vs. temperature measurements of 45 nm Mn_2Au (001) films. The buffer layer contribution was eliminated by measuring the resistance (vs. temperature) of an Al_2O_3 ($1\bar{1}02$)/13 nm Ta (001) sample and subtracting it from the resistance of Al_2O_3 ($1\bar{1}02$)/13 nm Ta (001)/45 nm Mn_2Au (001) using a parallel circuit model. Compared to the sputtered sample, reduced residual resistivity of the MBE thin film indicates a lower degree of disorder achieved by MBE deposition.

Although X-ray diffraction probes the crystallographic order of the samples, its sensitivity for low degrees of disorder, which nevertheless influences the transport properties, is limited. A figure of merit for the concentration of impurities, which results in the scattering of charge carriers in metals, is the residual resistance ratio (RRR) = $\text{Resistance}_{300\text{K}}/\text{Resistance}_{4\text{K}}$. Thus, temperature dependent sheet resistivity measurements were performed on both MBE deposited and sputtered Mn_2Au films (grown under optimized conditions) using the van der Pauw method (Fig. 4.4). Though the resistivity of both films is the same at 300 K, the MBE film has a lower resistivity at 4 K (a temperature where phonon scattering is suppressed), implying a lower level of intrinsic disorder. The MBE film shows $\text{RRR} \approx 6.8$, while the value for the sputtered film is $\text{RRR} \approx 4.6$. These values represent a significant improvement in quality over that of the previously reported films, which showed a residual

resistivity of $7 \mu\Omega\cdot\text{cm}$ and $\text{RRR} \approx 3$ [37].

Furthermore, the high degree of smoothness possessed by an MBE-grown film is evident from the presence of prominent Kiessig fringes corresponding to its thickness of 45 nm in its XRR scan (figure 4.5). The sputtered sample mainly shows oscillations corresponding to the 13 nm Ta buffer layer. Though faint fringes corresponding to the Mn_2Au layer are also present at lower values of the scattering angle, they fade away rather quickly with increasing 2Θ , implying a lower surface quality compared to MBE films.

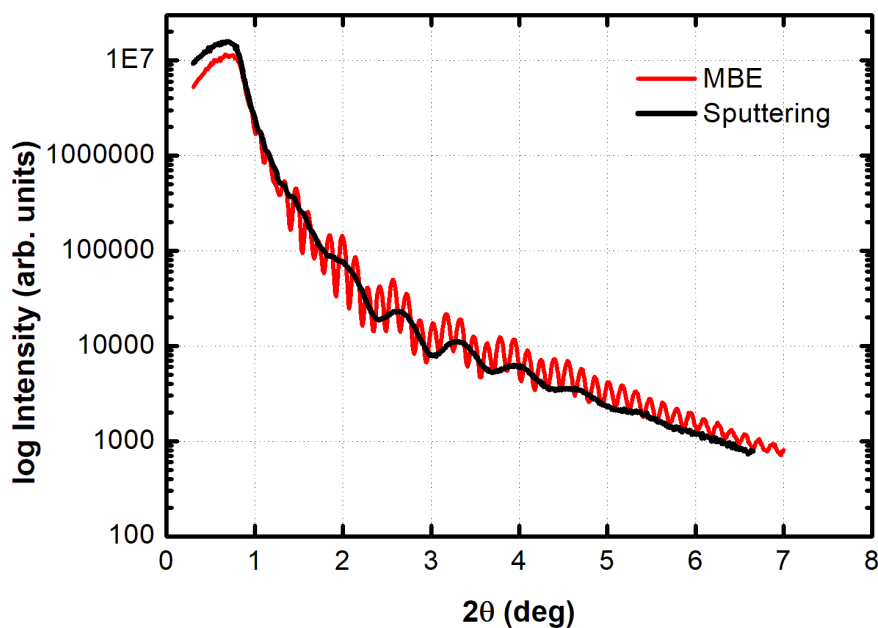


Figure 4.5. Comparison of the XRR scans of Al_2O_3 ($1\bar{1}02$)/13 nm Ta (001)/45 nm Mn_2Au (001) samples grown via MBE and RF magnetron sputtering techniques. The MBE grown Mn_2Au film shows pronounced oscillations till $2\Theta = 7^\circ$ owing to its relatively smoother morphology.

Although both these techniques yield epitaxial Mn_2Au (001) films of a high quality, magnetron sputtering was used for all subsequent experiments due to its relatively high through-put and ease of operation. Scanning tunnelling microscopy was carried out on a sputtered 40 nm Mn_2Au (001) thin film to study its surface features in greater detail. The sample was prepared using the standard growth procedure described in section 3.1.1 and was subsequently moved to the STM analysis chamber under UHV conditions in a transport box (a.k.a vacuum suitcase) as the measurement was performed ex-situ. Though the delocalization of electrons over a metallic surface makes it difficult to achieve atomic resolution, the technique was able to reveal the

presence of atomically flat terraces spanning a few tens of nm (figure 4.6). The terraces are separated by steps whose height is always an integer multiple of half a unit cell. As Mn_2Au has a layered structure with each type of atomic plane (i.e., Au, Mn_A and Mn_B) also repeating at half unit cell intervals along [001] (see section 2.2), these steps should cause the film to terminate in the same atomic plane across the entire surface.

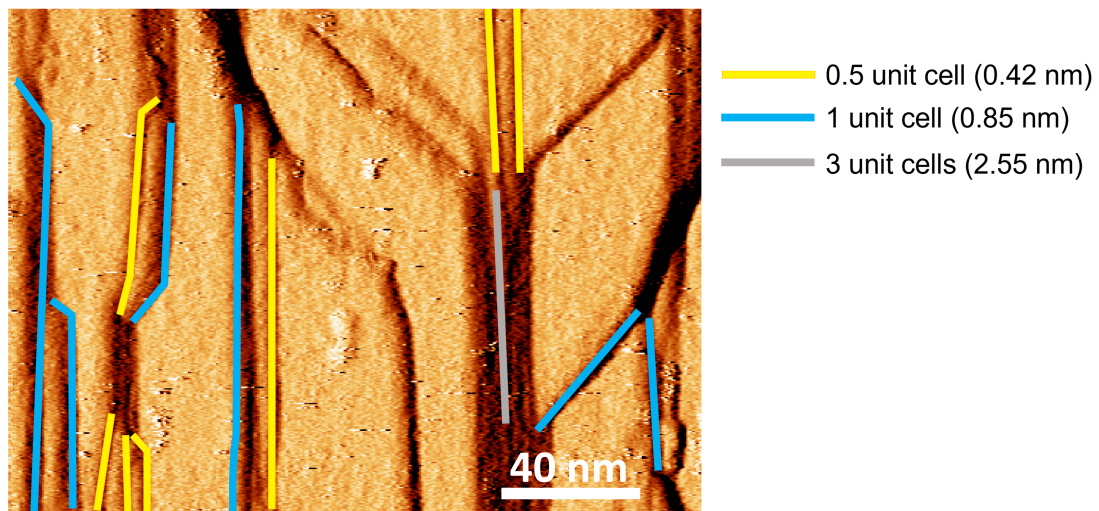


Figure 4.6. Topography of a sputtered Al_2O_3 ($1\bar{1}02$)/13 nm Ta (001)/40 nm Mn_2Au (001) sample mapped via STM. The surface of Mn_2Au is seen to be composed of smooth terraces and steps whose height is half an integer multiple of the c -axis parameter of Mn_2Au ($c = 0.85$ nm). Obtained with the help of Dr. T. Mashoff and Prof. H.-J. Elmers from the Institut für Physik, Johannes Gutenberg-Universität Mainz.

High resolution transmission electron microscopy of the cross section of a Al_2O_3 ($1\bar{1}02$)/13 nm Ta (001)/40 nm Mn_2Au (001)/10 nm Py/2 nm Si_3N_4 sample helped garner information regarding this topmost lattice plane as well as other significant features which cannot be identified by XRD. The atomic resolution provided by TEM (figure 4.7.a and b) reveals that the Mn_2Au (001) thin film terminates in a Au layer. The c -axis of Mn_2Au is tilted with respect to the substrate normal by $\approx 2.2^\circ$. This is a consequence of the low rotational symmetry of Al_2O_3 ($1\bar{1}02$) and has also been observed in case of other epitaxial thin films such as Nb (001) [57] and ZrN (001)^{§§} [58] grown over this substrate at elevated temperatures. The interfaces between various layers of the stack are observed to be sharp without signs of interdiffusion. Additionally, low energy electron diffraction (LEED) performed as a part of this analysis clearly distinguishes the Mn-Au impurity as a separate crystallographic and

^{§§}Though Tanabe *et al.* do not explicitly mention it, the misalignment is evident from the absence of substrate peaks in the $\Theta/2\Theta$ XRD scan shown in figure 1 of this publication.

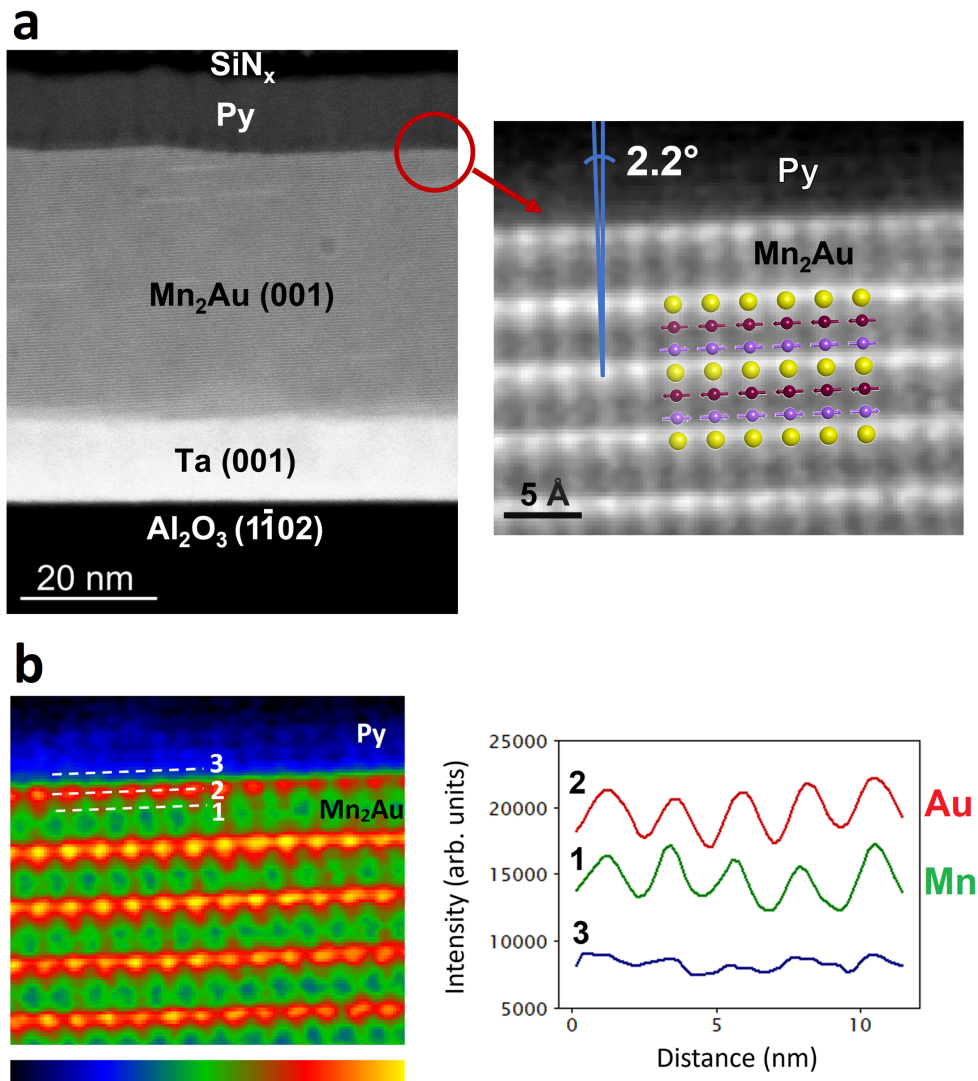


Figure 4.7. a. High resolution TEM images of the cross section of a Al_2O_3 ($1\bar{1}02$)/40 nm Mn_2Au (001)/10 nm Py/2 nm Si_3N_4 (cap) sample (viewed along Mn_2Au [110]). A close-up image of the Mn_2Au (001)/Py interface is shown on the right. b. Colour coded intensity map of the Mn_2Au (001)/Py interface in (a). Profiles 1 and 2 show the regular arrangement of Au and Mn atoms respectively in the topmost lattice planes. Profile 3 is extracted from the region above the last Au plane (where a Mn plane can be expected based on the crystal structure of Mn_2Au) and no such regular variation in intensity is seen, confirming a Au termination of the Mn_2Au (001) thin film. Obtained with the help of Dr. T. Denneulin and Dr. A. Kovacs from the Ernst Ruska centre for microscopy and spectroscopy with electrons, Forschungszentrum Jülich, Germany.

stoichiometric phase (figure 4.8). TEM also sheds light on the distribution of this impurity within the Mn_2Au thin film. It is predominantly scattered across the Ta/ Mn_2Au interface in a non-homogeneous fashion and is entirely absent at the surface of Mn_2Au (001) which is of primary interest to the study of exchange coupled AFM/FM bilayers.

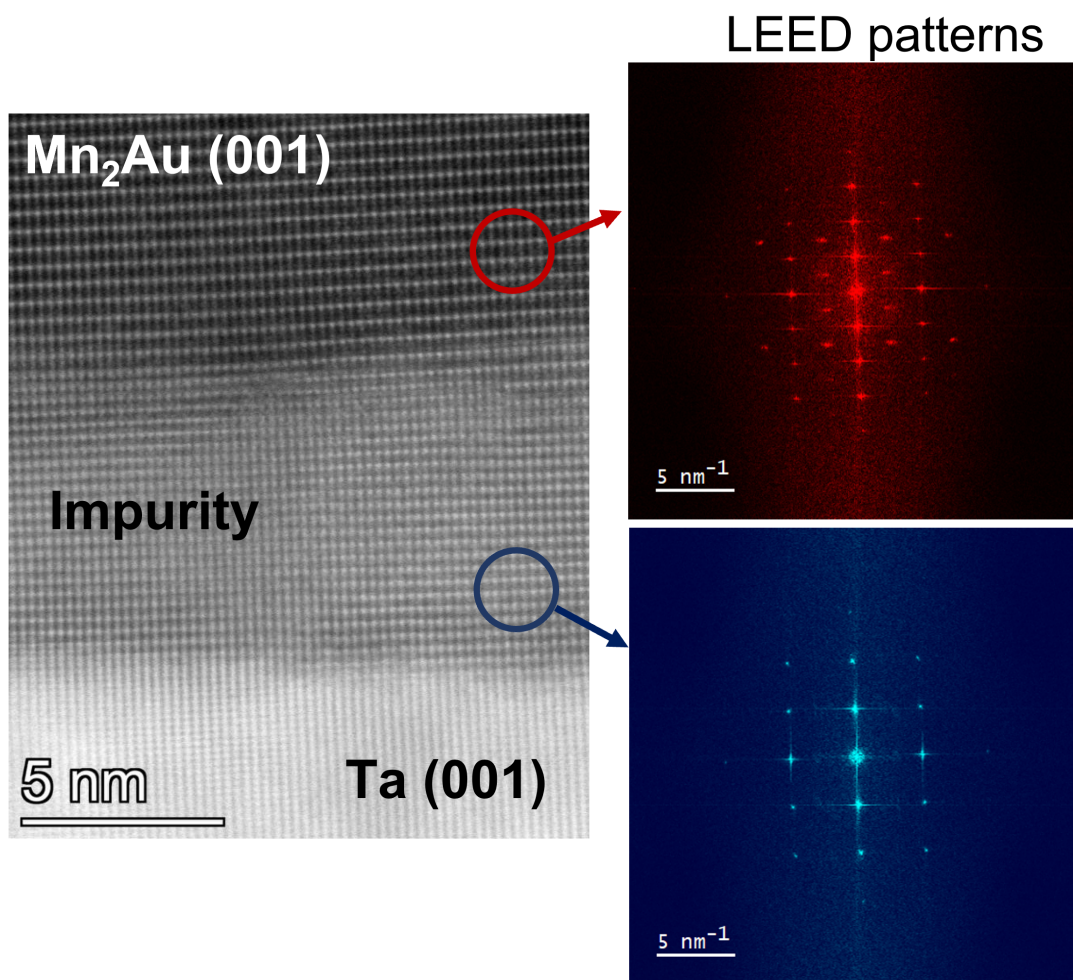


Figure 4.8. High resolution TEM of the cross section of an optimized Mn_2Au thin film prepared by RF magnetron sputtering. The image was acquired from a small region of the Ta/ Mn_2Au interface containing the cubic Mn-Au (001) impurity. LEED patterns corresponding to the two phases are shown on the right. In the desired Mn_2Au (001) phase, the spacing between any two successive Au planes is found to be $\approx 4.3 \text{ \AA}$ (half unit cell height) as expected. The cubic impurity phase has a vertical lattice constant of $\approx 3.2 \text{ \AA}$ and appears relatively brighter due to its different stoichiometry. Obtained with the help of Dr. T. Denneulin and Dr. A. Kovacs from the Ernst Ruska centre for microscopy and spectroscopy with electrons, Forschungszentrum Jülich, Germany.

The canting of Mn_2Au [001] is unidirectional (i.e., present only along one side of the substrate) as illustrated in figure 4.9. It can be quantified via XRD

as the difference in rocking curve maxima ($\Delta\omega$) of the (002) and (1 $\bar{1}$ 02) peaks of Mn₂Au and Al₂O₃ respectively (when measured with the tilted side parallel to the scattering plane).

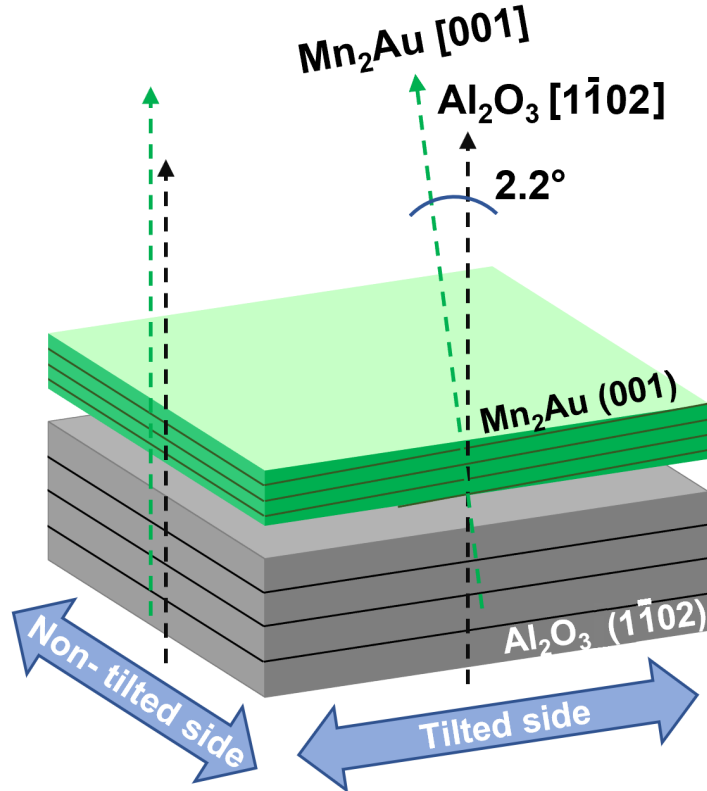


Figure 4.9. Monodirectional canting of Mn₂Au [001] induced by the low symmetry of the Al₂O₃ (1 $\bar{1}$ 02) plane. The c-axes of both film and substrate are parallel on one side of the sample while they form an angle of 2.2° on an orthogonal side.

4.2 Magnetic microscopy of Mn₂Au/FM bilayers

4.2.1 SEMPA based imaging of FM overlayers

Initially, a 4 nm overlayer of Fe was chosen for the preparation of exchange coupled Mn₂Au/FM bilayers based on earlier experiments by Jourdan et al. [37]. The Al₂O₃ (1 $\bar{1}$ 02)/13 nm Ta (001)/40 nm Mn₂Au (001)/4 nm Fe stack was capped with a 2.5 nm thick layer of Al as magnetic imaging was carried out ex-situ. As SEMPA is a surface sensitive technique, the Al cap layer was milled away using energetic Ar⁺ ions at a pressure of 7.5 × 10⁻⁶ mbar together with an acceleration voltage of 1000 V for 40-50 minutes to expose

the underlying Fe prior to imaging. The process was carried out inside a UHV sample preparation chamber attached to the SEMPA. The domain pattern of Fe was found to be strongly dependant on the milling time. The results are shown in figure 4.10.

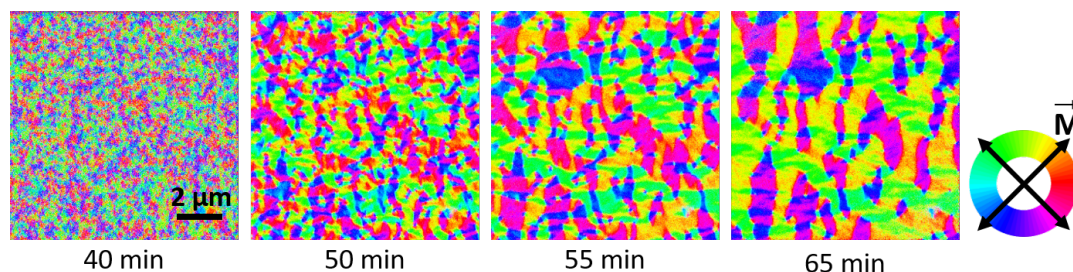


Figure 4.10. SEMPA imaging of Fe domains in a Al_2O_3 ($1\bar{1}02$)/40 nm Mn_2Au (001)/4 nm Fe/2.5 nm Al (cap) stack. The sample was de-capped via Ar^+ etching. The images were acquired from the same $10 \times 10 \mu m^2$ area of the sample after various milling periods [59]. The colours represent domain orientations and can be interpreted using the colour wheel shown on the right. The domain pattern is found to change drastically with milling time (In this particular case, the domains are seen to enlarge with increasing milling time but the behaviour was found to vary from sample to sample).

During the course of this study, it was discovered that the domains of ferromagnetic thin films can be visualized directly through a thin protective cap layer, albeit with longer accumulation time (compared to uncapped samples). All subsequent SEMPA imaging was carried out through an Al or a Si_3N_4 cap. Si_3N_4 is well suited to act as a protective overlayer, particularly in microscopy experiments due to its low density, uniform growth at small thicknesses (figure 4.7.a), chemical stability and good adhesion. As Si is already passivated with N, it is less likely to interact with adjacent layers (evident from the sharp Py/ Si_3N_4 interface seen in figure 4.7.a) unlike Al, which has a strong tendency to form intermetallic alloys with other metals at interfaces. Si_3N_4 being a low density insulator was also found to be sufficiently electron transparent for surface sensitive ex-situ angle-resolved photoemission spectroscopy (ARPES) measurements performed by this group on Mn_2Au [60]. Mn_2Au /FM bilayer samples capped with Si_3N_4 were found to survive for several months under ambient conditions with no measurable loss of magnetic moment.

The domain pattern of Fe in a pristine Mn_2Au /Fe/Al cap sample (figure 4.11) was found to vary significantly from that in a sample which was subjected to milling. This difference is attributable to structural damage caused by the impinging Ar^+ ions during the de-capping process. The

average domain size is $\sim 1 \mu\text{m}$ and the ferromagnetic moments of Fe are coupled to the antiferromagnetic moments of Mn_2Au with a mutual angle of 45° . The reason behind this bi-quadratic exchange coupling is most likely the epitaxial growth of Fe (100) on Mn_2Au (001) [61]. Thus, the observed spin orientation in Fe is a compromise between its magnetocrystalline anisotropy and its exchange coupling to the adjacent AFM.

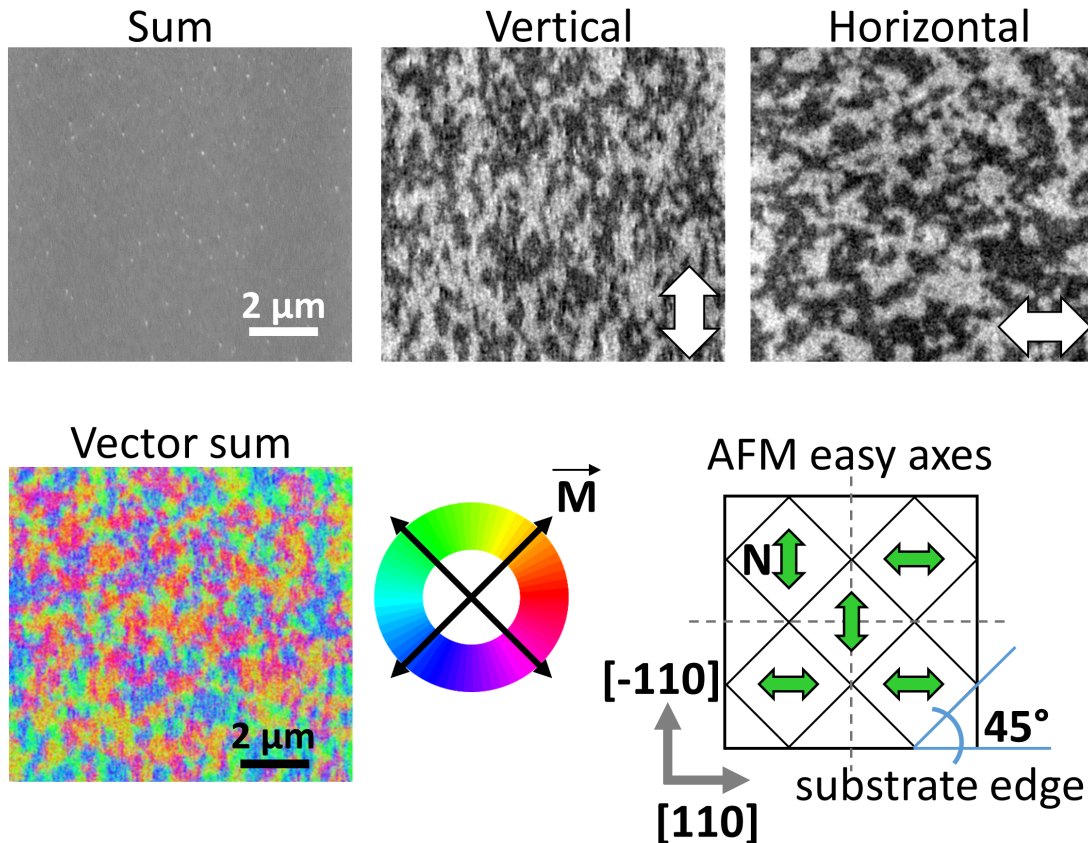


Figure 4.11. SEMPA imaging of Al_2O_3 ($1\bar{1}02$)/13 nm Ta (001)/40 nm Mn_2Au (001)/4 nm Fe/2.5 nm Al. The top panel comprises of raw data generated by SEMPA. The total number of electrons received from each spot by all four channeltrons combined is used to construct the 'sum' or topography image. The 'vertical' and 'horizontal' asymmetry images represent two orthogonal in-plane magnetization components as resolved by the SPLEED crystal. As the sum image shows a smooth morphology, the contrast seen in the asymmetry images is certainly of magnetic origin. The colour coded image contained within the bottom panel represents the vector sum of these two magnetization components. The FM moments \vec{M} make a 45° angle with respect to the underlying AFM moments N . The image was acquired over an accumulation time of ≈ 30 min.

As NSOT is expected to rotate the Néel order by 90° , this bi-quadratic coupling may lead to ambiguity in the intended visualization of current-induced AFM switching via the FM layer. To circumvent this issue,

Fe was replaced by Permalloy which is well known to be an extremely soft ferromagnet with virtually zero magnetocrystalline anisotropy, and is therefore ideal for experiments of this nature. However, the smaller spin polarization of Py yields a relatively low signal to noise ratio, demanding a significantly higher accumulation time ($\approx 15 \times$ time needed for Fe) to generate SEMPA images with good contrast. The horizontal and vertical components of the domain orientations of a Py overlayer exchange coupled to Mn_2Au (001) are presented in figure 4.12. Domains with an average size of $\sim 1 \mu m$ are observed, similar to the case of Mn_2Au /Fe (figure 4.11). The FM moments are also seen to lay parallel to the substrate edges similar to the AFM moments below, indicating a mutually collinear exchange coupling between the two layers. Four distinct magnetic directions are found corresponding to four possible orientations of the AFM sublattices closest to the AFM/FM interface (due to the layered structure of Mn_2Au combined with its two easy axes). The unidirectional tilt of Mn_2Au [001] lifts the degeneracy between its otherwise equivalent AFM easy axes. This causes an asymmetric distribution of domains with $\approx 60\%$ of them being aligned parallel to the sample side along which the c-axis is tilted (verified using images acquired from multiple locations in several samples).

The observed domain size was also found to be dependant on the AFM film thickness. Lowering the thickness of Mn_2Au to 22 nm reduces the average domain size to ~ 300 nm as shown in figure 4.13. This could be related to an increased mosaicity of 0.86° found in this sample compared to 0.5° for a 40 nm film. During this study, it was also established that the mosaicity of Mn_2Au (001) thin films varies as a function of thickness, with better crystallinity (or lower mosaicity) being obtained at larger thicknesses.

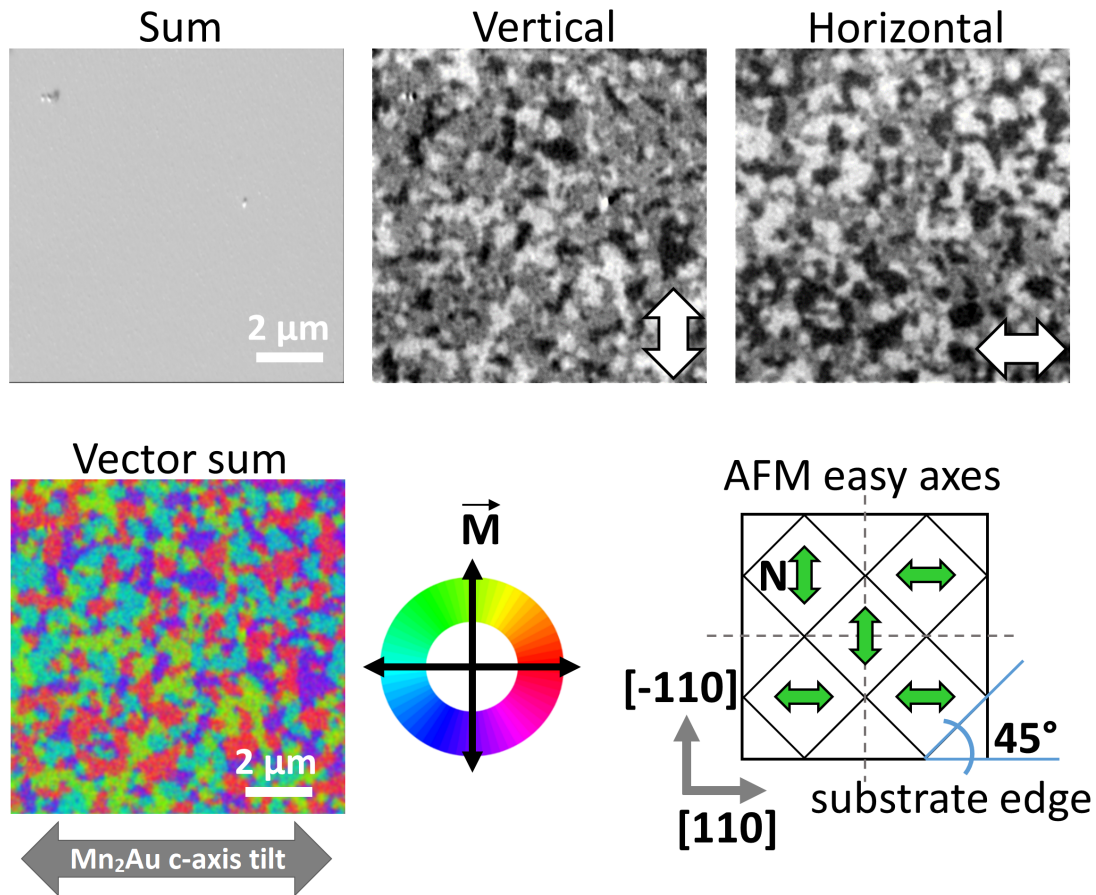


Figure 4.12. SEMPEA imaging of Al_2O_3 ($1\bar{1}02$)/13 nm Ta (001)/40 nm Mn_2Au (001)/4 nm Py/2 nm Si_3N_4 . The top panel shows the sample morphology together with vertical and horizontal magnetic components of Py. The vector sum of these two components (shown in the bottom panel) reveals a mutually collinear interfacial exchange coupling between the FM and AFM layers. On an average, the domains show a 60:40 distribution between the tilted and non-tilted sides. The image was generated with an accumulation time of ≈ 7 hours.

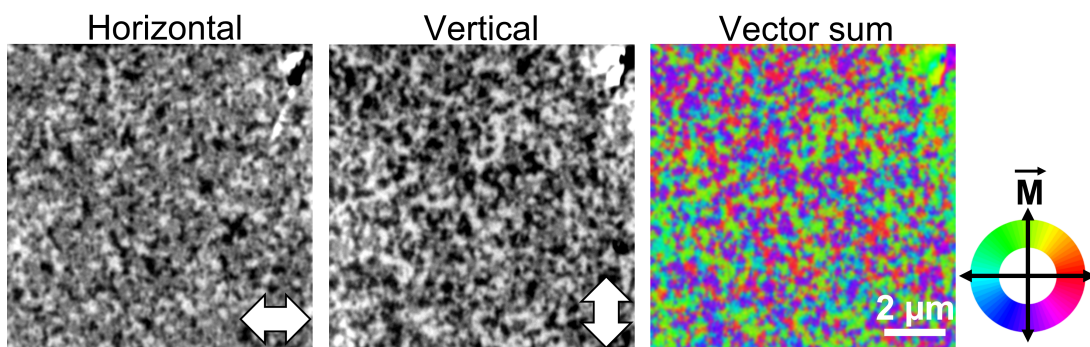


Figure 4.13. SEMPEA imaging of the Py overlayer in a Al_2O_3 ($1\bar{1}02$)/13 nm Ta (001)/22 nm Mn_2Au (001)/4 nm Py/2 nm Si_3N_4 sample. Py is collinearly coupled to Mn_2Au .

4.2.2 XMLD-PEEM

The microscopy began with an identification of the $L_{2,3}$ -absorption edges of Ni, Fe and Mn with XAS. No signs of oxidation were found in the form of chemically shifted absorption peaks within the vicinity of the 2p core levels in both layers. Subsequently, imaging of Py domains was attempted using photon energies corresponding to the $L_{2,3}$ -edges of Ni as a strong signal was expected owing to its high concentration of 81%. The contrast image (at a particular photon energy) is given by the asymmetry (difference normalized to sum) of images acquired with horizontal- and vertical X-ray polarization. However, no magnetic contrast could be observed, which is in agreement with the theoretical prediction of a tiny XMLD at the L-edges of elemental Ni [62]. Eventually, ferromagnetic domain images with a high contrast were obtained at the L_3 -edge of Fe despite its lower concentration of 19% as this element shows a significantly larger XMLD effect [62, 63]. A comparison of the XMLD-PEEM images of both magnetic layers acquired from the same region (figure 4.14) reveals perfect one-to-one correspondence between the FM and AFM domains. The average domain size observed is $\sim 1 \mu m$ and is consistent with the results obtained via SEMPA. All subsequent visualization of AFM domains can therefore, be carried out in-house.

It is evident from figures 4.6 and 4.12 that the average size of an AFM domain exceeds the average area of a Mn_2Au terrace. As the entire Mn_2Au film terminates in a Au plane, the interfacial Py moments couple strongest to the Mn sublattice located directly below this final Au layer (line profile '1' in figure 4.7.b). Owing to the crystallographic symmetry of Mn_2Au , this last magnetic sublattice is always of the same orientation within any chosen AFM domain as illustrated in figure 4.15. Therefore, the FM domains do not terminate at Mn_2Au steps but are able to spread across multiple terraces to perfectly copy the AFM domain structure underneath. It should be noted that if steps which expose both Mn sublattices at the interface were present (for instance, those with a height of $\frac{1}{3} \times c$ -axis parameter of Mn_2Au) they would have caused multiple 180° FM domains to appear within one AFM domain (as a FM domain wall would be formed at each such step).

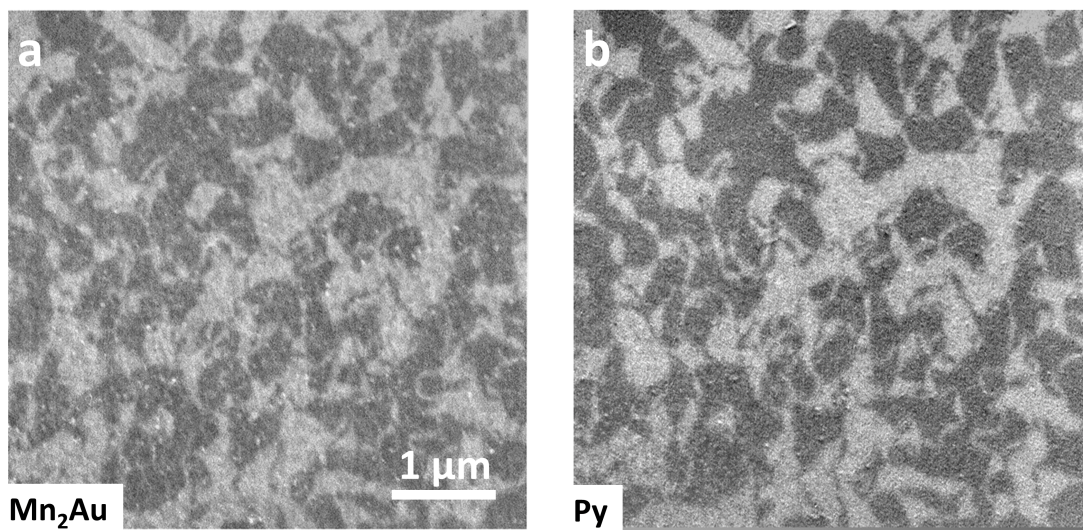


Figure 4.14. XMLD PEEM imaging of an as-grown Al_2O_3 ($1\bar{1}02$)/13 nm Ta (001)/40 nm Mn_2Au (001)/4 nm Py/2 nm Si_3N_4 sample. a. The AFM domains of Mn_2Au visualized using XMLD at the Mn L_3 -edge. The narrow stripe-like features (≈ 150 nm wide) separating any two neighbouring white/black domains are 180° domain walls and can also be observed in the SEMPA images (figure 4.12) upon closer inspection. It should be noted that it is possible to image the AFM through 6 nm of overlaying material. b. Ferromagnetic domains of Py obtained using photon energy corresponding to the Fe L_3 -absorption edge. Py is found to perfectly mimic the AFM domain pattern of the Mn_2Au underlayer. All XMLD-PEEM images presented in this thesis were obtained with the help of B. Sarpi and Y. R. Niu from the MAXPEEM beamline, MAX IV Laboratory, Lund, Sweden.

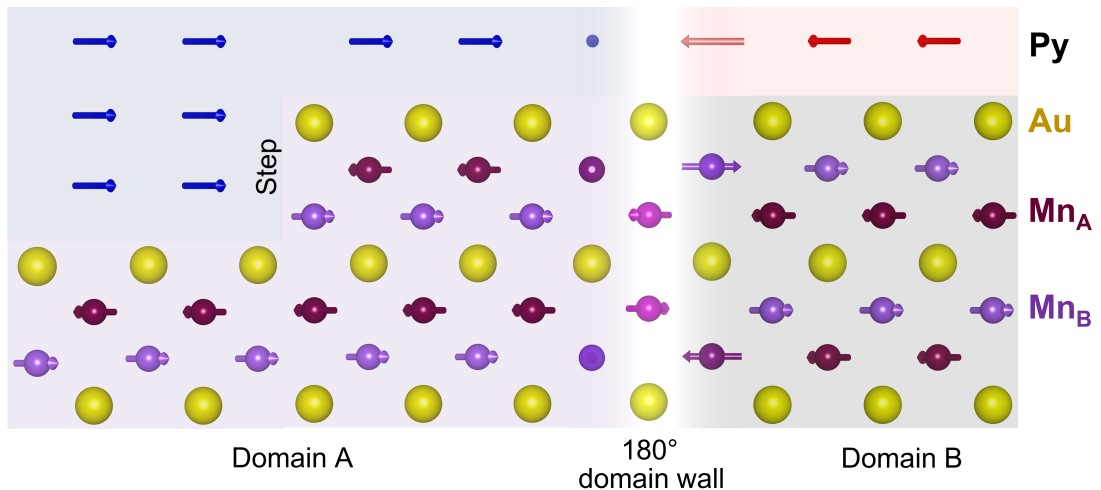


Figure 4.15. Interfacial exchange coupling in Mn_2Au /Py. The bilayer system is viewed along Mn_2Au [100]. The layered crystal structure of Mn_2Au always features the same AFM sublattice below every Au atomic plane within a particular AFM domain (for example, Mn_A in AFM domain A). As the steps observed in the topography of Mn_2Au are integer multiples of half a unit cell, the presence of multiple steps within any given AFM domain does not change the Mn sublattice which participates in interfacial exchange coupling together with Py. Thus, the domain patterns of both magnetic layers match one-to-one. The AFM domains form randomly with no correlation between the domain pattern and film morphology. The strong in-plane anisotropy of Mn_2Au causes the moments in an AFM domain wall to also rotate within the plane, which is faithfully reproduced by the overlying Py moments.

4.3 Quantification of the exchange coupling strength in Mn₂Au/Py

Ferromagnetic hysteresis loops of a 4 nm Py layer (in a Mn₂Au (001)/Py bilayer sample) measured with the external field swept along the AFM easy axes are shown in figure 4.16. Coercive fields of 1400 Oe and 1000 Oe are observed with the field applied along [110] and [1 $\bar{1}$ 0] respectively. Since Py is a soft ferromagnet with negligible coercivity, these large values can only be explained by a strong exchange coupling to the underlying AFM. A conventional square-shaped magnetization reversal loop is obtained along one easy axis of Mn₂Au while a double stepped loop is found along the other. This difference in switching behaviour between the two orthogonal easy directions can be traced back to the tilted c-axis of Mn₂Au and is explored further in section 4.5.

Wadley et al. [63] observed that under the influence of an external magnetic field, 2 nm Fe (001) grown over a very thin AFM layer (5 nm) of CuMnAs (001) could switch its staggered moments below spin-flop field. This interfacial exchange based control of the AFM spin axis was mainly made possible by the weak anisotropy of the CuMnAs film (which is evident from the small coercive field of Fe (001)). The unusually large coercive field in Mn₂Au/Py also hints at a joint rotation of both magnetic orders. If a similar phenomenon is at play, the work done by an applied field to switch the FM moments should equal the energy required to overcome the large in-plane anisotropy of Mn₂Au^{¶¶} (since Py has no anisotropy of its own). This was verified by measuring the hysteresis loops of a series of Mn₂Au/Py samples with the FM thickness ranging from 2 - 10 nm while keeping the AFM thickness fixed at 40 nm. The results are summarized in figure 4.17. The Py coercive field H_c is observed to be inversely proportional to the saturation magnetic moment M_{sat} , implying that their product $M_{sat}H_c$ (i.e., the work done to rotate the magnetic order) is the same in each case. This is consistent with the above premise as the anisotropy of Mn₂Au is expected to remain constant throughout this sample series. To gather more direct evidence in support of this phenomenon, the bilayers were examined further using spectroscopic XMCD and XMLD measurements which are explained in the next section.

Though the FM \leftrightarrow AFM interaction is purely interfacial, it is found to be

^{¶¶} Assuming a simple macrospin rotation of the Néel order.

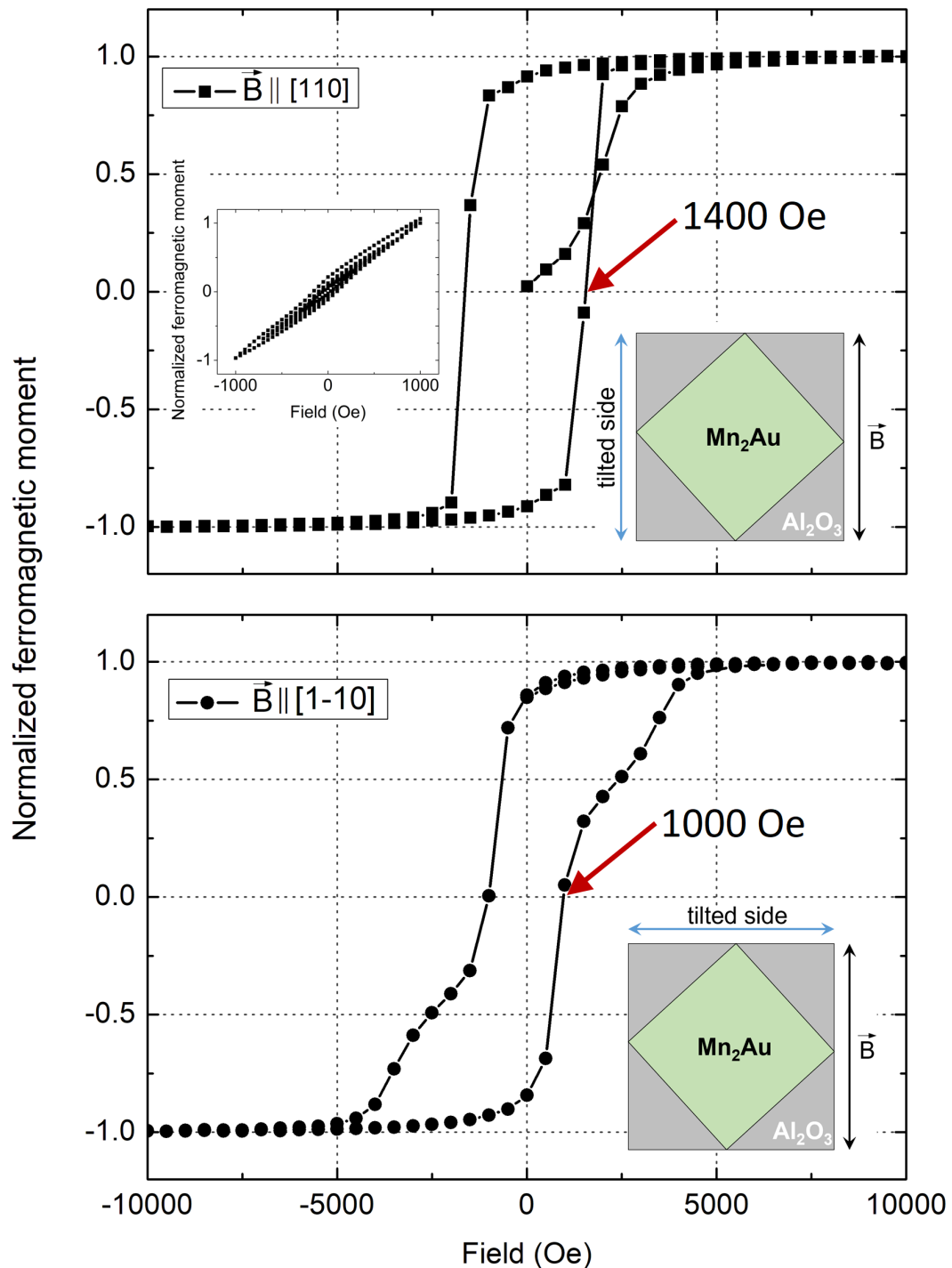


Figure 4.16. Ferromagnetic hysteresis loops of Py in a Al_2O_3 ($\bar{1}\bar{1}02$)/13 nm Ta (001)/40 nm Mn_2Au (001)/4 nm Py/2 nm Si_3N_4 sample. The external field \vec{B} is swept along Mn_2Au [110] in the upper panel. A square shaped hysteresis loop with sharp magnetization switching is observed. The inset shows the behaviour at small fields. The magnetic moment varies linearly with applied field and is restored to zero when the field is removed. Next, the sample is rotated by 90° such that the field is swept along Mn_2Au [$\bar{1}\bar{1}0$] (lower panel). The hysteresis loop shows a dual-stepped magnetization reversal on either branch with a smaller coercive field compared to the previous case.

sufficiently strong to keep the Py coupled to Mn₂Au even at a large thickness of 10 nm. The as-grown domain pattern of this sample is shown in figure 4.18 and is found to be similar to that of the Mn₂Au/4 nm Py sample discussed earlier (figure 4.12).

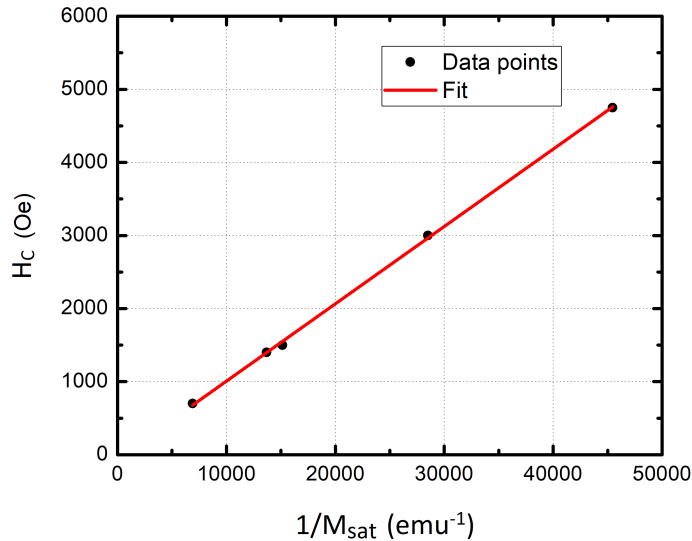


Figure 4.17. Coercive field vs. inverse of Py saturation magnetic moment in Al₂O₃ (1 $\bar{1}$ 02)/13 nm Ta (001)/40 nm Mn₂Au (001)/2 - 10 nm Py/2 nm Si₃N₄ samples. The applied magnetic field was swept parallel to the sample side along which the c-axis of Mn₂Au is tilted (square shaped hysteresis loops are obtained). The fit is a straight line passing through the origin.

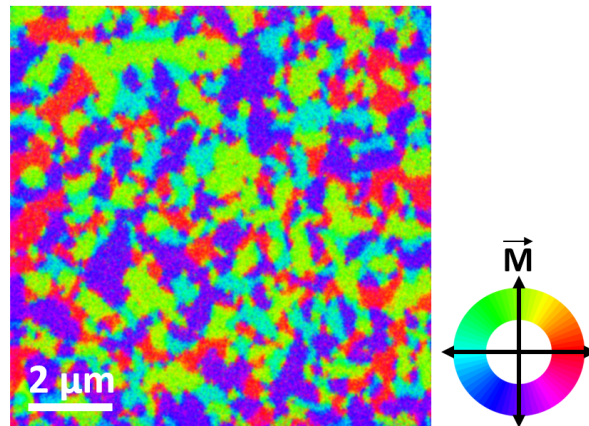


Figure 4.18. SEMPA image of the FM domains in a Al₂O₃ (1 $\bar{1}$ 02)/13 nm Ta (001)/40 nm Mn₂Au (001)/10 nm Py/2 nm Si₃N₄ sample. The colours are more vivid compared to those in figure 4.12 due to the larger thickness of Py. The secondary electrons collected by the detector originate mainly in the Py layer, leading to a larger overall spin-polarization, and therefore a better signal to noise ratio.

4.4 Origin of the large coercive field of exchange coupled Py

Spectroscopic XMCD and XMLD measurements were carried out to understand the influence of external fields on the magnetic order of each individual layer in the Mn₂Au/Py system. The apparatus allows for in-situ application of large magnetic fields required to manipulate the magnetization, a feature which is unavailable in PEEM. The information collected in these measurements lacks spatial resolution as it is averaged over the entire area illuminated by the primary radiation (unlike PEEM). During these measurements the sample was maintained at room temperature and the incident X-ray beam had a spot size of $\approx 360 \times 530 \mu\text{m}$.

First, the as-grown 40 nm Mn₂Au/4 nm Py sample was positioned at an angle of $\theta = 60^\circ$ with respect to the incident radiation (figure 4.19.a) to observe XMCD in Py using the asymmetric absorption of right- and left circularly polarized X-rays at Ni L_{2,3}-edges. The measurement was carried out in total electron yield*** (TEY) mode which is surface sensitive. As the illuminated area is much larger than the average FM/AFM domain, absence of a dichroic signal (figure 4.19.b) confirms the expected multi-domain configuration of the FM (180° domains produce opposing effects, leading to an overall zero XMCD). Next, the sample was subjected to a magnetic field B of 1 T along the x-axis to fully saturate the magnetization of the FM layer (based on SQUID measurements presented in the previous section). Being in a monodomain state, Py now shows strong XMCD at the L_{2,3}-edges of Ni. Subsequently, the underlying Mn₂Au layer was examined for XMLD with normal photon incidence. The asymmetry of absorption spectra acquired with x- and y-polarized light reveals large dichroism at the L_{2,3}-edges of Mn (figure 4.19.c), implying a uniaxial alignment of the staggered magnetization (presence of 90° domains would have yielded a net zero XMLD). This procedure was repeated with the 1 T field applied parallel to the y-axis. The circular dichroism in Py vanishes as its magnetization is now orthogonal to the direction of X-ray incidence while the linear dichroism in Mn₂Au shows sign reversal, implying a rotation of its spin-axis by 90°. Thus, both the magnetic orders never rotate independently of each other.

***The incident X-rays are absorbed by the sample leading to an ejection of photo- and Auger electrons. Consequently, an electron current flows to the sample from ground to make up for this loss and can be measured to quantify the X-ray absorption. As electrons can escape only from the top few nm of the sample, this technique is surface sensitive.

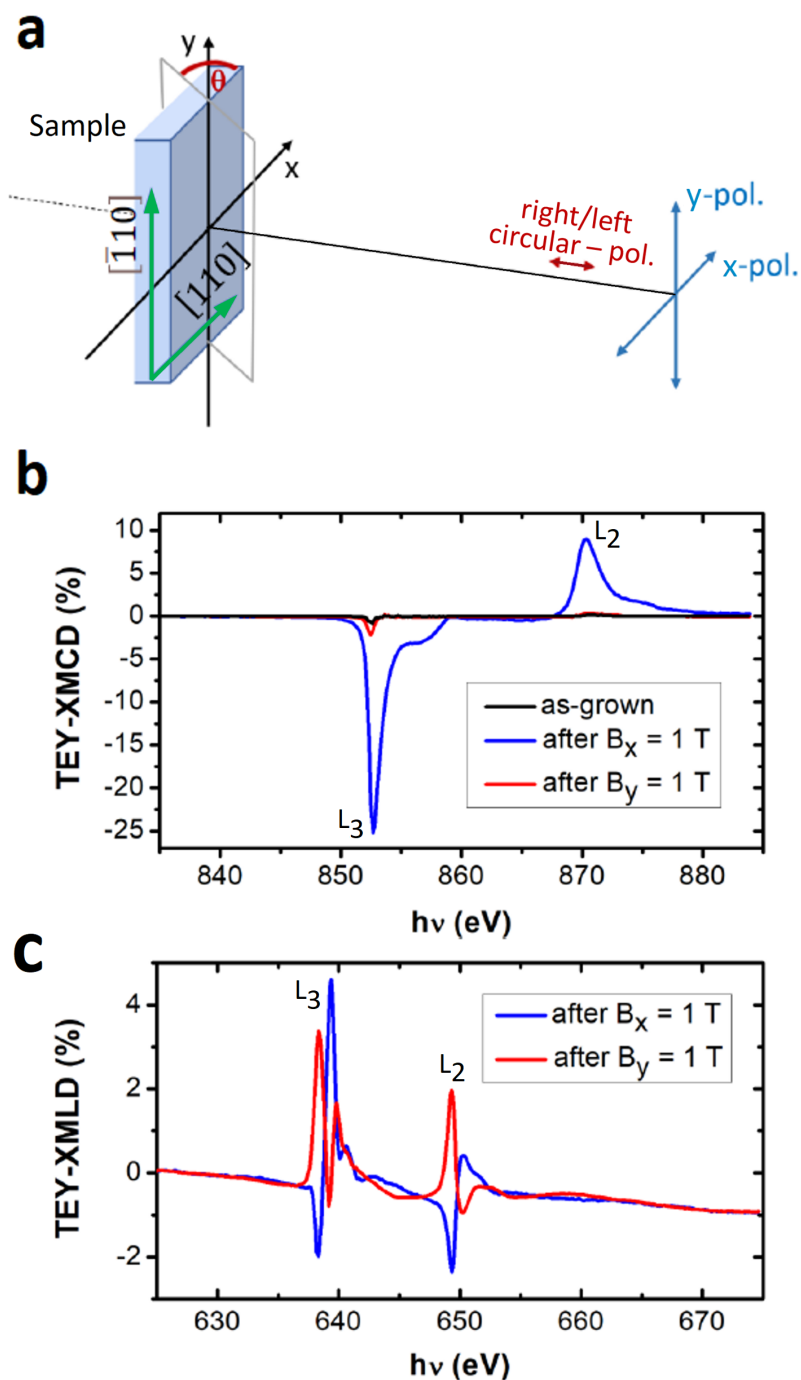


Figure 4.19. a. Experimental geometry of spectroscopic X-ray magnetic dichroism measurements. XMCD and XMLD were measured at $\theta = 60^\circ$ and 0° respectively. A Al_2O_3 ($1\bar{1}02$)/13 nm Ta (001)/40 nm Mn_2Au (001)/4 nm Py/2 nm Si_3N_4 sample was used for these experiments. The bold green arrows represent the easy directions of Mn_2Au (001). b. XMCD at the $L_{2,3}$ -edges of Ni in Py measured using TEY. c. XMLD at the $L_{2,3}$ -edges of Mn in Mn_2Au (001) measured using TEY. The measurements were performed with help from Dr. D. Backes, Dr. L. S. I. Veiga and Dr. S. S. Dhesi at the I06 beamline - Diamond light source in Didcot, United Kingdom.

Based on previous experiments by Sapozhnik et al. [64], the sign of the measured XMLD in Mn_2Au indicates a mutually parallel alignment of the AFM spin axis and applied magnetic field. Thus, the observed field-induced realignment of AFM order is not a product of spin-flop as this phenomenon generates 180° domains perpendicular to the applied field. Moreover, a single layer of Mn_2Au is expected to require much larger field to be manipulated [15]. A similar increase in the coercivity of a FM when combined with an adjoining AFM was previously reported by Scholl et al. [56] in bulk $\text{NiO}/2.5\text{ nm Co}$. Using an approach similar to the one presented above, it was shown that when the ferromagnetic moments switch in response to an external field, momentum is transferred to the neighbouring AFM via interfacial exchange coupling. Consequently, the staggered moments of NiO close to the interface rotate, leading to the creation of a planar domain wall along its thickness. Thus, the observed Co coercivity was a measure of energy expended to overcome antiferromagnetic exchange in NiO for the formation of this domain wall. This possibility was ruled out in the given $\text{Mn}_2\text{Au}/\text{Py}$ samples via bulk sensitive XMLD measurements in fluorescence yield⁺⁺⁺ (FY) mode which found the Néel order to switch through out the antiferromagnetic layer (figure 4.20). Hence, the measured coercive field of Py quantifies the magnetocrystalline anisotropy of the exchange coupled Mn_2Au layer and it can be used to align the AFM moments along a single spin-axis much below the spin-flop transition field. Retention of dichroism upon removal of the external field implies a stably reoriented magnetic order (in both FM and AFM). This was to be expected based on the residual magnetization shown by Py in hysteresis loops obtained via SQUID magnetometry. This so called 'exchange-spring' effect was earlier employed by Park et al. [65] to manipulate the Néel vector in $10\text{ nm Py}/1.5, 3\text{ nm IrMn}$ for an investigation of tunnelling anisotropic magnetoresistance (TAMR) in $\text{IrMn}/\text{MgO}/\text{Pt}$. However, the phenomenon was found to be active only at low temperatures (upto 100 K) unlike the $\text{Mn}_2\text{Au}/\text{Py}$ system, where it is robust at room temperature.

Py continues to stay coupled to Mn_2Au upon subsequent demagnetization of the above sample and a one-to-one correspondence can still be observed between the two domain patterns as shown in figure 4.21.

⁺⁺⁺Core electrons ejected by incident X-rays leave behind vacancies which are filled by electrons from higher energy levels. The secondary photons emitted during this decay process are collected by a fluorescence detector placed close to the sample surface and serve as a measure of primary X-ray absorption. The ability of these photons to escape from deep within the sample gives this mode its bulk sensitivity.

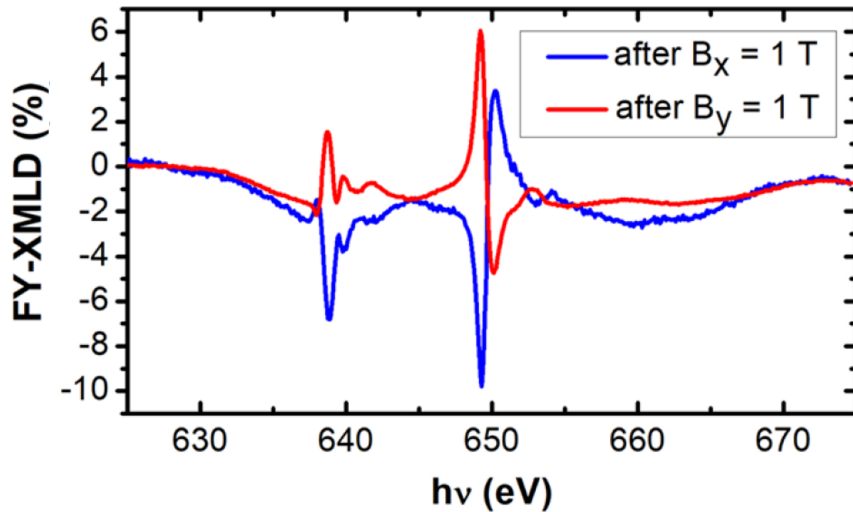


Figure 4.20. XMLD at the $L_{2,3}$ -edges of Mn in Mn_2Au (001) measured via fluorescence yield. The measurement was performed with help from Dr. D. Backes, Dr. L. S. I. Veiga and Dr. S. S. Dhesi at the I06 beamline - Diamond light source in Didcot, United Kingdom.

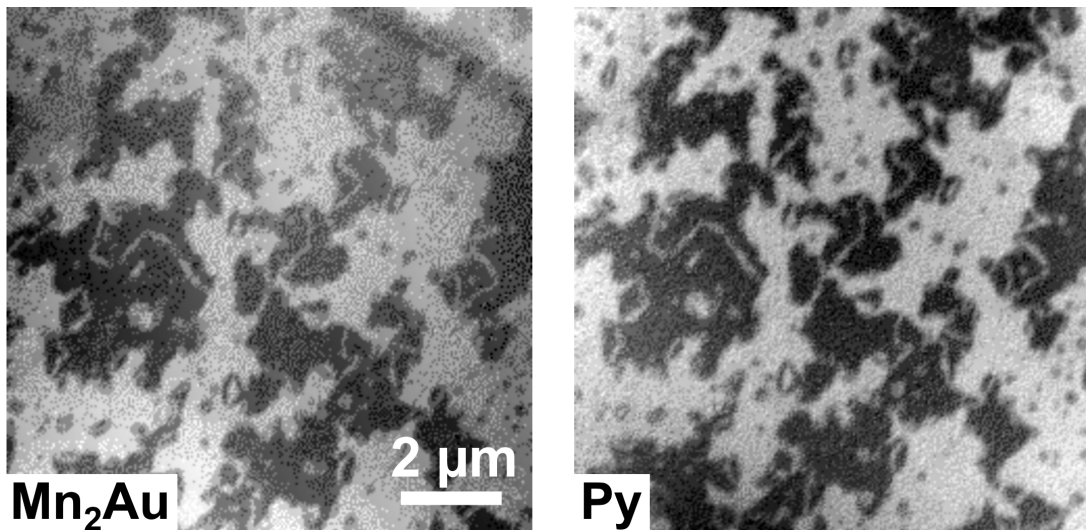


Figure 4.21. XMLD-PEEM images of a Al_2O_3 ($1\bar{1}02$)/13 nm Ta (001)/40 nm Mn_2Au (001)/4 nm Py/2 nm Si_3N_4 sample. The sample was first exposed to a field of 1T along Mn_2Au [110] to achieve a monodomain state and was subsequently demagnetized. Py and Mn_2Au continue to share a common domain pattern. However, the domains are now larger compared to those typically observed in the as-grown state.

Based on a theory by Dr. O. Gomonay from the Institut für Physik, Johannes Gutenberg-Universität Mainz, the field-induced co-rotation of Mn_2Au /Py can be described using a macrospin approximation. The density

of magnetic energy per unit area w of the Mn₂Au/Py bilayer is given by:

$$w(M_{\text{FM}}, \mathbf{N}) = -\frac{H_{\text{an}} t_{\text{AFM}}}{M_{\text{AFM}}^3} (N_x^4 + N_y^4) - J_{\text{coup}} \zeta \mathbf{M}_{\text{FM}} \cdot \mathbf{N} - t_{\text{FM}} \mathbf{M}_{\text{FM}} \cdot \mathbf{H} \quad (4.1)$$

Where the first term on the right hand side describes the magnetocrystalline anisotropy energy of Mn₂Au. $H_{\text{an}} > 0$ and t_{AFM} stand for the in-plane anisotropy field and AFM thickness respectively. \mathbf{N} is the Néel vector and $M_{\text{AFM}} = |\mathbf{N}|$. The magnetic easy axes of Mn₂Au define the coordinate axes x and y . The next term represents the mutual exchange coupling of AFM and FM magnetization vectors. $J_{\text{coup}} > 0$ and ζ stand for the strength and characteristic length of this exchange coupling respectively. \mathbf{M}_{FM} is the FM magnetization. The last term represents the Zeeman energy of Py. \mathbf{H} and t_{FM} are applied magnetic field and thickness of the FM layer respectively.

w has to be minimized with respect to \mathbf{M}_{FM} and \mathbf{N} in order to derive the equilibrium configurations. The as-grown state is comprised of multiple domains with $\mathbf{M}_{\text{FM}} \uparrow \uparrow \mathbf{N}$ and parallel to \hat{x} or \hat{y} . A magnetic field \mathbf{H} applied along \hat{x} lifts the degeneracy between the states with $\mathbf{M}_{\text{FM}} \uparrow \uparrow \mathbf{H}$, $\mathbf{M}_{\text{FM}} \uparrow \downarrow \mathbf{H}$ and $\mathbf{M}_{\text{FM}} \perp \mathbf{H}$. The applied field exerts a ponderomotive force $\propto \mathbf{H} \mathbf{M}_{\text{FM}}$ on the domain walls [66], aiming to lower the overall number of energetically unfavourable states, i.e., domains. As the external field is gradually increased, it results in a non-linear rise in the magnetic moment from zero to M_{sat} (i.e., the virgin magnetization curve seen in the upper panel in figure 4.16). Eventually, the domain walls are completely expelled, leading to the formation of a true AFM monodomain with a single Néel vector. If the external field is not large enough to remove all the domain walls, the process is reversible as indicated by the minor hysteresis loop in the inset of figure 4.16. Cyclic magnetic field sweeps upon saturation cause hysteretic switching between $\mathbf{M}_{\text{FM}} \uparrow \uparrow \mathbf{H}$ and $\mathbf{M}_{\text{FM}} \downarrow \downarrow \mathbf{H}$ configurations. The following expression for coercive field H_c is derived from the stability conditions for these states:

$$H_c = \frac{4H_{\text{an}} J_{\text{coup}} M_{\text{AFM}} \zeta t_{\text{AFM}}}{4H_{\text{an}} t_{\text{AFM}} + J_{\text{coup}} M_{\text{FM}} \zeta t_{\text{FM}}} \frac{1}{M_{\text{FM}}} \quad (4.2)$$

If the exchange coupling is considered to be extremely strong, then $J_{\text{coup}} M_{\text{FM}} \zeta \gg H_{\text{an}} t_{\text{AFM}}$. In such a case, $H_c \approx 4H_{\text{an}} M_{\text{AFM}} t_{\text{AFM}} / (M_{\text{FM}} t_{\text{FM}})$ or $H_c \propto \frac{1}{M_{\text{FM}}}$, which explains the linear behaviour observed earlier in figure 4.17. Using the experimentally determined value of Py magnetization $M_{\text{FM}} = 1.8\mu_B$ per Ni₈₁Fe₁₉ atom together with $M_{\text{AFM}} = 4\mu_B$ per Mn-atom [15], $H_{\text{an}} \approx 40$ Oe is obtained, which corresponds to an in-plane anisotropy constant $K_4 = 2 \times 4\mu_B \times$

$40 \times 10^{-4} \text{ T} = 1.8 \mu\text{eV}$ per formula unit (f.u.) for a 40 nm Mn_2Au thin film. The AFM anisotropy was observed to increase with the Mn_2Au film thickness. For instance, H_c of 2000 Oe was observed in case of 60 nm $\text{Mn}_2\text{Au}/4 \text{ nm Py}$. This variation was also found to be non-linear as the crystallinity of Mn_2Au thin films changes with increasing thickness as explained earlier in section 4.2.1.

4.5 Visualization of field-driven AFM/FM switching behaviour

The Zeeman energy driven switching of Mn_2Au via an exchange coupled ferromagnetic overlayer was imaged using Kerr microscopy. A bilayer sample with Py thickness of 10 nm was chosen for this purpose to obtain a strong magnetic contrast. The images were acquired at various points along the hysteresis loops and are explained in detail below.

First, imaging was carried out with the external field \vec{B} swept parallel to the sample side along which the c-axis of Mn_2Au is tilted (side along which domains are preferentially oriented) as shown in figure 4.22. The corresponding ferromagnetic hysteresis loop (obtained via SQUID) is presented in the central panel. Longitudinal MOKE geometry (section 3.5) was used with the plane of incidence $\parallel \vec{B}$ in order to be sensitive to opposite FM domains oriented along the axis of \vec{B} . A familiar magnetization switching behaviour was observed. The loop begins with the sample fully saturated along +x (point 1). Applying a field larger than 55 mT along -x triggers the nucleation of reversed domains as seen at point 2. Increasing the field further pushes the domain walls, causing these nucleated domains to expand (point 3) and eventually merge to form a reversed monodomain (completion of switching) at point 4. A similar behaviour is seen once again on the other branch of the loop (4 \rightarrow 1). No magnetic contrast was seen when the above field sweep was repeated in transverse MOKE geometry, i.e., with the plane of incidence $\perp \vec{B}$ as the magnetic moments swiftly rotate to align to the external field.

Next, the field was cycled along the non-tilted side, i.e., orthogonal to the axis along which more AFM domains are favoured in the as-grown state. The corresponding Kerr microscopy images (and double-stepped hysteresis loop) are presented in figures 4.23 and 4.24. Only a weak and fleeting magnetic contrast could be observed with the plane of incidence $\parallel \vec{B}$ (figure 4.23). However, strong magnetic contrast was found when the field sweep was

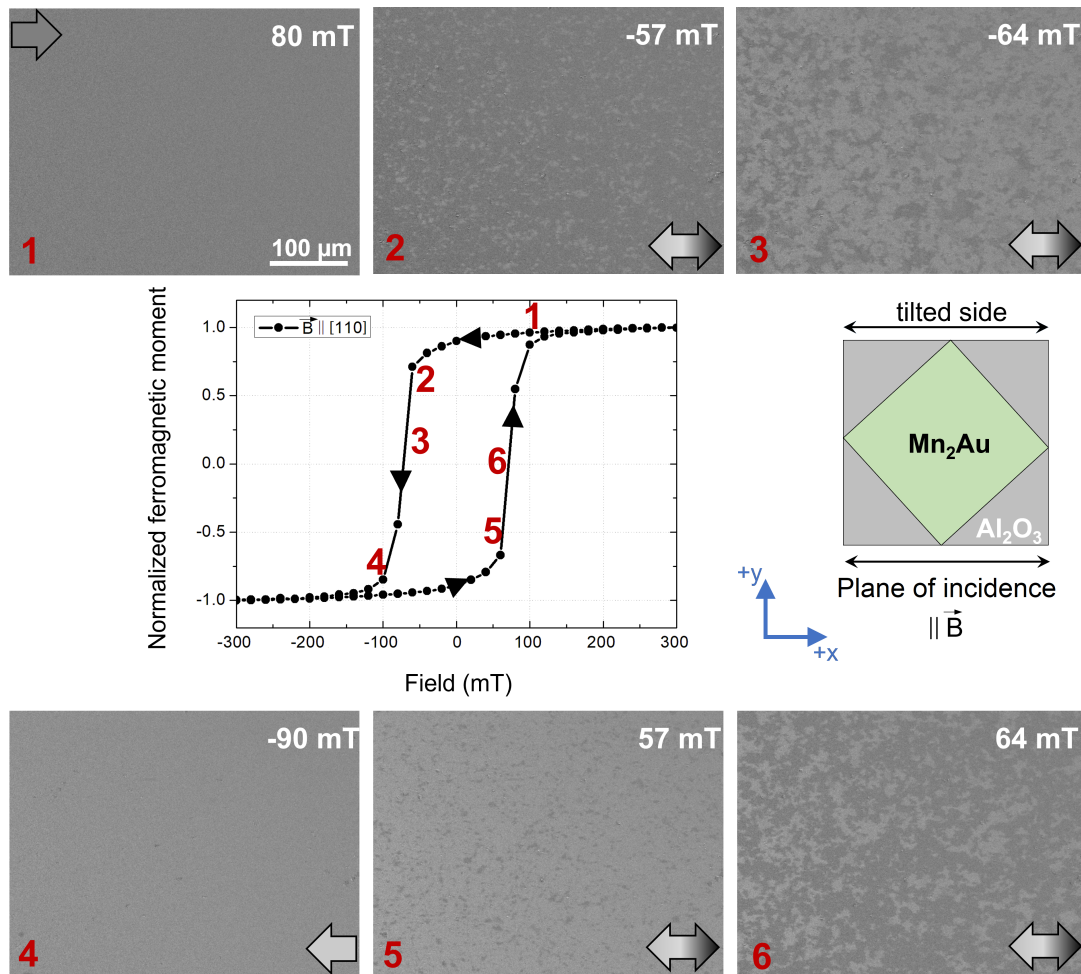


Figure 4.22. Kerr microscopy of Py in a Al_2O_3 ($1\bar{1}02$)/13 nm Ta (001)/40 nm Mn_2Au (001)/10 nm Py sample with the external field swept parallel to the tilted side of Mn_2Au . Py has a coercive field of 70 mT. The domains observed in each frame are oriented along the magnetic field axis.

repeated with the plane of incidence $\perp \vec{B}$, implying that the magnetization (of both layers) rotates to become perpendicular to the applied field (point 2 in figure 4.24.a). Thus, the coercive field is significantly lower in this case as the magnetization readily switches towards this preferred axis. Subsequently, a larger field is required to pull the magnetic moments out of this relatively more stable orientation and align them to the less favoured easy axis. This gives rise to a two-stepped magnetization reversal process. The contrast fades gradually with increasing field, while the domain pattern is retained (point 3), implying that the domains rotate coherently. Eventually, the contrast is completely lost when the magnetization is fully aligned to the external field (point 4). These results are preliminary evidence for strain-induced

manipulation of AFM anisotropy in Mn_2Au . Interestingly, the domain pattern seen at point 2 is almost perfectly reproduced during the latter half of the field cycle (point 5 in figure 4.24.b). This indicates the presence of a pinning mechanism which causes the domain walls to appear at the same locations during both forward and reverse switches.

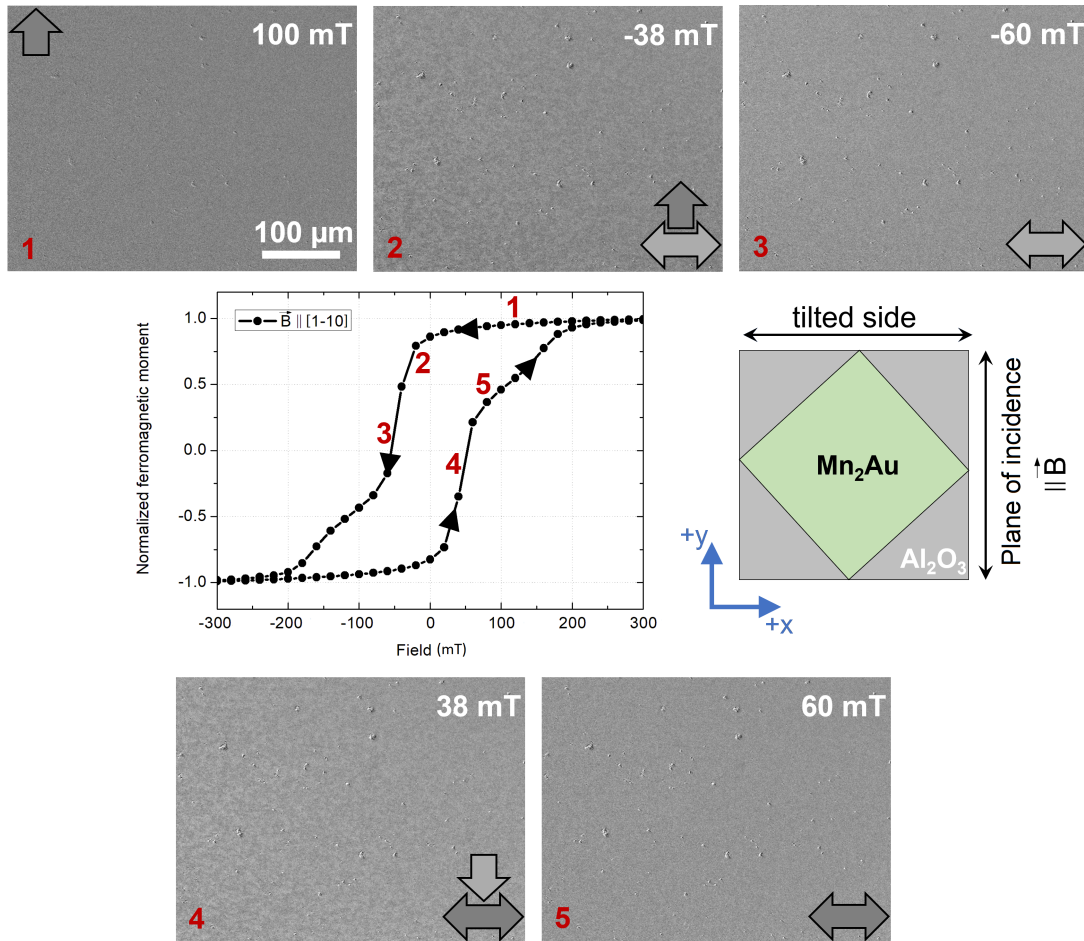


Figure 4.23. Kerr microscopy of Py in a Al_2O_3 ($1\bar{1}02$)/13 nm Ta (001)/40 nm Mn_2Au (001)/10 nm Py sample with the external field swept perpendicular to the tilted side of Mn_2Au . Py has a coercive field of 50 mT. The plane of incidence and external field are mutually parallel. Weak magnetic contrast appears during the field sweep when a part of the magnetization rotates towards the tilted side. As the rest of the magnetization quickly follows, this contrast is only briefly observed.

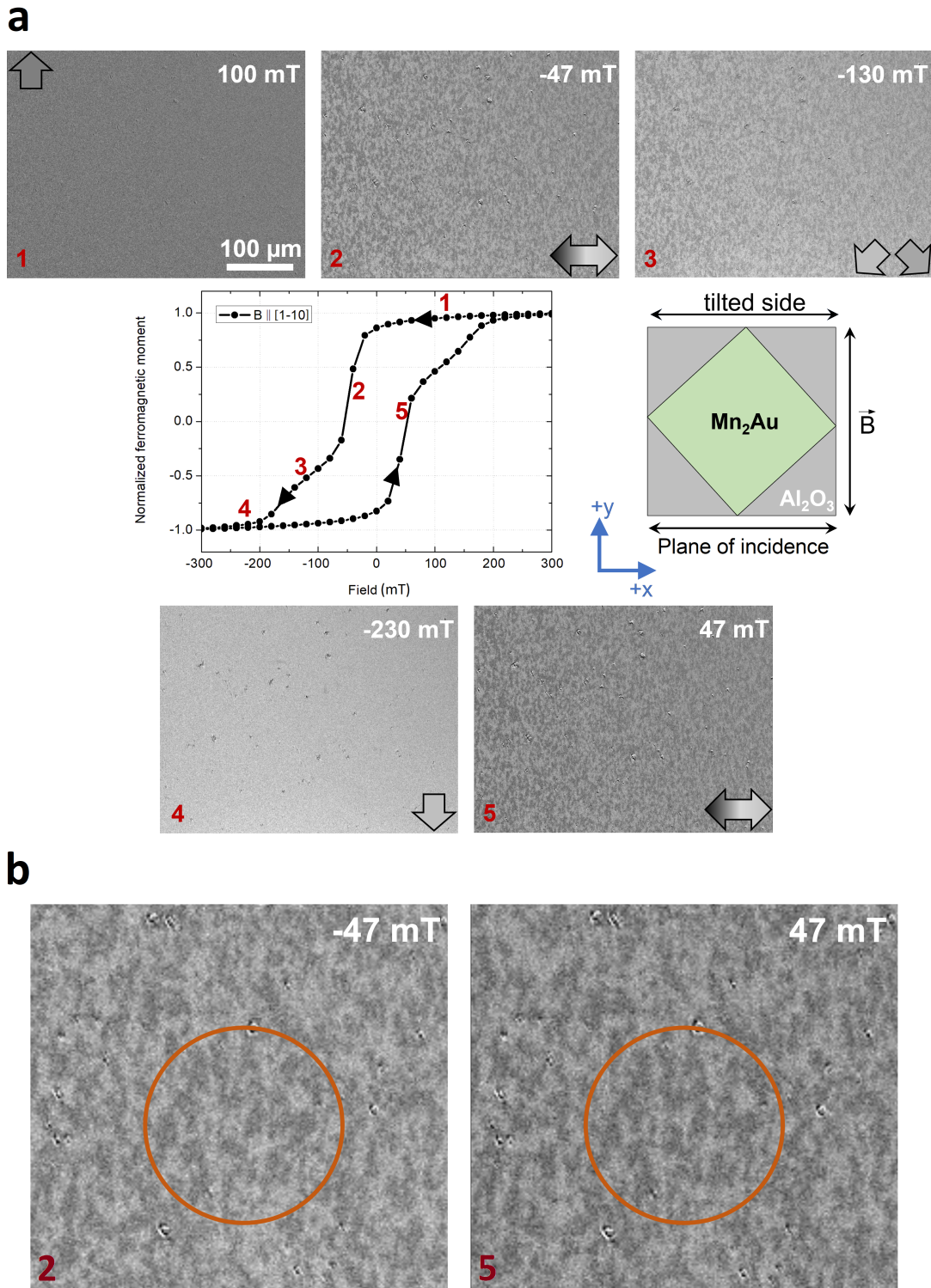


Figure 4.24. a. Kerr microscopy of Py in a Al_2O_3 ($1\bar{1}02$)/13 nm Ta (001)/40 nm Mn_2Au (001)/10 nm Py sample with the external field swept perpendicular to the tilted side of Mn_2Au . The incident light polarization and applied magnetic field are mutually perpendicular. b. The domain patterns corresponding to points 2 and 5 on the hysteresis loop are nearly identical. The same area is encircled in both images for easy comparison.

5 Conclusions & future work

IN summary, the experimental results presented in this thesis are conclusive evidence for a highly robust collinear AFM/FM exchange coupling at the Mn_2Au (001)/Py interface. Using the visualization techniques of SEMPA and XMLD-PEEM, this interaction was shown to cause a perfect imprinting of the AFM domain pattern on the soft ferromagnetic overlayer. This one-to-one correspondance can be ascribed to the layered nature of Mn_2Au combined with the Au termination of Mn_2Au (001) thin films grown for this study. Quantification of the mutual exchange coupling strength was initially attempted using SQUID magnetometry which found a large coercive field of $\approx 0.5\text{T}$ in case of a 2 nm Py overlayer. Further investigation via spectroscopic XMCD and XMLD measurements led to the discovery of a joint rotation of both magnetic orders in the presence of an applied field. Thus, the observed coercivity of Py is understood to be a measure of the magnetocrystalline anisotropy of Mn_2Au . This interfacial exchange mediated re-alignment of the Néel vector allows one to set the AFM in a monodomain state much below its spin-flop field.

Although the Mn_2Au (001) films prepared using MBE and RF magnetron sputtering show a high degree of crystalline order and smooth morphology, the growth certainly has scope for further improvement. The next phase in the study of Mn_2Au /Py bilayers involves in-house microscopy of current-driven switching of AFM domains via the FM layer. Both SEMPA and SQUID measurements have revealed that the canted c -axis of Mn_2Au alters the anisotropy energies pertaining to its two easy axes, thereby making one of them energetically more favourable than the other. This is also expected to make the switching highly asymmetric with forward and reverse

manipulation of the Néel order requiring significantly different critical current densities. Replacing Al_2O_3 (1 $\bar{1}$ 02) with a substrate that possesses a higher rotational symmetry, for instance, MgO (001) is bound to eliminate this problem. Kwon et al. [67] successfully grew Ta (001) thin films on Cr (001) which was deposited on MgO (001) substrates. Thus, a Cr/Ta buffer can be adopted for the epitaxial growth of Mn_2Au (001) on MgO (001). Another promising approach is the growth of Mn_2Au (001) over a Mo (001)/Ta (001) buffer deposited on MgO (001). A large lattice mismatch of 11% hinders the direct growth of epitaxial Ta (001) ($a\sqrt{2} = 4.67 \text{ \AA}$) on MgO (001) ($a = 4.21 \text{ \AA}$). Therefore, the insertion of an epitaxial Mo (001) ($a\sqrt{2} = 4.44 \text{ \AA}$) interlayer serves to bridge this gap, allowing the growth of Ta [110] \parallel Mo [110] \parallel MgO [100]. An optimized growth recipe for such a stack is currently being developed by Dr. Yaryna Lytvynenko of this group.

The effects of the tiny lattice distortion of Mn_2Au (introduced by its tilted c-axis) on its Néel order point towards the possibility of a strain based control of antiferromagnetic anisotropy. This phenomenon can be explored further via XMLD-PEEM using Mn_2Au (001) films grown on thin substrates which can be mechanically strained as desired. Efforts in this direction are presently being undertaken by Dr. Sonka Reimers of this research group. Alternatively, as a strongly coupled Py overlayer has been shown to exactly replicate the underlying AFM domain pattern, strain-induced effects could be observed in-house using SEMPA. Replacing Py with another common ferromagnet like CoFeB which is amorphous (no magnetocrystalline anisotropy) and soft can improve imaging via this technique. Its larger spin polarization (compared to Py) can significantly reduce the accumulation time required to obtain high quality images, allowing one to benefit from the relative ease of operation provided by this method. During the course of this study, the AFM domain size was found to strongly depend on layer thickness. This also explains the large domains previously seen by Sapozhnik et al. [40] in 240 nm thick Mn_2Au (001) films. Thus, using thicker films with large domains could make it easier to observe both current- and strain-induced switching (including domain wall motion).

Ultimately, the success of spin-electronic devices that use antiferromagnetic storage layers is strongly dependant on the discovery of an efficient means for their electrical readout. In this context, the only large signal reported until now has been a spin-valve-like AFM-TAMR of 160% by Park et al. [65] in $\text{IrMn}/\text{MgO}/\text{Pt}$ junctions. However, a low temperature of 4K and external magnetic fields were required to observe this effect,

making it highly impractical for microelectronics applications. This doctoral work has laid the basis for a spin-valve with a AFM/FM/tunnel barrier/FM design that can potentially offer a similarly large signal at room temperature itself. The bottom electrode (AFM/FM), which serves as the storage layer, can be written by current-induced Néel SOTs while the device is read via tunnelling magnetoresistance. Thus, the results presented in this thesis provide motivation for an AFM spintronics device concept that is close to practical application.

Appendix

¹Rashba spin texture

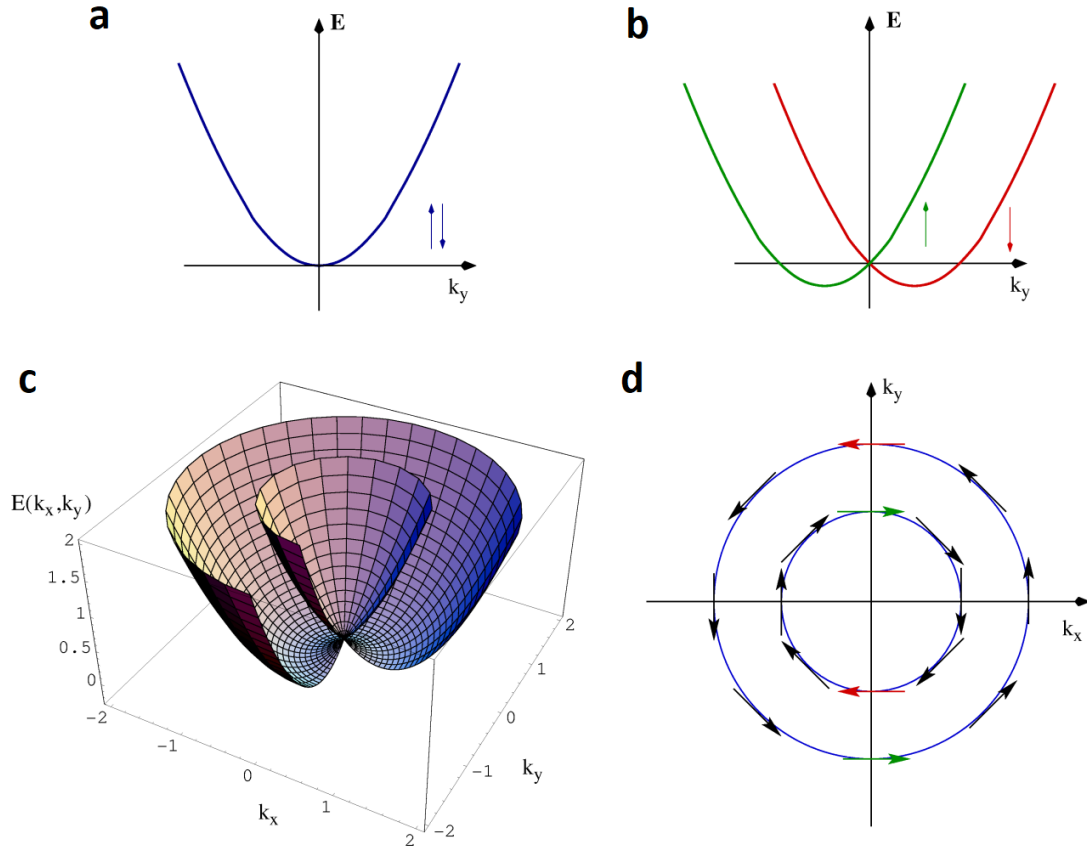


Figure 1. a. Band structure of 1-dimensional free electron model - Energy (E) vs. wave vector (\vec{k}_y). The total energy of an electron (or Hamiltonian) varies as a parabolic function of \vec{k}_y and is expressed as $E = \frac{\hbar^2 |\vec{k}_y|^2}{2m_e}$ where \hbar is the reduced Planck's constant and m_e is electron mass. Every quantum state in \vec{k}_y space is occupied by a pair of \uparrow and \downarrow spins. As the Hamiltonian is spin independent, both spin types share the same parabolic dispersion relation. b. Rashba spin splitting. In the presence of an electric field \vec{E} (which is $\perp \vec{k}_y$) the electrons experience a relativistic magnetic field \vec{B}_R in their rest frame given by $\vec{B}_R = -(\hbar \vec{k}_y \times \vec{E}) / 2m_e c^2$ where c is the speed of light [68]. \vec{B}_R makes an additional contribution (Zeeman energy) to the Hamiltonian given by $\mu_B \sigma \cdot \vec{B}_R$ where μ_B and σ are Bohr magneton and electron spin (vector) respectively. As \uparrow and \downarrow spins gain Zeeman energies of opposite sign, the total energy of an electron now takes the form $E = A |\vec{k}_y|^2 \pm B |\vec{k}_y|$ where A and B are constants. Thus, the parabolic dispersion shown in (a) splits into two (based on electron spin). c. Rashba spin splitting extended to 2-dimensional electron gas (2DEG). An electric field is generated normal to a surface/interface due to structure inversion asymmetry. The 2D dispersion in this case is obtained by rotating the double parabola shown in (b) about the energy axis. d. Fermi contour of a 2D Rashba spin-split surface. Each spin is collinear with \vec{B}_R (and perpendicular to its momentum). Figure modified from [69].

²Non-equilibrium distribution of charge carriers

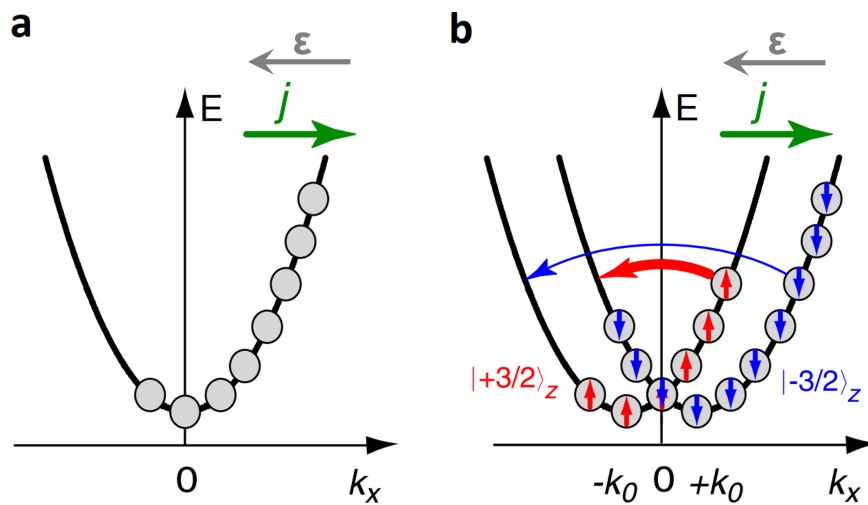


Figure 2. a. Redistribution of electrons in momentum k_x space owing to an applied electric field ϵ . The process is described within the framework of the 1-dimensional free electron model. The electrons are accelerated by ϵ while also being scattered by phonons, impurities etc. The resultant increased occupation of quantum states on the positive side of k_x leads to a current j as shown. b. Non-equilibrium redistribution of electrons in a 1D system with Rashba spin split bands. The applied electric field accelerates electrons in both \uparrow and \downarrow spin parabolas to occupy states with positive k_x similar to (a). Momentum scattering events (which normally preserve spin) can be accompanied by spin flips in the presence of spin-orbit coupling according to the Elliot-Yafet mechanism of spin relaxation. The likelihood of such a spin flip is dependant on the initial and final values of k_x [34]. The probability of \uparrow to \downarrow is significantly larger (represented by the bold red arrow) compared to \downarrow to \uparrow (blue arrow). Therefore, this leads to a net \downarrow spin-polarization for the given direction of ϵ . An opposite spin accumulation can be generated by reversing the direction of applied field. Figure modified from [34].

Bibliography

- [1] C. Chappert, A. Fert and F. N. Van Dau. “The emergence of spin electronics in data storage”. *Nature Materials* **6** (2007), pp. 813–823. DOI: [10.1038/nmat2024](https://doi.org/10.1038/nmat2024) (cit. on pp. 21, 22).
- [2] R. Sbiaa, H. Meng and S. N. Piramanayagam. “Materials with perpendicular magnetic anisotropy for magnetic random access memory”. *physica status solidi (RRL) – Rapid Research Letters* **5** (2011), pp. 413–419. DOI: <https://doi.org/10.1002/pssr.201105420> (cit. on p. 21).
- [3] J. Sinova, S. O. Valenzuela, J. Wunderlich, C. H. Back and T. Jungwirth. “Spin Hall effects”. *Reviews of Modern Physics* **87** (2015), pp. 1213–1260. DOI: [10.1103/RevModPhys.87.1213](https://doi.org/10.1103/RevModPhys.87.1213) (cit. on pp. 21, 30).
- [4] J. Železný, H. Gao, K. Výborný, J. Zemen, J. Mašek, A. Manchon, J. Wunderlich, J. Sinova and T. Jungwirth. “Relativistic Néel-order fields induced by electrical current in antiferromagnets”. *Physical Review Letters* **113** (2014), p. 157201. DOI: [10.1103/PhysRevLett.113.157201](https://doi.org/10.1103/PhysRevLett.113.157201) (cit. on pp. 21–23).
- [5] P. Wadley, B. Howells, J. Železný, C. Andrews, V. Hills, R. P. Campion, V. Novák, K. Olejník, F. Maccherozzi, S. S. Dhesi, S. Y. Martin, T. Wagner, J. Wunderlich, F. Freimuth, Y. Mokrousov, J. Kuneš, J. S. Chauhan, M. J. Grzybowski, A. W. Rushforth, K. W. Edmonds, B. L. Gallagher and T. Jungwirth. “Electrical switching of an antiferromagnet”. *Science* **351** (2016), pp. 587–590. DOI: [10.1126/science.aab1031](https://doi.org/10.1126/science.aab1031) (cit. on pp. 21, 23, 24, 31).
- [6] S. Y. Bodnar, L. Šmejkal, I. Turek, T. Jungwirth, O. Gomonay, J. Sinova, A. A. Sapozhnik, H.-J. Elmers, M. Kläui and M. Jourdan. “Writing and reading antiferromagnetic Mn₂Au by Néel spin-orbit torques and large anisotropic magnetoresistance”. *Nature Communications* **9** (2018), p. 348. DOI: [10.1038/s41467-017-02780-x](https://doi.org/10.1038/s41467-017-02780-x) (cit. on pp. 21, 23, 24).

- [7] M. Meinert, D. Graulich and T. Matalla-Wagner. “Electrical switching of antiferromagnetic Mn_2Au and the role of thermal activation”. *Physical Review Applied* **9** (2018), p. 064040. DOI: [10.1103/PhysRevApplied.9.064040](https://doi.org/10.1103/PhysRevApplied.9.064040) (cit. on pp. 21, 23, 24, 33).
- [8] K. Olejník, V. Schuler, X. Marti, V. Novák, Z. Kašpar, P. Wadley, R. P. Campion, K. W. Edmonds, B. L. Gallagher, J. Garces, M. Baumgartner, P. Gambardella and T. Jungwirth. “Antiferromagnetic $CuMnAs$ multi-level memory cell with microelectronic compatibility”. *Nature Communications* **8** (2017), p. 15434. DOI: [10.1038/ncomms15434](https://doi.org/10.1038/ncomms15434) (cit. on pp. 22, 23).
- [9] X. Marti, I. Fina, C. Frontera, J. Liu, P. Wadley, Q. He, R. J. Paull, J. D. Clarkson, J. Kudrnovský, I. Turek, J. Kuneš, D. Yi, J.-H. Chu, C. T. Nelson, L. You, E. Arenholz, S. Salahuddin, J. Fontcuberta, T. Jungwirth and R. Ramesh. “Room-temperature antiferromagnetic memory resistor”. *Nature Materials* **13** (2014), pp. 367–374. DOI: [10.1038/nmat3861](https://doi.org/10.1038/nmat3861) (cit. on p. 22).
- [10] H. V. Gomonay and V. M. Loktev. “Spin transfer and current-induced switching in antiferromagnets”. *Physical Review B* **81** (2010), p. 144427. DOI: [10.1103/PhysRevB.81.144427](https://doi.org/10.1103/PhysRevB.81.144427) (cit. on p. 22).
- [11] L. Liu, C.-F. Pai, Y. Li, H. W. Tseng, D. C. Ralph and R. A. Buhrman. “Spin-torque switching with the giant spin Hall effect of Tantalum”. *Science* **336** (2012), pp. 555–558. DOI: [10.1126/science.1218197](https://doi.org/10.1126/science.1218197) (cit. on p. 22).
- [12] L. Liu, O. J. Lee, T. J. Gudmundsen, D. C. Ralph and R. A. Buhrman. “Current-induced switching of perpendicularly magnetized magnetic layers using spin torque from the spin Hall effect”. *Physical Review Letters* **109** (2012), p. 096602. DOI: [10.1103/PhysRevLett.109.096602](https://doi.org/10.1103/PhysRevLett.109.096602) (cit. on p. 22).
- [13] https://www.fzu.cz/~zeleznyj/publication/afm_switching/ (cit. on p. 23).
- [14] D. Apalkov, A. Khvalkovskiy, S. Watts, V. Nikitin, X. Tang, D. Lottis, K. Moon, X. Luo, E. Chen, A. Ong, A. Driskill-Smith and M. Krounbi. “Spin-transfer torque magnetic random access memory (STT-MRAM)”. *Journal on Emerging Technologies in Computing Systems* **9** (2013). DOI: [10.1145/2463585.2463589](https://doi.org/10.1145/2463585.2463589) (cit. on p. 23).

-
- [15] V. M. T. S. Barthem, C. V. Colin, H. Mayaffre, M.-H. Julien and D. Givord. "Revealing the properties of Mn_2Au for antiferromagnetic spintronics". *Nature Communications* **4** (2013), p. 2892. DOI: [10.1038/ncomms3892](https://doi.org/10.1038/ncomms3892) (cit. on pp. 24, 73, 75).
- [16] S. Yuasa, T. Nagahama, A. Fukushima, Y. Suzuki and K. Ando. "Giant room-temperature magnetoresistance in single-crystal Fe/MgO/Fe magnetic tunnel junctions". *Nature Materials* **3** (2004), pp. 868–871. DOI: [10.1038/nmat1257](https://doi.org/10.1038/nmat1257) (cit. on p. 24).
- [17] D. D. Djayaprawira, K. Tsunekawa, M. Nagai, H. Maehara, S. Yamagata, N. Watanabe, S. Yuasa, Y. Suzuki and K. Ando. "230% room-temperature magnetoresistance in CoFeB/MgO/CoFeB magnetic tunnel junctions". *Applied Physics Letters* **86** (2005), p. 092502. DOI: [10.1063/1.1871344](https://doi.org/10.1063/1.1871344) (cit. on p. 24).
- [18] S. Ikeda, J. Hayakawa, Y. Ashizawa, Y. M. Lee, K. Miura, H. Hasegawa, M. Tsunoda, F. Matsukura and H. Ohno. "Tunnel magnetoresistance of 604% at 300K by suppression of Ta diffusion in CoFeB/MgO/CoFeB pseudo-spin-valves annealed at high temperature". *Applied Physics Letters* **93** (2008), p. 082508. DOI: [10.1063/1.2976435](https://doi.org/10.1063/1.2976435) (cit. on p. 24).
- [19] C. C. Chiang, S. Y. Huang, D. Qu, P. H. Wu and C. L. Chien. "Absence of evidence of electrical switching of the antiferromagnetic Néel vector". *Physical Review Letters* **123** (2019), p. 227203. DOI: [10.1103/PhysRevLett.123.227203](https://doi.org/10.1103/PhysRevLett.123.227203) (cit. on p. 24).
- [20] T. Matalla-Wagner, J.-M. Schmalhorst, G. Reiss, N. Tamura and M. Meinert. "Resistive contribution in electrical-switching experiments with antiferromagnets". *Physical Review Research* **2** (2020), p. 033077. DOI: [10.1103/PhysRevResearch.2.033077](https://doi.org/10.1103/PhysRevResearch.2.033077) (cit. on p. 24).
- [21] M. J. Grzybowski, P. Wadley, K. W. Edmonds, R. Beardsley, V. Hills, R. P. Campion, B. L. Gallagher, J. S. Chauhan, V. Novak, T. Jungwirth, F. Maccherozzi and S. S. Dhesi. "Imaging current-induced switching of antiferromagnetic domains in CuMnAs ". *Physical Review Letters* **118** (2017), p. 057701. DOI: [10.1103/PhysRevLett.118.057701](https://doi.org/10.1103/PhysRevLett.118.057701) (cit. on p. 25).
- [22] S. Y. Bodnar, M. Filianina, S. P. Bommanaboyena, T. Forrest, F. Maccherozzi, A. A. Sapozhnik, Y. Skourski, M. Kläui and M. Jourdan. "Imaging of current induced Néel vector switching in antiferromagnetic Mn_2Au ". *Physical Review B* **99** (2019), p. 140409. DOI: [10.1103/PhysRevB.99.140409](https://doi.org/10.1103/PhysRevB.99.140409) (cit. on p. 25).

- [23] <https://www.nobelprize.org/prizes/physics/1970/neel/lecture/> (cit. on p. 27).
- [24] C. Kittel. Introduction to solid state physics (8th ed.). John Wiley & Sons, Inc., (2013). Chap. 13, pp. 361-392, ISBN : 978-81-265-3518-7. (Cit. on pp. 28, 32).
- [25] C. Kittel. "Theory of antiferromagnetic resonance". *Physical Review* **82** (1951), pp. 565–565. DOI: [10.1103/PhysRev.82.565](https://doi.org/10.1103/PhysRev.82.565) (cit. on p. 28).
- [26] I. Mihai Miron, G. Gaudin, S. Auffret, B. Rodmacq, A. Schuhl, S. Pizzini, J. Vogel and P. Gambardella. "Current-driven spin torque induced by the Rashba effect in a ferromagnetic metal layer". *Nature Materials* **9** (2010), pp. 230–234. DOI: [10.1038/nmat2613](https://doi.org/10.1038/nmat2613) (cit. on p. 28).
- [27] V. Edelstein. "Spin polarization of conduction electrons induced by electric current in two-dimensional asymmetric electron systems". *Solid State Communications* **73** (1990), pp. 233–235. DOI: [https://doi.org/10.1016/0038-1098\(90\)90963-C](https://doi.org/10.1016/0038-1098(90)90963-C) (cit. on p. 29).
- [28] V. V. Bel'kov and S. D. Ganichev. "Magneto-gyrotropic effects in semiconductor quantum wells". *Semiconductor Science and Technology* **23** (2008), p. 114003. DOI: [10.1088/0268-1242/23/11/114003](https://doi.org/10.1088/0268-1242/23/11/114003) (cit. on p. 29).
- [29] A. Hoffmann. "Spin Hall effects in metals". *IEEE Transactions on Magnetics* **49** (2013), pp. 5172–5193. DOI: [10.1109/TMAG.2013.2262947](https://doi.org/10.1109/TMAG.2013.2262947) (cit. on p. 29).
- [30] A. Chernyshov, M. Overby, X. Liu, J. K. Furdyna, Y. Lyanda-Geller and L. P. Rokhinson. "Evidence for reversible control of magnetization in a ferromagnetic material by means of spin–orbit magnetic field". *Nature Physics* **5** (2009), pp. 656–659. DOI: [10.1038/nphys1362](https://doi.org/10.1038/nphys1362) (cit. on p. 29).
- [31] C. Ciccarelli, L. Anderson, V. Tshitoyan, A. J. Ferguson, F. Gerhard, C. Gould, L. W. Molenkamp, J. Gayles, J. Železný, L. Šmejkal, Z. Yuan, J. Sinova, F. Freimuth and T. Jungwirth. "Room-temperature spin-orbit torque in NiMnSb". *Nature Physics* **12** (2016), pp. 855–860. DOI: [10.1038/nphys3772](https://doi.org/10.1038/nphys3772) (cit. on p. 29).
- [32] J. Železný, H. Gao, A. Manchon, F. Freimuth, Y. Mokrousov, J. Zemen, J. Mašek, J. Sinova and T. Jungwirth. "Spin-orbit torques in locally and globally noncentrosymmetric crystals: Antiferromagnets and ferromagnets". *Physical Review B* **95** (2017), p. 014403. DOI: [10.1103/PhysRevB.95.014403](https://doi.org/10.1103/PhysRevB.95.014403) (cit. on p. 29).

- [33] V. Baltz, A. Manchon, M. Tsoi, T. Moriyama, T. Ono and Y. Tserkovnyak. “Antiferromagnetic spintronics”. *Reviews of Modern Physics* **90** (2018), p. 015005. DOI: [10.1103/RevModPhys.90.015005](https://doi.org/10.1103/RevModPhys.90.015005) (cit. on p. 29).
- [34] S. D. Ganichev, S. N. Danilov, P. Schneider, V. V. Bel’kov, L. E. Golub, W. Wegscheider, D. Weiss, and W. Prettl. Can an electric current orient spins in quantum wells? arXiv:cond-mat/0403641 (2004). <https://arxiv.org/abs/cond-mat/0403641> (cit. on pp. 30, 87).
- [35] A. Brataas, A. D. Kent and H. Ohno. “Current-induced torques in magnetic materials”. *Nature Materials* **11** (2012), pp. 372–381. DOI: [10.1038/nmat3311](https://doi.org/10.1038/nmat3311) (cit. on p. 32).
- [36] H.-C. Wu, Z.-M. Liao, R. G. S. Sofin, G. Feng, X.-M. Ma, A. B. Shick, O. N. Mryasov and I. V. Shvets. “Mn₂Au: Body-centered-tetragonal bimetallic antiferromagnets grown by molecular beam epitaxy”. *Advanced Materials* **24** (2012), pp. 6374–6379. DOI: <https://doi.org/10.1002/adma.201202273> (cit. on p. 33).
- [37] M. Jourdan, H. Bräuning, A. Sapozhnik, H.-J. Elmers, H. Zabel and M. Kläui. “Epitaxial Mn₂Au thin films for antiferromagnetic spintronics”. *Journal of Physics D: Applied Physics* **48** (2015), p. 385001. DOI: [10.1088/0022-3727/48/38/385001](https://doi.org/10.1088/0022-3727/48/38/385001) (cit. on pp. 33, 51, 56, 60).
- [38] M. Arana, F. Estrada, D. S. Maior, J. B. S. Mendes, L. E. Fernandez-Outon, W. A. A. Macedo, V. M. T. S. Barthem, D. Givord, A. Azevedo and S. M. Rezende. “Observation of magnons in Mn₂Au films by inelastic Brillouin and Raman light scattering”. *Applied Physics Letters* **111** (2017), p. 192409. DOI: [10.1063/1.5001705](https://doi.org/10.1063/1.5001705) (cit. on p. 33).
- [39] X. F. Zhou, J. Zhang, F. Li, X. Z. Chen, G. Y. Shi, Y. Z. Tan, Y. D. Gu, M. S. Saleem, H. Q. Wu, F. Pan and C. Song. “Strong orientation-dependent spin-orbit torque in thin films of the antiferromagnet Mn₂Au”. *Physical Review Applied* **9** (2018), p. 054028. DOI: [10.1103/PhysRevApplied.9.054028](https://doi.org/10.1103/PhysRevApplied.9.054028) (cit. on p. 33).
- [40] A. A. Sapozhnik, M. Filianina, S. Y. Bodnar, A. Lamirand, M.-A. Mawass, Y. Skourski, H.-J. Elmers, H. Zabel, M. Kläui and M. Jourdan. “Direct imaging of antiferromagnetic domains in Mn₂Au manipulated by high magnetic fields”. *Physical Review B* **97** (2018), p. 134429. DOI: [10.1103/PhysRevB.97.134429](https://doi.org/10.1103/PhysRevB.97.134429) (cit. on pp. 35, 82).
- [41] S. Hasegawa. “Reflection high-energy electron diffraction”. Characterization of materials. John Wiley & Sons, Ltd (2012), pp. 1–14. DOI: <https://doi.org/10.1002/0471266965.com139> (cit. on pp. 36, 38).

- [42] C. Kittel. Introduction to solid state physics (8th ed.). John Wiley & Sons, Inc., (2013). Chap. 2, pp. 23-45, ISBN : 978-81-265-3518-7. (Cit. on p. 36).
- [43] A. N. Hattori and K. Hattori. "21st century surface science". IntechOpen, (2020). Chap. 6. DOI: [10.5772/intechopen.92860](https://doi.org/10.5772/intechopen.92860) (cit. on p. 37).
- [44] J. Clarke. "SQUIDS". *Scientific American* **271** (1994), pp. 46–53 (cit. on pp. 40–42).
- [45] STAR Cryoelectronics, Mr. SQUID® user's guide. <https://starcryo.com/wp-content/themes/education-pro/manuals/MrSQm66.pdf> (cit. on p. 40).
- [46] J. F. Annett. Superconductivity, superfluids and condensates. Oxford University Press Inc., New York (2004). Chap. 5, pp. 97–125 (cit. on p. 40).
- [47] J. Kirschner and R. Feder. "Spin polarization in double diffraction of low-energy electrons from W(001): Experiment and theory". *Physical Review Letters* **42** (1979), pp. 1008–1011. DOI: [10.1103/PhysRevLett.42.1008](https://doi.org/10.1103/PhysRevLett.42.1008) (cit. on p. 43).
- [48] G.-C. Wang, R. J. Celotta and D. T. Pierce. "Polarized low-energy-electron diffraction from W(100)". *Physical Review B* **23** (1981), pp. 1761–1770. DOI: [10.1103/PhysRevB.23.1761](https://doi.org/10.1103/PhysRevB.23.1761) (cit. on p. 43).
- [49] <http://evicomagnetics.com/info/kerr-microscopy-principle/> (cit. on p. 45).
- [50] G. van der Laan and A. I. Figueroa. "X-ray magnetic circular dichroism—A versatile tool to study magnetism". *Coordination Chemistry Reviews* **277-278** (2014). Following Chemical Structures using Synchrotron Radiation, pp. 95–129. DOI: <https://doi.org/10.1016/j.ccr.2014.03.018> (cit. on p. 47).
- [51] J. Stöhr. "Exploring the microscopic origin of magnetic anisotropies with X-ray magnetic circular dichroism (XMCD) spectroscopy". *Journal of Magnetism and Magnetic Materials* **200** (1999), pp. 470–497. DOI: [https://doi.org/10.1016/S0304-8853\(99\)00407-2](https://doi.org/10.1016/S0304-8853(99)00407-2) (cit. on p. 46).
- [52] U. Fano. "Spin orientation of photoelectrons ejected by circularly polarized light". *Physical Review* **178** (1969), pp. 131–136. DOI: [10.1103/PhysRev.178.131](https://doi.org/10.1103/PhysRev.178.131) (cit. on p. 46).
- [53] J. Stöhr and S. Anders. "X-ray spectro-microscopy of complex materials and surfaces". *IBM Journal of Research and Development* **44** (2000), pp. 535–551. DOI: [10.1147/rd.444.0535](https://doi.org/10.1147/rd.444.0535) (cit. on pp. 48, 50).

- [54] J. Stöhr, H. Padmore, S. Anders, T. Stammler and M. R. Scheinfein. "Principles of X-ray magnetic dichroism spectromicroscopy". *Surface Review and Letters* **5** (1998), pp. 1297–1308 (cit. on p. 48).
- [55] F. Nolting, A. Scholl, J. Stöhr, J. W. Seo, J. Fompeyrine, H. Siegart, J.-P. Locquet, S. Anders, J. Lüning, E. E. Fullerton, M. F. Toney, M. R. Scheinfein and H. A. Padmore. "Direct observation of the alignment of ferromagnetic spins by antiferromagnetic spins". *Nature* **405** (2000), pp. 767–769. DOI: [10.1038/35015515](https://doi.org/10.1038/35015515) (cit. on p. 49).
- [56] A. Scholl, M. Liberati, E. Arenholz, H. Ohldag and J. Stöhr. "Creation of an antiferromagnetic exchange spring". *Physical Review Letters* **92** (2004), p. 247201. DOI: [10.1103/PhysRevLett.92.247201](https://doi.org/10.1103/PhysRevLett.92.247201) (cit. on pp. 49, 73).
- [57] A. Wildes, J. Mayer and K. Theis-Bröhl. "The growth and structure of epitaxial niobium on sapphire". *Thin Solid Films* **401** (2001), pp. 7–34. DOI: [https://doi.org/10.1016/S0040-6090\(01\)01631-5](https://doi.org/10.1016/S0040-6090(01)01631-5) (cit. on p. 57).
- [58] K. Tanabe, H. Asano, Y. Katoh and O. Michikami. "Properties of superconducting ZrN thin films deposited by dc reactive magnetron sputtering". *Japanese Journal of Applied Physics* **26** (1987), pp. L570–L572. DOI: [10.1143/jjap.26.1570](https://doi.org/10.1143/jjap.26.1570) (cit. on p. 57).
- [59] D. Schönke. "Static and dynamic magnetic imaging of different magnetic materials using scanning electron microscopy with polarization analysis". PhD thesis. Johannes Gutenberg-Universität Mainz, (2021). DOI: <http://doi.org/10.25358/openscience-5659> (cit. on p. 61).
- [60] H. J. Elmers, S. V. Chernov, S. W. D'Souza, S. P. Bommanaboyena, S. Y. Bodnar, K. Medjanik, S. Babenkov, O. Fedchenko, D. Vasilyev, S. Y. Agustsson, C. Schlueter, A. Gloskovskii, Y. Matveyev, V. N. Strocov, Y. Skourski, L. Šmejkal, J. Sinova, J. Minár, M. Kläui, G. Schönhense and M. Jourdan. "Néel vector induced manipulation of valence states in the collinear antiferromagnet Mn₂Au". *ACS Nano* **14** (2020), pp. 17554–17564. DOI: [10.1021/acsnano.0c08215](https://doi.org/10.1021/acsnano.0c08215) (cit. on p. 61).
- [61] A. A. Sapozhnik, M. Jourdan, H. Zabel, M. Kläui and H.-J. Elmers. "Exchange bias in epitaxial Mn₂Au (001)/Fe (001) bilayers". *Journal of Physics D: Applied Physics* **52** (2019), p. 465003. DOI: [10.1088/1361-6463/ab3966](https://doi.org/10.1088/1361-6463/ab3966) (cit. on p. 62).

- [62] J. Kuneš and P. M. Oppeneer. “Anisotropic X-ray magnetic linear dichroism at the $L_{2,3}$ edges of cubic Fe, Co, and Ni: *Ab initio* calculations and model theory”. *Physical Review B* **67** (2003), p. 024431. DOI: [10.1103/PhysRevB.67.024431](https://doi.org/10.1103/PhysRevB.67.024431) (cit. on p. 65).
- [63] P. Wadley, K. W. Edmonds, M. R. Shahedkhah, R. P. Champion, B. L. Gallagher, J. Železný, J. Kuneš, V. Novák, T. Jungwirth, V. Saidl, P. Němec, F. Maccherozzi and S. S. Dhesi. “Control of antiferromagnetic spin axis orientation in bilayer Fe/CuMnAs films”. *Scientific Reports* **7** (2017), p. 11147. DOI: [10.1038/s41598-017-11653-8](https://doi.org/10.1038/s41598-017-11653-8) (cit. on pp. 65, 68).
- [64] A. A. Sapozhnik, R. Abrudan, Y. Skourski, M. Jourdan, H. Zabel, M. Kläui and H.-J. Elmers. “Manipulation of antiferromagnetic domain distribution in Mn_2Au by ultrahigh magnetic fields and by strain”. *physica status solidi (RRL) – Rapid Research Letters* **11** (2017), p. 1600438. DOI: <https://doi.org/10.1002/pssr.201600438> (cit. on p. 73).
- [65] B. G. Park, J. Wunderlich, X. Martí, V. Holý, Y. Kurosaki, M. Yamada, H. Yamamoto, A. Nishide, J. Hayakawa, H. Takahashi, A. B. Shick and T. Jungwirth. “A spin-valve-like magnetoresistance of an antiferromagnet-based tunnel junction”. *Nature Materials* **10** (2011), pp. 347–351. DOI: [10.1038/nmat2983](https://doi.org/10.1038/nmat2983) (cit. on pp. 73, 82).
- [66] O. Gomonay, T. Jungwirth and J. Sinova. “High antiferromagnetic domain wall velocity induced by Néel spin-orbit torques”. *Physical Review Letters* **117** (2016), p. 017202. DOI: [10.1103/PhysRevLett.117.017202](https://doi.org/10.1103/PhysRevLett.117.017202) (cit. on p. 75).
- [67] A. Kwon, S. Fähler, V. Neu and L. Schultz. “Effect of composition on phase formation, microstructure and magnetic properties of Nd–Fe–B thin films”. *Journal of Magnetism and Magnetic Materials* **302** (2006), pp. 252–258. DOI: <https://doi.org/10.1016/j.jmmm.2005.09.014> (cit. on p. 82).
- [68] P. Gambardella and I. M. Miron. “Current-induced spin–orbit torques”. *Philosophical Transactions of the Royal Society A* **369** (2011), pp. 3175–3197. DOI: <http://doi.org/10.1098/rsta.2010.0336> (cit. on p. 86).
- [69] D. Bercioux and P. Lucignano. “Quantum transport in Rashba spin–orbit materials: a review”. *Reports on Progress in Physics* **78** (2015), p. 106001. DOI: [10.1088/0034-4885/78/10/106001](https://doi.org/10.1088/0034-4885/78/10/106001) (cit. on p. 86).